Modeling the Spread of Airborne Particles Associated with Harmful Algal Blooms and Plumes of Colored Smoke

Landon T. Bilyeu

Dissertation submitted to the faculty of the Virginia Polytechnic Institute and State University in partial fulfillment of the requirements for the degree of

Doctor of Philosophy

In

Plant Pathology, Physiology, and Weed Science

David G. Schmale III, Chair

Shane D. Ross

Hossein Foroutan

W. Cully Hession

Aug 1, 2024

Blacksburg, Virginia, United States of America

Keywords: bioaerosol, plume, uncrewed aerial vehicle, remote sensing, harmful algal blooms, weather

Modeling the Spread of Airborne Particles Associated with Harmful Algal Blooms and Plumes of Colored Smoke

Landon T. Bilyeu

(Academic Abstract)

Lakes and oceans are threatened by harmful algal blooms (HABs), caused mostly by toxic cyanobacteria. When people or animals drink the toxic water, it can be damaging to their health, potentially leading to hospitalization or even death. In some cases, these toxins are not just limited to the water, but can become airborne through wave breaking, bubble bursting, and spume droplet formation. New information is needed regarding the transport and fate of HAB-associated aerosols. The overall goal of this research was to monitor particle concentrations and measure meteorological conditions near HAB sites to determine the conditions that may lead to increased exposure to HAB cells and toxins in the atmosphere. By creating predictions of which conditions and locations will be experiencing higher aerosol levels at any given time, models could be used to inform the public and policy makers to ensure that appropriate responses and safety measures can be taken. The research also includes experiments to study plumes of colored smoke, as a proxy for the transport of biological particles such as HAB cells, pollen, and pathogens.

The first objective of this research was to explore associations between measured weather conditions and particle concentrations measured above active HABs and HAB sites using drone-based sensor packages.

The second objective was to monitor wind and particle concentrations near freshwater and marine HABs using ground-based sensor packages.

The third objective was to model HAB aerosol behavior at a beach level to predict respiratory irritation.

The fourth objective was to use aerial and ground-based sensors and images of colored smoke to predict particle concentrations at different distances and intensity levels downwind from the source(s).

Modeling the Spread of Airborne Particles Associated with Harmful Algal Blooms and Plumes of Colored Smoke

Landon T. Bilyeu

(General Audience Abstract)

Certain environmental conditions in lakes and oceans can favor unhealthy amounts of algal growth. Overgrowth can lead to harmful algal blooms (HABs). This occurs when algae produce toxins that make the water unsafe for humans and animals to drink. Sometimes these toxins don't stay in the water and can become toxic airborne particles. We need more information to understand what happens to create and transport these airborne toxins produced by HABs. This research aims to monitor particle concentrations and weather to find what conditions lead to more aerosolized toxins. Accurate predictions of high levels of HAB toxins in the air could be used to alert the public. This work utilized colored smoke released outdoors as a visual indicator of particle movement in the air. The specific objectives of this research were to (1) find associations between weather and particle concentrations at lake HAB sites using drone-mounted samplers at a height above 30 feet from the ground, (2) find associations between weather and particle concentrations at lake and ocean HAB sites using samplers at a height of 5 feet from the ground, (3) predict human throat irritation levels from airborne toxins at the beach level, and (4) use a drone sensor, a ground sensor, and simultaneous video footage of a controlled smoke release to visually track airborne particles.

Acknowledgements

This work would not have been possible without the support and opportunities given to me by my co-advisors Dr. David Schmale and Dr. Shane Ross. I am grateful for their guidance and direction which have helped me grow both personally and professionally through my time as a PhD student. I would like to thank my committee Dr. Foroutan and Dr. Hession for helping me to expand my knowledge base and rounding out my research and learning experience. Thank you all for your support.

I would like to thank the members of the Schmale Lab group, Ms. Regina Hanlon, Ms. Hope Gruszewski, and Ms. Niki McMaster for their support in the lab and the field as well as with my writing. You all made Virginia Tech and my time here feel more welcoming and provided invaluable support.

This work was supported in part by grants to David Schmale from the U.S. National Science Foundation (NRI- 2001119) and the Institute for Critical Technology and Applied Science at Virginia Tech (ICTAS-178429), and a grant to HF, SR, and DS from the Global Change Center and the Institute for Society, Culture, and the Environment at Virginia Tech.

Contents

List of Figures

2.5 Wind speed (m/s) over the course of the day. The first two graphs represent August 5th – 6th, 2019 at GLSM. The third graph represents August 8th, 2019 at Lake Erie. The wind speed was determined by our sonic anemometer for August 5th – 7th, 2019, and using GLOS data for August 8th, 2019.

2.6 Airborne particle counts over the course of the day. Data were recorded from a PMS7003 OPC onboard the AirDROPS. The first two graphs show flights that occurred August 5th – 6th, 2019 at GLSM while hovering 10 m over the water. The third graph depicts the flights on August 8th, 2019 while hovering 10 meters over the water at Lake Erie. To the right of each graph is the corresponding wind rose which shows wind direction and speed for each day.

2.7 Airborne particle counts recorded from the OPC onboard the AirDROPS, and windspeed from the sonic anemometer mounted on a flagpole (GLSM) and drone-modeled data for Lake Erie. The first two graphs show flights that occurred August 5th – 6th, 2019 at GLSM while hovering 10 m over the water. The third graph depicts the flights on August 8th, 2019 while hovering 10 m over the water at Lake Erie.

2.8 Comparing total particle counts to obj/mL collected by the impinger during the AirDROPS flights. The graph depicts the total particle count over the 10-min flights for > 0.3 μm particle diameter as well as the obj/mL count in the impinged air samples taken at the same time. Samples 2, 7, 8, 9, 10, 13, 14, and 15 were collected at GLSM, while samples 17-21 were collected at Lake Erie.

2.9 Measured vs predicted particle counts used in the best fit model. The model was made using the wind speed, temperature, wind speed*temperature, and wind direction*temperature.

2.10 Calibration experiments for the OPC in the AirDROPS package. Experiments were performed in a sealed bag filled with air mixed with different aerosolized particle sizes. Experiments 1 and 4 were done with no added particles as a chance to run a zero test for the sensors and give a background of particle levels in the bags. Experiments 2 and 3 were run with aerosolized 1 μm diameter particles, experiments 5 and 6 were run with aerosolized 3 μm diameter particles (data was not recovered from the APS in experiment 6), and experiments 7 and 8 contained both 1 μm and 3 μm particles.

3.1 One sampling location at Lake Anna, VA marked in yellow, and the two beaches in Manasota, FL and Seagate FL in red are marked where sampling was performed. Lake Anna consisted of ground level and drone-based sampling while Manasota and Seagate beaches consisted of only ground level sensing.

3.2 A shows the ground sampling device in location at Seagate Beach FL, December 3, 2019. B shows a closeup of the impinger actively sampling the air while the weather station is running in Florida. C shows the ground sampling device at Lake Anna, Virginia collecting near the lake shore on June 30, 2020. D shows combined drone and ground sampling at Lake Anna.

3.3 Onshore and offshore wind profiles showing wind speed as a factor of altitude for flights taken over Lake Anna over the course of the day on July 7th, broken down based on wind coming from over the land or over the water.

process with the same initial rate (bottom) produces events that are roughly equally spaced in time. The Hawkes process proves to be a good model for many natural processes, which also tend to have events which cluster in time.

5.1 3 panels depicting the smoke release experiments. Panel A shows smoke passing over ground sampling devices with a drone sampler flying overhead. Panel B shows a different configuration of ground sampling devices with high wind speed creating a low plume. Panel C shows the top-down image of smoke release as captured by the drone video camera.

5.2 The method of wind direction processing for each ground sampler with an attached weather sensor. When the wind blew in the 180 degree line from the smoke source to the sampler it was set to 180 degrees and when the wind blew from the sampler towards the smoke source it was set to 0 degrees. Each direction had a range of 1 to 180 degrees. Crosswinds from either direction would be 90 degrees.

5.3 The correlation between wind speed and direction with the particle concentration measured 10 meters from the smoke plume source. Higher concentrations are associated with wind direction blowing the plume towards the sampler, and lower wind speeds are associated with higher particle concentrations when the wind is not directly towards the sampler.

5.4 Optical particle counter measurements to have higher concentrations of smoke the closer the sensor was to the plume source, as seen with OPC A having a higher concentration of particles than OPC B despite similar smoke intensity levels.

5.5 The absorbance measured from each of the 6 high volume samplers. R1 refers to the first sample period, R2 the second sample period, and R3 the third sample period. In R1 Ed samplers B, D, and E were downwind at 7.5, 15, and 25 meters, A and F were crosswind at 15 meters and C was upwind at 15 meters. For R2 and R3 Ed samplers A, B, and C were downwind 5, 10, and 15 meters, D and E were crosswind at 15 meters, and F was upwind at 15 meters. We see as distance increased for our downwind samplers that absorbance decreased, meaning less exposure to smoke was measured as the distance from the plume increased.

5.6 A side view of a period when the drone mounted sensor (DR OPC) was flying above OPC C (12:14:32 PM July 6th, 2023). OPC C is within the plume while the drone sensor was above the plume, which is shown by a high concentration measured from OPC C and a much lower concentration measured from the drone mounted sensor.

5.7 The smoke plume as seen from above by the drone processed into 4 different intensity levels. The edges of the smoke plume near to the source can be seen to be level 2 with the center being level 4. As the distance from the source increased, the center of the plume intensity level tapered off from level 3 (at OPCs A and B) to level 2 (at OPC C), to level 1 before no longer being detected. At the furthest extent of the plume the center was only intensity level 2 with an outside edge of level 1.

5.8 4 panels of processed smoke images as seen from above along with the associated optical particle counter concentration measurements (cm-3). In the top left panel, the edge of the smoke plume intersected with OPCs A and B. In the top right and bottom left panel, the smoke plume engulfed all 3 OPCs with higher intensity levels on OPCs A and B. In the

bottom right panel, the plume drifted away from OPC A. As the plume ascended, OPC B was fully covered, and OPC C was partially covered.

5.9 2 sets of processed smoke images as seen from above along with the associated optical particle counter concentration measurements (cm-3) overlaid on the left image. In the top left and bottom left the smoke plume was divided into smoke intensity bins based on the relative red intensity of the RGB readout of each pixel. In the top right and bottom right panel, the smoke plume was measured by average saturation and the value of each measured pixel was displayed as a continuous color gradient.

5.10 The processed side (top) and top-down (bottom) view of the smoke plume. Processed images had the plume identified via a trained Detectron2 AI and the plume density was color mapped using the averaged saturation and value read at each pixel within the plume.

5.11 The training and validation predicted vs actual plots for the particle concentrations measured by the OPC and predicted by the neural model trained with smoke intensity data. These results had an R-Squared value of 0.612 for the training data and 0.559 for the validation data.

5.12 The training and validation predicted vs actual plots for the particle concentrations measured by the OPC and predicted by the neural model trained with the averaged saturation and value measurements of pixel readings taken near the OPC as seen by the drone video. The empirical prediction equation produced a model that had an R-Squared of 0.532 and a validation prediction R-Squared value of 0.382.

List of Tables

Also given are the false negative rate (also called the miss rate) and the false positive rate.

5.1 Sampler name, start time, stop time, distance, direction from the smoke source, and number of smoke emitters released during sampling period is shown for the sampling equipment during the July 6, 2023, smoke release experiments. Ed refers to the high volume filter samplers. IMP refers to the ground-based sensors containing OPC and weather sensors. DR V refers to the drone collecting video data. DR OPC refers to the drone with the mounted OPC.

5.2 Training and validation data for the model predicting smoke intensity level using particle concentrations as inputs.

Chapter 1. Introduction

1.1 – Background and Motivation

Harmful algal blooms (HABs) are characterized by the proliferation of toxin-producing cyanobacteria and dinoflagellates, commonly referred to as blue-green algae (Anderson et al., 2002). HABs cause adverse effects on human health and wildlife (Backer et al., 2015) through degradation of water and air quality (Kirkpatrick et al., 2011; Birbeck et al., 2019b). HABs not only disrupt the ecological balance of aquatic habitats by outcompeting other organisms for resources and altering food webs, but they also produce a variety of toxins (Backer et al., 2015; Hanlon et al., 2022). *Microcystis* is a genus of cyanobacteria commonly found in lakes and reservoirs, often producing hepatotoxins which can be damaging to the liver (Birbeck et al., 2019b). However, other genera of cyanobacteria produce different types of toxins including neurotoxins (Sutherland, 2021). In lakes, nutrient availability limits growth of these HABs (Anderson et al., 2002; Welch, 2009). The frequency of HAB events appears to be increasing with climate change and extreme weather (Plaas and Paerl, 2021). Recent studies have shown that human activity and climate change may be exacerbating these blooms through an increase in agriculture and urbanization, which increases nutrient pollution and leads to more frequent and severe HABs (Dees et al., 2017; Wells et al., 2020).

Ocean systems can also experience HABs which negatively impact human and marine health (Fleming et al., 2005a; Kirkpatrick et al., 2011). One such ocean HAB, often referred to as Red Tide, is caused by the dinoflagellate *Karenia brevis* (Zohdi and Abbaspour, 2019). Red Tide is prevalent in the Gulf of Mexico and other coastal regions and is characterized by the

production of potent neurotoxins known as brevetoxins (Pierce et al., 2005). Marine HABs, such as red tides, release aerosolized toxins, leading to respiratory problems and skin irritation in exposed individuals (Fleming et al., 2005a; Pierce et al., 2005). However, advances in technology, such as robotic sampling systems and drones, offer innovative solutions for real-time monitoring and data collection, aiding in the formulation of effective management strategies (González-Rocha et al., 2022; Hanlon et al., 2022).

Sea spray aerosol (SSA) is the interface between the ocean and the atmosphere. SSA generation occurs through bubble bursting, wave breaking, and wind-driven processes, releasing particles and organic compounds into the atmosphere (de Leeuw et al., 2011; Cunliffe et al., 2013). These aerosols exhibit significant variability, influenced by factors such as wind speed, and biogeochemical processes within the ocean (O'Dowd and de Leeuw, 2007; Harb and Foroutan, 2019). SSA composition is highly heterogeneous, comprising inorganic salts, organic matter, and biological components derived from marine sources (Meskhidze et al., 2013; Quinn et al., 2015).

Lake spray aerosol (LSA) represents aerosols originating from freshwater bodies, offering insights into the interactions between land and air interfaces. LSA formation primarily occurs through wave breaking, wind shear, and turbulence over freshwater surfaces, leading to the ejection of water droplets and particles into the atmosphere (May et al., 2016; Harb and Foroutan, 2022). These aerosols chemical and physical characteristics, influenced by the composition and biogeochemistry of the underlying lake ecosystem are different than that of SSA (May et al., 2018a; Olson et al., 2020). Compared to sea spray aerosols, research on LSA remains relatively limited, requiring further investigation to better understand the formation mechanisms, and chemical composition. By utilizing drone based sampling

platforms, aerosols can be collected and measured directly at lake and sea surface as well as higher above the surface and on shore (Powers et al., 2018; Hanlon et al., 2022).

Utilizing advanced statistical techniques and machine learning algorithms, researchers are able to identify patterns and make informed predictions based on empirical data, such as detecting smoke presence in images or tracking aerosol movement with sensor measurements. (Ho and Kuo, 2009; Jones and Sall, 2011; Schmale and Ross, 2015). Prediction modeling facilitates the integration of multiple variables and factors, allowing for comprehensive analyses and enhanced predictive accuracy. The utilization of machine learning algorithms, such as neural networks, has enabled the identification of environmental drivers and development of robust forecasting models (Shin et al., 2022). By leveraging historical data on HAB occurrences, water quality parameters, meteorological conditions, and ecological factors, these models can provide probabilistic forecasts of HAB development, bloom intensity, and spatial extent, aiding in early warning and decision-making processes by leveraging weather forecasts with determined weather impact on HAB aerosol behavior. (Stumpf, 2001; Ahn and Shanmugam, 2006; Bulot et al., 2019).

By taking empirical data and integrating it with modeling software, it is possible to predict what areas will be most impacted by HABs (Maguire et al., 2016; Ralston and Moore, 2020). Utilizing multiple monitoring locations and types allows for more accurate HAB predictions (Fang et al., 2019), with larger data sets allowing for more robust and accurate predictions of HAB conditions (Ai et al., 2023). Despite advancements in predicting HABs, challenges such as data availability and the dynamic nature of HABs remain areas of ongoing research (Deng et al., 2018). Through the use of prediction equations and models of HAB impact, there is promise for enhancing preparedness and response strategies, safeguarding

ecosystems, and human well-being from the detrimental effects of this ever-increasing problem.

Traditional aerosol sampling has been performed with ground level sensing devices and has been limited to samples of aerosols within a few meters of the ground or structures (Belyaev and Levin, 1974). By adding drone particle tracking, the study aerosol dynamics and behavior at finer scales than traditional ground-based or satellite observations is possible (Gray et al., 2018). By flying at different altitudes and utilizing advanced sensors, drones can capture detailed information on particle size distributions, vertical profiles, and transport pathways (Bansod et al., 2017; González-Rocha et al., 2023). This enhanced spatial and temporal resolution allows for more accurate modeling of aerosol dispersion and forecasting of air quality conditions, thereby supporting informed decision-making and public health interventions (Pochwała et al., 2020).

Significant advancements have been made in smoke tracking techniques, facilitated by remote sensing technologies, atmospheric modeling, and data assimilation methods (Ho and Kuo, 2009; Zhao et al., 2012). Remote sensing platforms, such as drones, enable the detection and monitoring of smoke plumes over large areas, offering valuable information for wildfire management agencies (McClure et al., 2023). By combining visual remote sensing with drone technology, including lightweight sensors, the particle composition of a smoke plume can be determined (Chen and Huang, 2019). The ability to compare the composition of a smoke plume and particle data is particularly important for use in tracking particles of interest that are not visible. Pollen movement across large distances can be modeled through land use and pollen emission estimates (Prank et al., 2013) and ground sensors as part of the national pollen monitoring network (AAAAI, 2021), however, with

drone-based sensors pollen can be measured directly in the atmosphere (Bieber et al., 2020). Current video and image smoke tracking merely captures the size and movement of visible smoke plumes (Ho and Kuo, 2009; Gupta et al., 2021). By utilizing data collected from drone sensors alongside visual smoke tracking data the predictions of particle movement can be further improved. The combination of particle sensors and video smoke tracking allows for the training of prediction models which can determine the particle concentrations from just collected video of the smoke plume. The opposite is also true, where particle concentrations collected in an array can determine relative plume intensity and a visualization of the plume dynamics can be created for aerosols that may not be visible, such as pollen, pathogens, or HAB cells (Schmale and Ross, 2015).

1.2 Objectives

Overall Goal: The goal of this research is to characterize the influence of weather phenomenon such as wind speed, wind direction, and temperature on measured aerosol levels above and around HABs. This will be done by taking measurements using ground and drone mounted sensors along with water and air sampling techniques.

Objective 1. Explore associations between measured weather conditions and the particle counts measured above and beside active HABs and HAB sites.

Question: What conditions lead to the highest and lowest levels of particle counts in the sampling are?

Hypothesis: Higher wind speeds and lower temperatures are associated with higher particle counts.

Objective 2. Create a model to predict concentrations of particles associated with HABs in the air at downwind sites.

Question: What is the relative risk of aerosolized toxins at downwind sites?

Hypothesis: The risk of exposure downwind to aerosolized toxins is associated with wind and temperature.

Objective 3. Create a model to predict what location will have high levels of HAB aerosols.

Question: What measurable factors most influence a location to be associated with an active HAB?

Hypothesis: Water color and wind direction will be most associated with higher levels of HAB irritation.

Objective 4. Combine visual smoke tracking with weather and particle measurements to improve particle behavior predictions.

Question: Do smoke particles behave in a predictable way based on measured particle concentrations and weather conditions and can different sensing devices be utilized to inform behavior of visible and invisible aerosol plume behavior?

Hypothesis: By utilizing multiple particle and weather sensors alongside video monitoring of smoke movement we will see associations between the movement of the smoke plume and the sensor measurements.

1.3 Organization of Thesis

The objectives of this work will be addressed in the following chapters:

1. Drone-Based Particle Monitoring Above Two Harmful Algal Blooms (HABs) in the USA
2. Monitoring wind and particle concentration near freshwater and marine harmful algal blooms (HABs)
3. Beach-level 24-hour forecasts of Florida red tide-induced respiratory irritation
4. Predicting concentrations of colored smoke using drone imagery and a series of fixed and mobile sensors

1.4 Attributions

Dr. David G. Schmale, III served as co-advisor for this work. Dr. Schmale provided direction on experimental design and writing for all work presented in these manuscripts. He participated in all research activities and lead the sampling missions for data analyzed in Chapters 2 and 3. He is listed as the corresponding author for Chapters 2, 3, and 5.

Dr. Shane Ross served as a co-advisor for this work. Dr. Ross provided guidance with Chapters 2, 3, and 5 as well as being the lead author for Chapter 4.

Dr. Hosein Foroutan served as a committee member and provided guidance throughout the completion of this dissertation.

Dr. Hession Cully served as a committee member and instructed Landon Bilyeu in graduate level coursework regarding hydrology.

Dr. González-Rocha provided experimental analysis advice as well as data and analysis for collected drone measurements from Chapter 3. He also collected data as the drone operator for results outlined in Chapter 3.

Regina Hanlon contributed to experimental design, planning, and writing for experiments outlined in Chapters 2, 3, and 5. She performed the flow cytometry analysis in Chapter 2. She collected data alongside Dr. González-Rocha with ground sampling devices used in Chapter 3.

Chapter 2. Drone-Based Particle Monitoring Above Two Harmful Algal Blooms (HABs) in the USA

Landon Bilyeu, Bryan Bloomfield, Regina Hanlon, Javier González-Rocha, Stephen J. Jacquemin, Andrew P. Ault, Johnna A. Birbeck, Judy A. Westrick, Hosein Foroutan, Shane D. Ross, Craig W. Powers, and David G. Schmale III

Submitted: May 2022

To: Environmental Science: Atmospheres

Status: Accepted September 2022

2.1 Abstract

Little is known about the transport and fate of aerosolized particles associated with harmful algal blooms (HABs). An Airborne DROne Particle-monitoring System (AirDROPS) was developed and used to monitor, collect, and characterize airborne particles over two HABs in Grand Lake St Marys (GLSM) and Lake Erie (LE), Ohio USA in August 2019. The AirDROPS consisted of an impinging device (ID) and an optical particle counter (OPC) mounted on a large commercial quadcopter (DJI Inspire 2). The sensor package was mounted above the airframe to limit the effects of propeller downwash that can corrupt measurements taken below the drone. Twenty flights were conducted 10 m above water level (AWL) at GLSM, and five flights were conducted 10 m AWL at LE. This sampling height was chosen to minimize the effects of propwash on aerosolization from the lake surface. One intercomparison flight was conducted at GLSM over land adjacent to a sonic anemometer mounted on the top of a flagpole 15 m above ground level (AGL). Particle counts generally decreased from morning to afternoon flights, ranging from > 4000 in the morning to < 1000 later in the day. Decreased particle counts were associated with an increase in windspeed that corresponded with time of day, ranging from > 4000 below 4 m/s to < 2500 above 4 m/s. Flow cytometry was used to image particles trapped in a liquid impinger onboard the AirDROPS. Sixty percent (15/25) of the impinger samples contained at least one biotic (fluorescent) object. Impinger samples were also analyzed for a suite of potential cyanotoxins using liquid chromatography–mass spectrometry (LC-MS/MS), but no cyanotoxins were detected in any of these air samples (water samples collected during a similar time contained greater than 20 µg/L microcystins). Additional work is needed to understand the environmental factors associated with the potential aerosolization and transport of cyanobacterial cells and toxins in aquatic environments.

2.2 Introduction

Harmful algal blooms (HABs), caused mostly by toxin-producing cyanobacteria, occur naturally in freshwater systems.(Backer et al., 2015; Watson et al., 2015; Schmale et al., 2019) HABs form as a result of lake conditions favorable to cyanobacterial growth, such as high levels of phosphorus and warmer temperatures.(Anderson et al., 2002) These conditions can occur in areas with high agricultural runoff and are a particular risk to shallow waters. HABs are often associated with high levels of cyanotoxins that pose a significant health threat to humans and domestic animals.(Graham et al., 2010; Bertani et al., 2016) The exposure of HAB associated aerosols has been shown to pose health threats in a *drosophila* model.(Hu et al., 2020a) Furthermore, HABs appear to be increasing in freshwater bodies around the world.(Anderson et al., 2002; Wells et al., 2020)

Research is needed to mitigate HABs, including the development of new low-cost and turn-key technologies to capture, detect, and quantify HAB cells and toxins in water and air.(Anderson et al., 2002; Schmale et al., 2019) Water samples suspected to contain HABs are usually collected by hand from crewed boats and shipped to off-site laboratories for cyanotoxin analyses. Detailed cyanotoxin analyses are usually conducted using liquid chromatography coupled with tandem mass spectrometry (LC-MS/MS), but the high costs of these instruments preclude their widespread use. Commercially available enzyme linked immunosorbent assays (ELISAs) are common for some cyanotoxins such as microcystins (MCs), employing either monoclonal or polyclonal antibodies.(Graham et al., 2010) New low-cost technologies with quick turn-around times are needed to understand threats, manage risks, and mitigate incidents associated with HABs.

Grand Lake Saint Marys (GLSM) is a natural HAB laboratory; the lake has experienced a recurring HAB since 2010.(Jacquemin et al., 2018) LE has also experienced several significant HABs in recent years. A HAB in 2014 near the water treatment plant intake for Toledo, OH led to non-potable water for days.(Steffen et al., 2014) HABs on LE are often associated with the southern and western portions of the lake, likely stemming from increased nutrient input from the Maumee River.(Boyer, 2008) Similar to GLSM, LE has been experiencing HABs for at least the past few decades, due in large part to the highly agricultural watershed and resulting nutrient rich runoff coupled with the shallow depth and bathymetry of the lake.(Brittain et al., 2000)

Lakes with HABs have been shown to produce lake spray aerosols (LSAs) through the breaking of waves and the bursting of bubbles.(May et al., 2016, 2018b) These processes may release HAB-associated particles into the air above the lake surface.(Pietsch et al., 2018) Red tides in the ocean are known to produce aerosolized toxins known as brevetoxins that may irritate the eyes and lungs of humans (Fleming et al., 2005a). Though red tides have been the focus of a considerable amount of research in the past decade (Pierce et al., 2005), relatively little is known about the airborne transport and fate of freshwater HABs and their associated toxins. This information is critical for health advisories issued via water quality experts, and for the communities of people that live on or around contaminated bodies of water.(Carmichael and Boyer, 2016)

A number of different techniques and approaches have been used to study the aerosolization and transport of microorganisms from aquatic environments. May et al. (2016)(May et al., 2016) developed a chamber to study LSA generation under controlled environmental conditions. Pietsch et al. (2018)(Pietsch et al., 2018) used a thin tank to

study wind-induced aerosolization of the bacterium *Pseudomonas syringae*. Harb et al. (2019)(Harb and Foroutan, 2019) used a chamber to study the potential impact of salinity on the aerosolization of microorganisms from aquatic environments. Powers et al.(Powers et al., 2018) developed an extensive sampling tower for an uncrewed surface vehicle (USV) to collect microorganisms and monitor particle sizes in the atmosphere above a salt pond in Falmouth, MA, USA and a freshwater lake in Dublin, VA, USA. The bioaerosol-sampling system featured in that work included a series of 3D-printed impingers, two different optical particle counters, and a weather station. A small, uncrewed aircraft system (sUAS; a fixed-wing drone) was used in a coordinated effort with the USV to collect microorganisms 50 m above the surface of the water. Samples from the USV and sUAS were cultured on selective media to estimate concentrations of culturable microorganisms. In this manuscript, we extend these prior efforts to the development and use of a unique Airborne DROne Particle-monitoring System (AirDROPS) to collect and characterize aerosols directly over HABs in two freshwater lakes. The AirDROPS consisted of low-cost and lightweight sensors, including an impinging device (ID) and an optical particle counter (OPC) mounted above a large commercial quadcopter (DJI Inspire 2). The OPC used on the AirDROPS can characterize particles up to 10 μm, which is above the size range of cells of *Microcystis* which have been reported to be 1-7 μm.(May et al., 2018b) Laboratory calibration experiments were conducted to assess the reliability of the OPCs after a period of use.(Bulot et al., 2019; Giordano et al., 2021) We hypothesized that particle size distributions above two freshwater HABs would be associated with windspeed, wind direction, and temperature. The specific objectives of our work were to: (1) design an automated drone-based sampler to monitor particle sizes in the atmosphere and collect

HAB cells and toxins, (2) use the drone-based sampler to monitor the distribution of particles in the atmosphere directly above two freshwater HABs, and (3) observe potential associations of wind direction, windspeed, and temperature with particle counts from the drone-based sampler.

2.3 Materials & methods

2.3.1 Study sites

GLSM is an artificial lake in western Ohio with a surface area of 54.6 square kilometers and average depth of about 2 m.(Jacquemin et al., 2018) In the GLSM watershed, over 90% of the land use is row crops or pastureland which leads to a high amount of nutrient pollution into the lake.(Hoorman et al., 2008) The shallow lake warms to between 20 and 30 °C in the summer months.(Steffen et al., 2014) The warmer waters and higher nutrient load in the lake allow the cyanobacteria to outcompete other algae in the lake, creating a bloom of toxin producing cyanobacteria. Samples were collected over five consecutive days between 5-9 August 2019 at GLSM and LE in Ohio, USA (LE). Drone sampling missions were conducted 10 m above the water surface at coordinates 40.54, -84.51 and 41.70, -83.46 (**Table 1**) in order to obtain unique measurements of collected aerosols and particle counts at heights above the water surface that could not be reached by boat. Wind speed and direction were collected by an anemometer attached to a flagpole at coordinates 40.54, -84.51. Due to the lack of an unobstructed space to place the stationary wind sensor at LE (there were tall trees at the sampling location that obstructed the sampling domain), wind data were collected through a separate drone flown simultaneously 10 m above the water. Wind data from these flights were gathered using previously published methods

where the motion of the drone was used to infer windspeed and wind direction .(González-Rocha et al., 2019, 2020) One of the flights at GLSM was also used for comparison with a concurrent separate drone flight measuring wind conditions and was flown adjacent to a sonic anemometer mounted on the top of a 15 m flagpole (**Flight 20, Table 1**).

Table 1. Details on AirDROPS sampling missions at GLSM and LE. AirDROPS was used to collect and characterize particles over two HABs. The AirDROPS consisted of an impinging device and an optical particle counter mounted above a large commercial quadcopter. Twenty flights were conducted 10 m above water level (AWL) at GLSM, and five flights were conducted 10 m AWL at LE. One sensor intercomparison mission (flight 20) was conducted over land adjacent to a sonic anemometer mounted on the top of a flagpole 15 m above ground level (AGL).

Flight #	Lake	Mission	Date	Start time (ET)	Stop time (ET)	Sample time (min.)	Height above water (m)	GPS of sampling location	OPC Count per mL	Red Channel Obj/mL
1	GLSM	Sample above lake surface	5-Aug-19	8:04 AM	8:17 AM	13	10	40.544873, -84.510843	45.3	0.0
2	GLSM	Sample above lake surface	5-Aug-19	9:07 AM	9:17 AM	10	10	40.544873, -84.510843	51.1	413.5
3	GLSM	Sample above lake surface	5-Aug-19	10:09 AM	10:19 AM	10	10	40.544873, -84.510843	29.4	0.0
4	GLSM	Sample above lake surface	5-Aug-19	11:06 AM	11:16 AM	10	10	40.544873, -84.510843	21.2	0.0
5	GLSM	Sample above lake surface	5-Aug-19	12:03 PM	12:13 PM	10	10	40.544873, -84.510843	22.1	0.0
6	GLSM	Sample above lake surface	5-Aug-19	1:05 PM	1:15 PM	10	10	40.544873, -84.510843	22.1	0.0
7	GLSM	Sample above lake surface	5-Aug-19	2:07 PM	2:17 PM	10	10	40.544873, -84.510843	16.3	871.4
8	GLSM	Sample above lake surface	5-Aug-19	3:03 PM	3:14 PM	11	10	40.544873, -84.510843	11.2	461.2
9	GLSM	Sample above lake surface	6-Aug-19	8:10 AM	8:20 AM	10	10	40.544873, -84.510843	54.5	2535.1
10	GLSM	Sample above lake surface	6-Aug-19	9:06 AM	9:16 AM	10	10	40.544873, -84.510843	36.4	3984.5
11	GLSM	Sample above lake surface	6-Aug-19	10:04 AM	10:14 AM	10	10	40.544873, -84.510843	18.9	nd
12	GLSM	Sample above lake surface	6-Aug-19	10:36 AM	10:46 AM	10	10	40.544873, -84.510843	19.1	0.0
13	GLSM	Sample above lake surface	6-Aug-19	11:07 AM	11:17 AM	10	10	40.544873, -84.510843	23.1	0.0

14	GLSM	Sample above lake surface	6-Aug-19	11:35 AM	11:42 AM	7	10	40.544873, -84.510843	17.3	0.0
15	GLSM	Sample above lake surface	6-Aug-19	12:43 PM	12:53 PM	10	10	40.544873, -84.510843	11.5	0.0
16	GLSM	Sample above lake surface	6-Aug-19	1:06 PM	1:16 PM	10	10	40.544873, -84.510843	35.7	0.0
17	GLSM	Sample above lake surface	6-Aug-19	1:34 PM	1:44 PM	10	10	40.544873, -84.510843	0.0	2030.8
18	GLSM	Sample above lake surface	6-Aug-19	2:06 PM	2:16 PM	10	10	40.544873, -84.510843	0.0	853.6
19	GLSM	Sample above lake surface	6-Aug-19	2:37 PM	2:47 PM	10	10	40.544873, -84.510843	0.0	2518.2
20	GLSM	Sensor calibration	7-Aug-19	8:18 AM	8:28 AM	10	10	40.544074, -84.508220	0.0	831.1
21	LE	Sample above lake surface	8-Aug-19	11:36 AM	11:46 AM	10	10	41.702472, -83.463598	5.54	2737.2
22	LE	Sample above lake surface	8-Aug-19	12:07 PM	12:17 PM	10	10	41.702472, -83.463598	5.68	5817.6
23	LE	Sample above lake surface	8-Aug-19	1:07 PM	1:17 PM	10	10	41.702472, -83.463598	5.37	2509.8
24	LE	Sample above lake surface	8-Aug-19	1:37 PM	1:47 PM	10	10	41.702472, -83.463598	5.38	2578.4
25	LE	Sample above lake surface	8-Aug-19	2:09 PM	2:14 PM	5	10	41.702472, -83.463598	5.21	2535.1

2.3.2 Airborne Drone Particle-monitoring System

The AirDROPS was designed and deployed for sampling bioaerosols and monitoring particle size distributions. The sampler was constructed using a 38.5 mm diameter by 290 mm length PolyPropylene tube and Polylactic Acid 3D printer components (**Figure 1A**). The sampler was mounted on top of the drone airframe (**Figure 1B**) to limit the effects of propeller downwash that can corrupt measurements taken below the drone.(de Boisblanc et al., 2014; Nolan et al., 2018) The sampler was powered via a single 3.7V 3000mAH 15A

Lithium-Ion battery (Samsung 30Q INR 18650) that was changed out with every flight. An impinger was designed using a stainless-steel tube and PolyCarbonate 3D printed components to allow for high temperature sterilization by autoclave and field disinfection using ethanol. The impinger was based on a design previously described by Powers et al., 2018(Powers et al., 2018) adapted for use with a 15 mL polypropylene sterile conical centrifuge tube (CLS430791, Corning, Millipore Sigma). An aliquot of 2.5 mL of sterile water was added to the 15 mL conical tube immediately prior to each sampling mission. Two micro vacuum pumps (PN: SC3101PM, 21 Hualun Sci & Tech Pk 1st Ind Zn Fenghuang Village, Fuyong Town, Shenzhen, Guangdong, China) were used in parallel to supply a flow rate of 0.6 L/min to the impinger. This flow rate was determined using an FTS Flow Calibrator from ARA Instruments (Eugene, OR, USA), and was optimized to ensure that the impinging fluid was not evacuated from the tube during the sampling mission (i.e., higher flow rates caused water to escape the tube into the vacuum pump). The collection efficiency of the impinger has been reported previously by Powers et al. (Powers et al., 2018) to be 75% for 1 μm polysterene latex beads and 99% for 3 μm polysterene latex beads. The inlet to the impinger was located 330 mm above the horizontal plane of the drone propellers to limit fouling of the sensor due to propwash (**Figure 1B**). An optical particle counter (PMS7003, Plantower, Shunyi District, Beijing, China) was used to record six particle size bins, each greater than 0.3, 0.5, 1.0, 2.5, 5.0, and 10.0 μm. PM_1, $PM_{2.5}$, and PM_{10} numbers were calculated internally by the PMS7003. The inlet to PMS7003 sensor was located 312 mm above the horizontal plane of the drone propellers (**Figure 1B**). An environmental sensor (BME280, Bosch Sensortec GmbH, Gerhard-Kindler-Strasse 9, 72770 Reutlingen Germany) was used to measure ambient temperature,

relative humidity, and barometric pressure. The BME280 was located 132 mm above the horizontal plane of the drone propellers. A GPS module (GPS-13740, SparkFun Electronics, 6333 Dry Creek Parkway, Niwot, CO 80503) was used for location and time data. All available data was recorded by the ARM based microcontroller to a secure digital (SD) card at 1Hz. The combined weight of the AirDROP including a battery and a 15 mL conical tube with 2.5 mL of sterile water was 587 g. This is below the safe limit operations of the Inspire 2 platform payload, which the manufacturer has specified as no greater than 810 g.(Inspire 2 - Product Information - DJI, n.d.) With the AirDROPS installed, the Inspire 2 platform has a reasonable (safe) flight time of about 15 minutes. Our sampling missions were designed with this limit in mind (10 minutes), providing enough time for takeoff, transit to and from the sampling location, and return to home for landing (about two minutes, given the location of our takeoff and landing spot).

Figure 1. (A) Engineering model of the AirDROPS package. (B) The AirDROPS attached to the DJI Inspire 2 platform. (C) Intercomparison flight of the AirDROPS adjacent to the sonic anemometer mounted on the flagpole. (D) Sampling mission at GLMS, 10 m above the surface of the water. (E) Drone image and aerial view of the sampling location at LE to the right of the point in the image.

2.3.3 Flight operations

For each sampling mission, the AirDROPS was flown into position, and held in 'Positioning mode' at a constant altitude of 10 m above the lake surface (**Figure 1D**). This height was chosen to reduce the impact of downwash on the lake surface as well as to measure aerosol levels higher above the HAB source than had been done previously using

watercraft. The sensor package was powered on using a photoelectric switch mounted over the left rear green LED light on the Inspire 2. The lights were powered on in the DJIGO4 app, starting the sensor package over water once the drone was in the correct position. The sensor package remained on for a period of 10 min. After 10 min, the sensor package was powered off using the photoelectric sensor, and the drone was returned home for landing.

2.3.4 Flow cytometry of impinger samples collected 10 m above the HABs

The concentration of impinged particles from the atmosphere above freshwater lake sites was determined with an Imaging Cytometer (Amnis ImageStream MarkII). The impinged aerosols were counted as obj/mL at 60X magnification in both the brightfield (BF) (457/45 nm bandpass filter) and red channels (642 nm excitation and 702/86 nm emission wavelength) (**Figure 2**). Phycocyanins are the light harvesting pigments found in cyanobacteria and these pigments are optimally excited in the red range with an emission spectrum that can be captured between 630 nm and 800 nm. Samples were stored at -20°C, thawed, and equilibrated at room temperature, prior to being run. One mL of the impinged liquid sample was spun twice at 3,000 x gravity for five minutes. Two aliquots of 42 µL were immediately recovered from the liquid near the bottom of the tube, with care to avoid any debris on the tube bottom. Molecular biology grade water was filtered with a 0.2 µm filter and used as a blank in the machine before running samples.

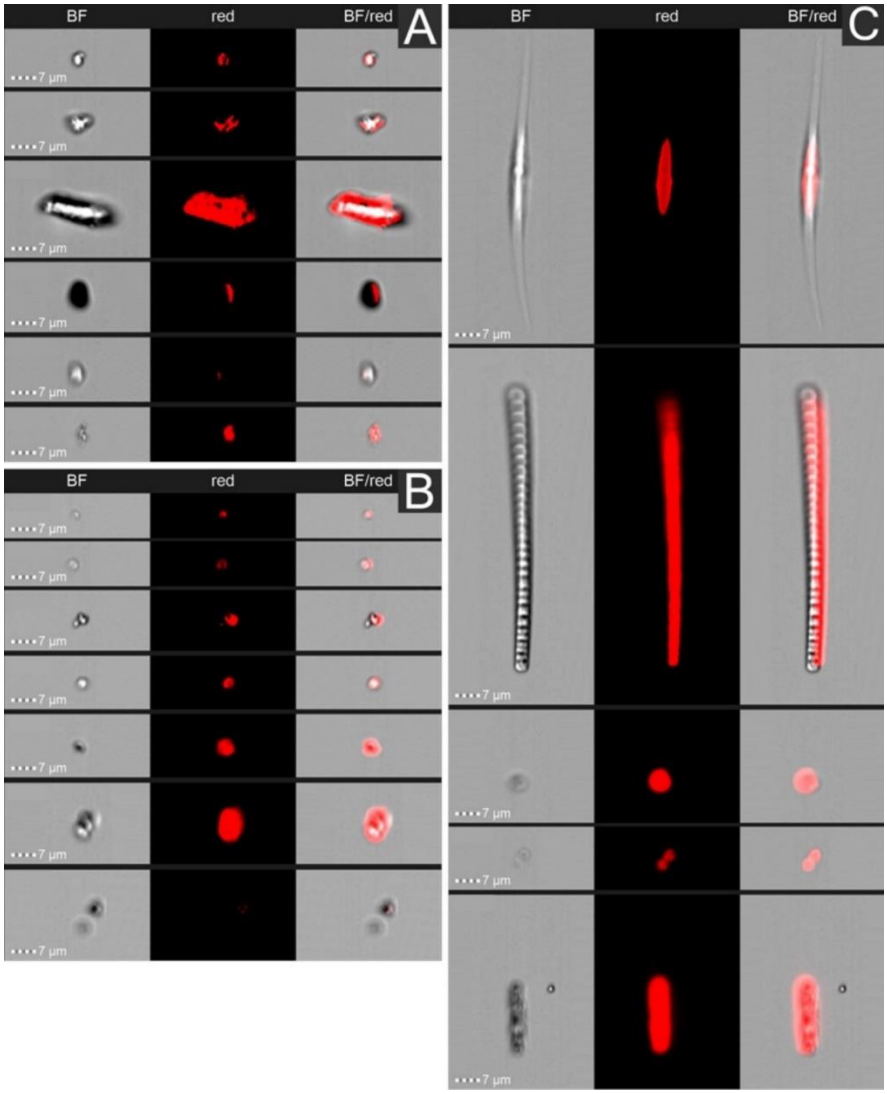

Figure 2. Selected images from flow cytometry analyses of impinger samples from the AirDROPS. **(**A) Objects from an impinger sample collected above GLSM showing brightfield, red filter, and combination of the two. (B) Objects from an impinger sample collected above LE showing brightfield, red filter, and combination of the two. (C) Objects from a lake water sample from LE showing brightfield, red filter, and combination of the two.

Due to the predicted low number of putative captured biotic aerosols, a 3-min run time was standardized for each impinged sample. In a previous study with natural and

simulated rain, samples were run for three min to obtain obj/mL outputs.(Powers et al., 2018) These authors determined that 3-min sample runs showed similar size distributions relative to samples that reached 1000 obj/mL in less than three min, and the background level of bacteria in the nucleic acid staining dye in sterile control water was 297 ± 82 DNA-containing particles per 10 µL (n=3). We did not use a nucleic acid staining dye in this study. Instead, the total obj/mL data for biotic particles was captured in the red channel to eliminate abiotic debris that might give rise to a false count in the BF channel alone. The objects counted in the red channel were considered to be biotic in origin, regardless of fluorescence level. Sample run focusing was achieved with SpeedBead® reagent beads (Amnis Cat. #400040) during data acquisition. The beads were removed by gating before object counts were generated for each run. To obtain total aerosolized particles captured, the BF channel data was corrected by subtraction of particles within the SpeedBead capture range. These counts were sorted by the size of the objects into bins of 0.13 - 1.13, 1.13 - 1.60, 1.60 - 1.95, 1.95 - 2.76, 2.76 - 3.91, 3.91 - 5.64, 5.64 - 6.91, 6.91 - 7.98, and 7.98 - 8.92 µm radius objects. The radius was calculated using the total size of the objects and assuming a circular (spherical) shape.

To calculate the total number of aerosolized particles collected during each impinger collection, the average of the total BF obj/mL for the zero red channel runs were assigned to a discrete size bin. The mean of this total obj/mL (for each size bin) was subtracted from the corresponding total BF obj/mL (for each size bin) for each run that contained a positive fluorescent object in the red channel. By subtracting the average particle count data for samples with zero objects in the red channel, from those with red objects, we were able to normalize by correcting for abiotic debris particle capture.

2.3.5 Cyanotoxin analyses using LC-MS/MS

Toxins from cyanobacteria were detected using LC-MS/MS methods described in Birbeck et al. 2019.(Birbeck et al., 2019a) Sample analytes were loaded into a Thermo Scientific TSQ Altis™ triple quadrupole mass spectrometer (Thermo Scientific, Waltham, MA, USA) with an EQuan MAX Plus™ system and then separated on a Thermo Accucore aQ, 50 × 2.1 mm, 2.6 µm particle size column. A standard curve was prepared between 0.5-500 ng/L, with detection limits for MCs and nodularin being between 0.5-10 ng/L. An electrospray ionization source was used in positive ion mode. Additional details regarding these methods are provided in Hanlon et al. (2022)[31] and reference ions are provided in Supplementary Table 1. The TraceFinder™ EFS 4.1 software package was used to ensure proper cyanotoxin identification (Supplementary **Table 1**).

2.3.6 Particle counts 10m above the HABs

The PMS7003 was used to count particles six particle size bins, each greater than 0.3, 0.5, 1.0, 2.5, 5.0, and 10.0 µm diameter in 0.1 L of air, and had a sample rate of about 1 Hz. The sampling occurred over 10-min intervals in tandem with the drone-based impinger. Airborne particle counts were measured according to the times shown in **Table 1**. The data collected was saved to an SD card in comma-separated values (*CSV*) file format and transferred before clearing the SD card to prepare for the next flight.

2.3.7 Ground-based measurements of windspeed and wind direction

At GLSM, an Atmos 22 sonic anemometer weather station was aligned north with a compass and raised on a flagpole to a height of 15 m where it recorded wind speed and

direction measurements every 15 s. Data were saved to an SD card and collection was run from 8:00 until 16:00 local time, daily. The same ground-based anemometer was also used at LE, but trees obstructed this sensor during flight operations so local wind data for the LE flights were determined from drone-based measurements of wind.(González-Rocha et al., 2022) These measurements were taken every second and matched with the time recorded on the AirDROPS to align particle count measurements with the wind speed and direction calculations.

2.3.8 Drone-based wind velocity measurements

Drone-based wind velocity measurements were derived from a 3DR Solo quadrotor using the model-based wind estimation technique described in (González-Rocha et al, 2019; 2020).(González-Rocha et al., 2019, 2020) With this method, wind velocity is inferred from wind-induced vehicle motion perturbations experienced as the drone sustains hovering flight. The general accuracy of this drone-based wind sensing approach has been demonstrated through previous experiments where drone, sonic anemometer, and a Sonic Detection and Ranging instrument (SoDAR) wind velocity measurements have been compared at various heights above ground level.(Nolan et al., 2018; González-Rocha et al., 2019, 2020)

2.3.9 Optical Particle Counter Calibration Experiments

The initial OPC calibrations were done according to the procedure outlined in Powers et al., 2018.(Powers et al., 2018) The accuracy of the OPC used onboard the AirDROPS was assessed in a series of controlled laboratory experiments against an Aerodynamic Particle

Sizer (APS, Model 3321, TSI Incorporated, Shoreview Minnesota, USA). Briefly, particles of known sizes (1 and 3 microns) were released into a sealed bag and measurements from the OPC were compared to the APS.

2.3.10 Data analyses

Data were saved in CSV files and were trimmed and aligned in Microsoft Excel. Statistical analyses were performed with JMP Pro Version 17 software (Cary, North Carolina, USA). A model was fit using the JMP neural network to create a prediction equation for GLSM which utilized wind speed, wind direction, and temperature to predict the particle count. The neural network weighs inputs from a provided dataset to create a prediction equation that will estimate a specific output parameter. The model was set up to create three hidden node equations that combine into an overall theta equation. The theta equation predicts the particle count from the provided weather data. The program adjusts the values in the hidden node equations and overall theta equation until it fits the best curve to the data.(Gotwalt, 2011; Chen and Chen, 2020) To get the best fit, the model was trained using all of the data collected from the sampling periods of August 5th and August 6th, 2019 for which we had both weather data and particle counts. The model was trained with a randomly selected 2/3^{rds} of the collected data, and utilized the remaining 1/3rd as verification for the prediction equation. This resulted in 368 measurements to train the model, and another 184 to verify the model.

2.4 Results

2.4.1 Flights

Twenty-one flights were conducted at GLSM, and five flights were conducted at LE (**Table 1**). Twenty-five of the flights were conducted 10 m above the surface of the water (**Table 1)**. One of the flights at GLSM was used to calibrate the drone sensor package (**Flight 20, Table 1**), and was flown adjacent to a sonic anemometer mounted on the top of a flagpole (**Figure 1C**).

2.4.2 Wind direction and wind speed

The wind direction was consistent across the lakes and toward the shore-based operations for all the sampling missions performed at the two lakes (**Figures 1 and 4**). For GLSM, the sonic anemometer (mounted on the flagpole) recorded wind speeds from 0 – 10 m/s **(Figure 4)**, and wind directions ranging from a source of 150 – 300 degrees (**Figure 3**). At GLSM, windspeed increased from morning to afternoon flights (**Figure 4**). At LE, windspeed was variable and ranged from 1 to 12 m/s across all sampling missions (**Figure 4**).

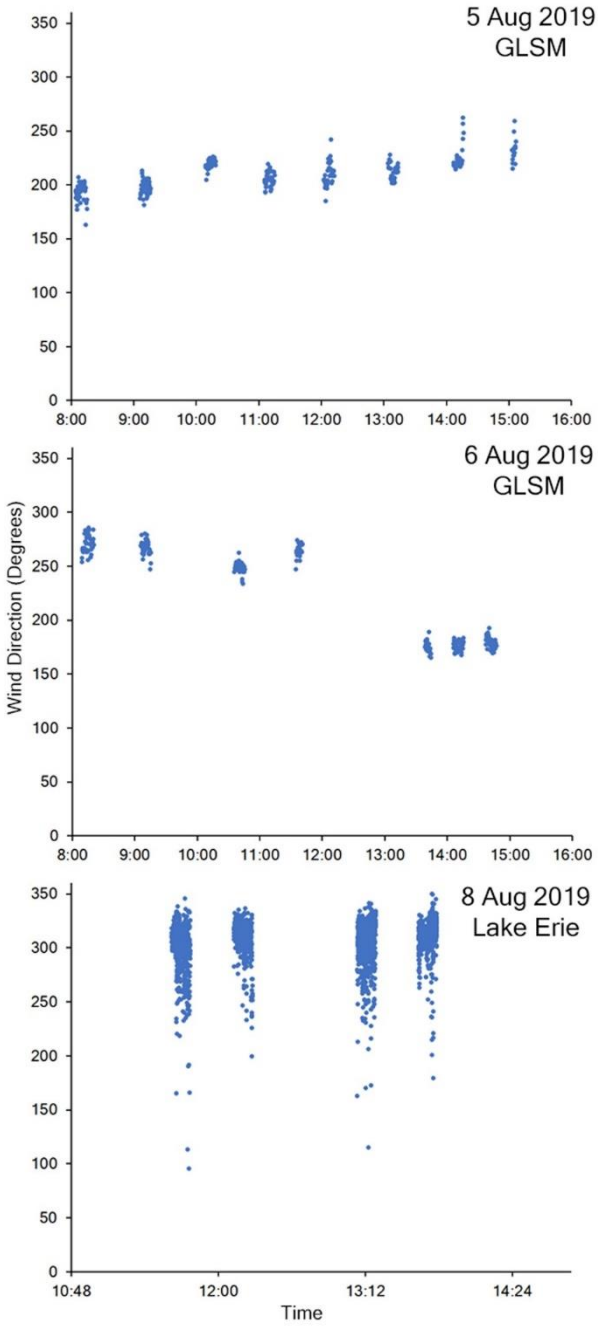

Figure 3. Wind direction (degrees) over the course of the day. The first two graphs represent August 5th – 6th, 2019 at GLSM. The third graph represents August 8th, 2019 at LE. The wind direction was determined using a sonic anemometer for August 5th – 7th, 2019, and using GLOS data for August 8th, 2019.

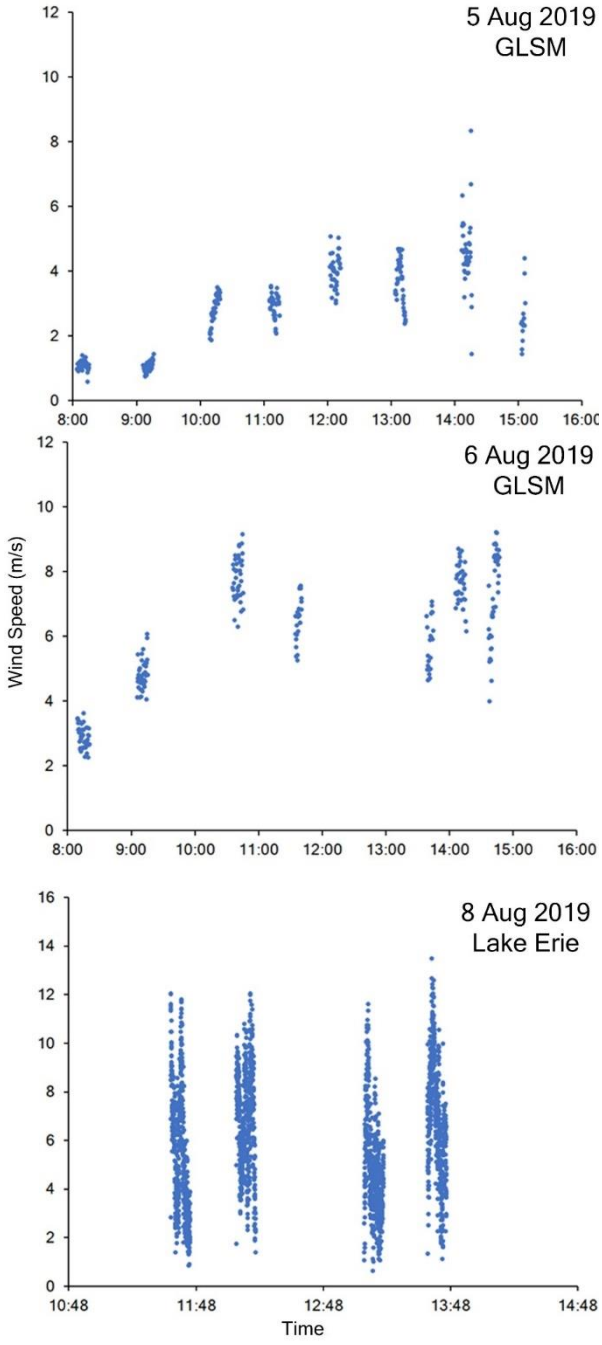

Figure 4. Wind speed (m/s) over the course of the day. The first two graphs represent August 5th – 6th, 2019 at GLSM. The third graph represents August 8th, 2019 at LE. The wind speed was determined by our sonic anemometer for August 5th – 7th, 2019, and using GLOS data for August 8th, 2019.

2.4.3 Particle counts

At GLSM, airborne particle counts generally decreased from morning to afternoon flights (**Figure 5**). We observed decreased particle counts at GLSM associated with an increase in windspeed from morning to afternoon (**Figure 6**). For the size bin of 0.3 – 0.5 µm diameter, particle counts per 0.1 L of air ranged from about 1,000 (afternoon flights) to 6,000 (morning flights) per measurement (**Figure 5**). For the size bin of 0.5 – 1.0 µm diameter, particle counts ranged from about 300 (afternoon flights) to 1,600 (morning flights) per measurement (**Figure 5**). For the size bin of 1.0 – 2.5 µm diameter, particle counts ranged from about 30 (afternoon flights) to 250 (morning flights) per measurement (**Figure 5**). For larger size bins (2.5 – 5.0, 5.0 – 10.0, and 10.0+ µm), particle counts ranged from 0 to 30 per measurement (**Figure 5).**

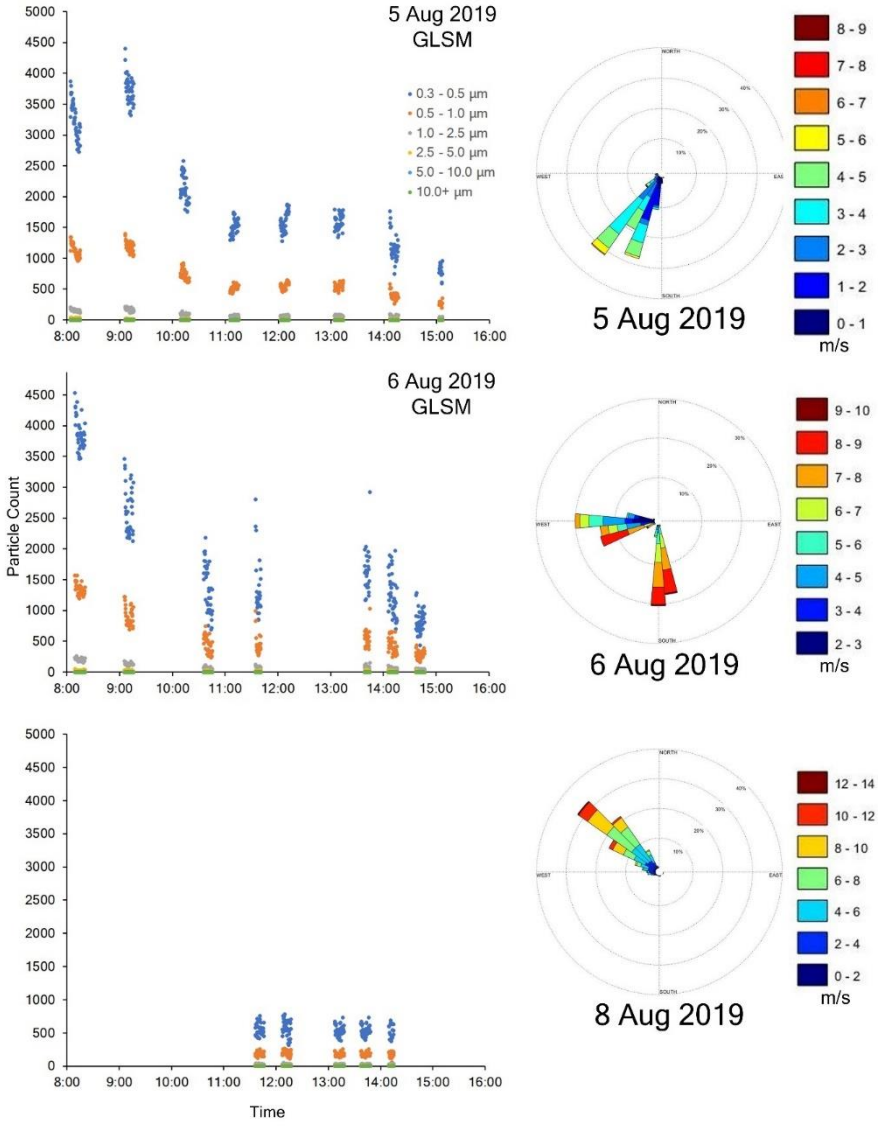

Figure 5. Airborne particle counts over the course of the day. Data were recorded from a PMS7003 OPC onboard the AirDROPS. The first two graphs show flights that occurred August 5th – 6th, 2019 at GLSM while hovering 10 m over the water. The third graph depicts the flights on August 8th, 2019 while hovering 10 meters over the water at LE. To the right of each graph is the corresponding wind rose which shows wind direction and speed for each day.

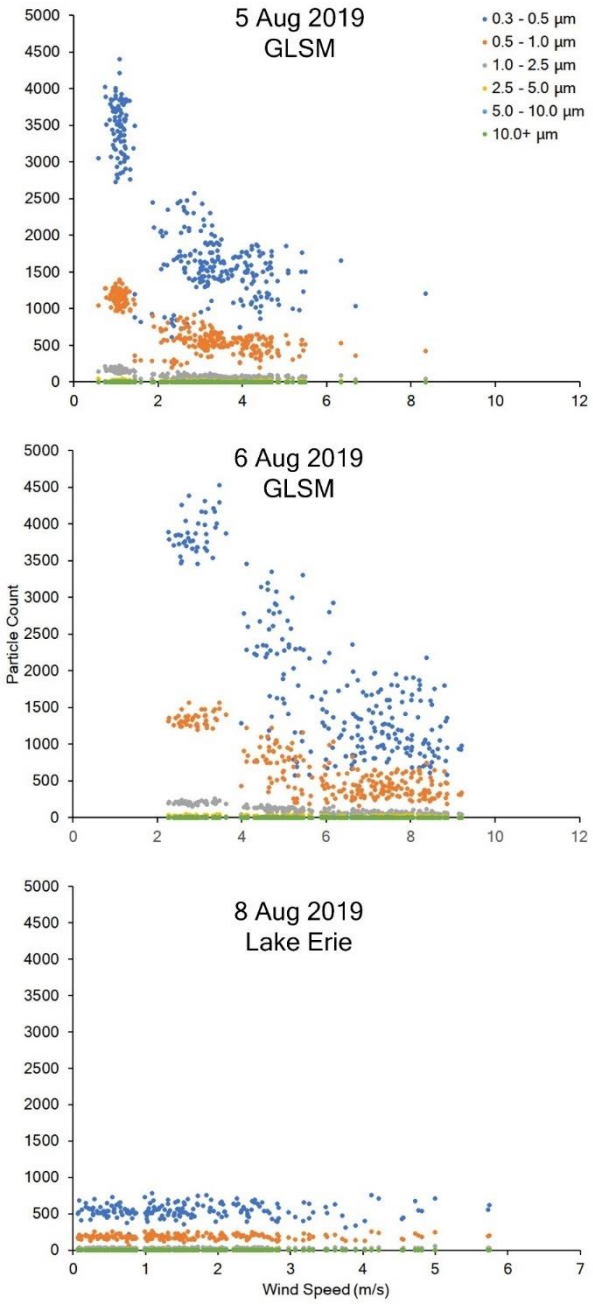

Figure 6. Airborne particle counts recorded from the OPC onboard the AirDROPS, and windspeed from the sonic anemometer mounted on a flagpole and drone-modeled data for LE. The first two graphs show flights that occurred August 5th – 6th, 2019 at GLSM while hovering 10 m over the water. The third graph depicts the flights on August 8th, 2019 while hovering 10 m over the water at LE.

At LE, airborne particle counts were generally lower than GLSM and consistent from morning to afternoon flights (**Figure 5**). At the time LE was not experiencing an algal bloom at the severity of the one in GLSM, which could have contributed to the lower particle counts. There was no association with particle counts with windspeed (**Figure 6**). For the size bin of 0.3 – 0.5 µm diameter, particle counts ranged from about 400 to 1,150 per measurement (**Figure 5**). For the size bin of 0.5 – 1.0 µm diameter, particle counts ranged from about 100 to 300 per measurement (**Figure 5**). For the size bin of 1.0 – 2.5 µm diameter, particle counts ranged from about 20 to 35 per measurement (**Figure 5**). For larger size bins (2.5 – 5.0, 5.0 – 10.0, and 10.0+ µm), particle counts ranged from 0 to 2 per measurement (**Figure 5).**

At GLSM when looking at particle counts over time, we saw the particle count decrease significantly as the day went on, dropping to as little as $1/6^{th}$ the morning particle count levels (**Figure 5**). During our sampling throughout the day. the windspeed increased by 2 to 3 times the morning speed (**Figure 4**), but the wind direction only slightly shifted and was always coming from off the lake. At LE, we saw lower average particle counts than at GLSM but had similar wind source distribution with over 90 percent of wind source direction coming from between 270 and 360 degrees which was off the lake.

2.4.4 Flow cytometry and cyanotoxin analyses of impinger samples

Selected panels of fluorescent objects present in the impinger samples are shown in **Figure 2**. Sixty percent (15/25) of the impinger samples contained at least one biotic (fluorescent) object, ranging from 1 to 7 obj/mL (**Figure 2**). Total biological objects counted in the R1 channel were sorted by size with the majority falling between 1.95 and 3.91 µm (Figure 7).

When comparing total particle counts and object concentrations, no association was observed (**Table 1**). However, despite lower particle counts at LE there were larger numbers of objects observed in the impinger (**Table 1**). Impinger samples were also analyzed for a suite of cyanotoxins using LC-MS/MS, but no cyanotoxins were detected in any of the samples. Water samples collected during a similar time contained greater than 20 µg/L microcystins(Hanlon et al., 2022).

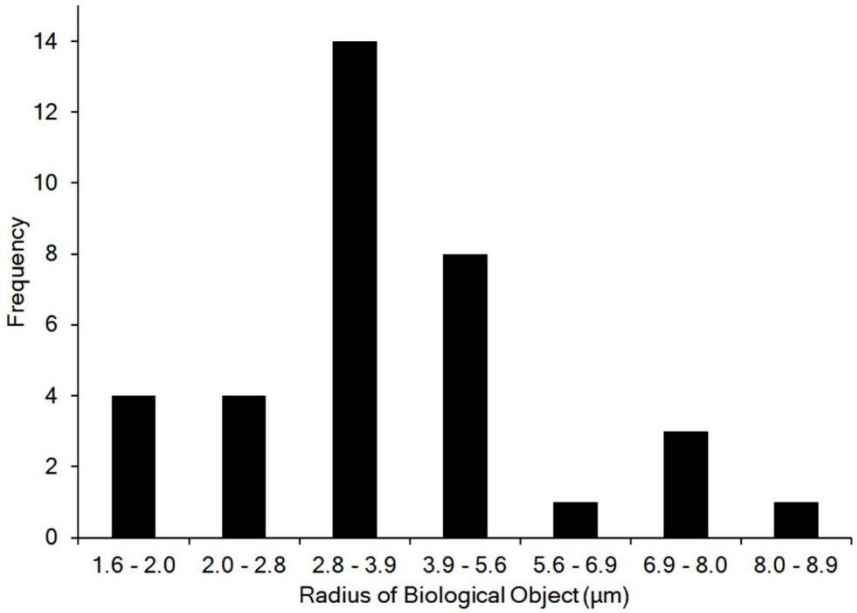

Figure 7. Biological object frequency by size from collected air impinged samples onboard the AirDROPS. The graph depicts object counts sorted by size with radius size bins from 1.60 - 1.95, 1.95 - 2.76, 2.76 - 3.91, 3.91 - 5.64, 5.64 - 6.91, 6.91 - 7.98, and 7.98 - 8.92 µm. The size bins were determined by assuming a spherical shape and calculating the radius of an object from its recorded size in the flow cytometer.

2.4.5 Predicting particle counts as a function of environmental parameters

Particle counts > 0.3 µm from August 5 were observed as a function of wind speed, wind direction, and temperature (**Figure 8**). **Figure 8** shows the actual measured particle counts

plotted against the model predicted versions which results in an optimized model with a R Square of 0.87 and a validation prediction with a R Square of 0.86. The hidden node equations and overall prediction equation, are as follows:

H1 = tanh(.5*(0.2565*Wind_Speed_m_s_ + -0.0022*Wind_Direction_Deg_ + 0.5451*Temperature_C_ + -14.13));

H2 = tanh(.5*(0.1432*Wind_Speed_m_s_ + 0.0036*Wind_Direction_Deg_ + 1.269*Temperature_C_ + -34.90));

H3 = tanh(.5*(-0.3080*Wind_Speed_m_s_ + -0.0092*Wind_Direction_Deg_ + -0.1154*Temperature_C_ + 6.022));

THETA1=-3913*H1 + 881.3*H2 + -901.7*H3 + 3583

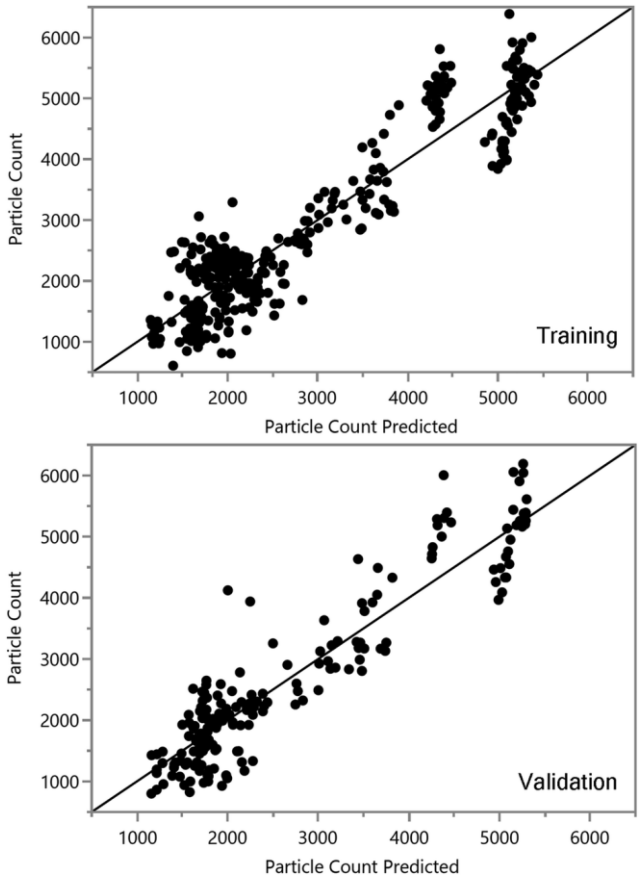

Figure 8. Measured vs predicted particle counts used in the best fit model. The graph on the top panel shows the fit of the model on the training set of data, while the graph on the bottom shows the fit of the validation set of data. The model was made using the wind speed, temperature, and wind direction through the JMP Pro neural network modeling. The model was trained on two days of collected data, and verified on a random subset of the collected data that was not used to train the model.

This model based on a neural network allowed for a prediction of the particle counts in the air above the HAB based on weather conditions.

2.5 Discussion

Little is known about the airborne fate and transport of HABs and their associated toxins. To address these knowledge gaps, we developed and deployed an airborne drone particle-monitoring system (AirDROPS) to collect and characterize aerosols directly over HABs in two freshwater lakes (GLSM and LE), each with different size and conditions that impact aerosolization processes. The AirDROPS consisted of an impinging device and an optical particle counter mounted above a large commercial quadcopter. Twenty flights were conducted 10 m above water level (AWL) at GLSM, and five flights were conducted 10 m AWL at LE. One intercomparison flight was conducted at GLSM over land adjacent to a sonic anemometer mounted on the top of a flagpole 15 m above ground level (AGL). Though airborne concentrations of particles have been reported over water using uncrewed boats,(Powers et al., 2018) to our knowledge, the work described here represents the first drone-based measurements of airborne particle counts directly over HABs.

Airborne particle size distributions varied with increasing windspeed for GLSM. Particle counts generally decreased from morning to afternoon flights, and the decreased particle counts were associated with an increase in windspeed. In contrast, LE particle counts were much lower, and we did not observe significant trends in particle counts with respect to wind direction, wind speed, or time of day. Airborne particle concentrations have been shown to be associated with windspeed and wind direction above a lake surface.(Powers et al., 2018) The time of day plays a role in the conditions affecting windspeed and direction through diurnal cycling.(VanCuren et al., 2012) In cases of higher windspeeds, it has previously been shown to correlate with a decrease in both fine and course aerosols in the ocean.(Pant et al., 2008; Montero et al., 2016; Dueker et al., 2017) In

the case of GLSM, the relatively small size and depth may cause less wave formation and breaking than we would see in large lake spray or sea spray studies, instead likely having aerosol production limited to the surf zone and mechanical disturbances of the surface. LE, however, would be more likely to produce larger numbers of aerosols from wave breaking and bubble-bursting due to the larger size and depth.(May et al., 2018b) Previous studies have shown a difference in particle counts with respect to wind direction when it caused a switch from offshore to onshore winds as wind can drive droplet formation from the water surface.(Hu et al., 2020a; Ross et al., 2022) Our drone sampling missions were conducted exclusively during onshore winds, so consequently we were unable to examine potential associations of particle counts with offshore winds. Since all of our sampling missions were conducted during onshore winds, we speculate that a significant fraction of the observed airborne particles were from the lakes studied. We acknowledge, however, that some of the particles may have originated from other non-lake sources. Future experiments with multiple background sampling locations would help to elucidate potential contributions to airborne particle concentrations.

Sixty percent (15/25) of the impinger samples contained at least one biotic (fluorescent) object. We saw higher numbers on average from LE, which could be caused by lake chemistry or environmental conditions that favor aerosolization of biotic objects.(Pant et al., 2008; Montero et al., 2016) Since the biotic objects were often on the larger end of the range (3-10 μm), we speculate that they may have stronger associations with particle counts of those sizes. Unfortunately, due to the low number of particle counts in the larger size bins, we were unable to provide a constructive analysis of this potential association. Impinger samples were also analyzed for a suite of cyanotoxins using LC-

MS/MS, but no cyanotoxins were detected in any of the samples. Hanlon et al. (2022)(Hanlon et al., 2022) conducted a series of water sampling missions at GLSM and LE during the same calendar dates and reported high levels of microcystin in the water, 15.00 and 1.92 µg/L, respectively. HAB-associated toxins can be aerosolized and transported to inland communities where they threaten the health of humans.(Fleming et al., 2005a; Pierce et al., 2005; Cheng et al., 2007; Kirkpatrick et al., 2011; Plaas and Paerl, 2021) In addition, wave breaks and bubble-bursting cause water to spray and contributes to aerosol production and the dispersal of cells, especially in larger bodies of water such as LE,[8] and cyanotoxins into the air.(Pierce et al., 2005) Aerosols produced in this way have been found to contain MCs in samples collected over land near a HAB, showing that the toxin can be transported over land to the surrounding area.(May et al., 2018b) Sutherland et al.(Sutherland, 2021) detected anatoxin-a in air samples during a HAB at Capaum Pond on Nantucket Island, Massachusetts, USA in 2019. Though air samples have not yet been incorporated into routine HAB monitoring in freshwater environments, the spread of HAB-associated aerosols in marine environments (e.g., brevetoxin) is known to cause respiratory problems and can be dangerous to those with underlying health conditions.(Fleming et al., 2005a) The approach showcased here demonstrates the feasibility of a rapid drone-based system to extend monitoring protocols beyond the water's edge. And while we did not necessarily detect any appreciable toxin values in our samples, our data regarding the distribution of particles as well as impingement of numerous fluorescent objects does validate the approach.

The concerns regarding the accuracy of lightweight and inexpensive OPCs is an important limitation to consider when comparing values of one OPC to another or to

determine absolute high or low levels of particles.(Bulot et al., 2019; Giordano et al., 2021) Our field experiments relied on a single OPC as part of the AirDROPS package. However, as shown in the laboratory calibration experiments, the data recorded from this OPC were robust and consistent with simultaneous measurements recorded from the APS.

Additional work is needed to understand the environmental factors associated with the potential aerosolization and transport of cyanobacterial cells and toxins in aquatic environments. Higher windspeeds may decrease total particle counts above a lake, but also drive aerosol production closer to the lake surface.(Dueker et al., 2017; Hu et al., 2020a; Olson et al., 2020) Though our study was only focused on an altitude of 10 m above the water surface, it sets the stage for future work to examine the vertical distribution of HABs above a lake surface. Powers et al. (Powers et al., 2018) conducted simultaneous sampling missions of microorganisms with a UAS and a USV at Claytor Lake, Virginia, USA. It should be noted that although Claytor Lake had relatively high levels of the bacterium *Pseudomonas syringae*, it was not experiencing a HAB. Additional research is needed to understand threats, manage risks, mitigate incidents, develop capabilities, and strengthen collaborations for improved water quality and security.(Schmale et al., 2019) Aerial and aquatic robots can be fitted with the tools to be used to work alongside health professionals and air and water quality experts to provide critical and timely information to guide regulatory decisions. Modeling of particle counts as a function of the wind speed, wind direction, and temperature could allow for future predictions of areas impacted by HAB-associated aerosols.(Ross et al., 2022) Such information is critical for determining time-sensitive health advisories, and to create public health forecasting models for the communities of people that live near contaminated bodies of water.

2.6 Author contributions

DS conceived, planned, and conducted the field experiments. BB assisted DS with all field experiments and data and sample curation following each sampling mission. LB conducted calibration experiments in the laboratory and analyzed data from all of the experiments. JGR conducted sUAS missions for measurements of wind. RH organized flow cytometry analyses. JB and JW conducted cyanotoxin analyses. LB and DS led the writing of the manuscript. All authors provided feedback on the manuscript.

2.7 Conflicts of interest

There are no conflicts to declare.

2.8 Acknowledgements

This work was supported in part by the Institute for Critical Technology and Applied Science at Virginia Tech under grant number (ICTAS-178429).

Chapter 3. Monitoring wind and particle concentration near freshwater and marine harmful algal blooms (HABs)

Landon Bilyeu, Javier González-Rocha, Regina Hanlon, Nora Al Amiri, Hosein Foroutan, Shane D. Ross, and David G. Schmale III

Submitted: May 2024

To: Environmental Science: Advances

Status: In review

3.1 Abstract

Harmful algal blooms (HABs), caused mostly by toxic cyanobacteria, are a threat to aquatic ecosystems. New information is needed about the environmental conditions associated with the aerosolization and transport of HAB cells and their associated toxins. This information is critical to help inform our understanding of potential exposures. We used a ground-based sensor package to monitor weather, measure airborne particles, and collect air samples on the shore of a freshwater HAB (bloom of *Rhaphidiopsis*, Lake Anna, Virginia) and a marine HAB (bloom of *Karenia brevis*, Gulf Coast, Florida). Each sensor package contained a sonic anemometer, impinger, and optical particle counter. A drone was used to measure vertical profiles of windspeed and wind direction at the shore and above the freshwater HAB. At the Florida sites, airborne particle number concentrations (cm^{-3}) increased throughout the day and the wind direction (offshore versus onshore) was strongly associated with these number concentrations (cm^{-3}). Offshore wind sources had particle number concentrations (cm^{-3}) 3 to 4 times higher than those of onshore wind sources. A predictive model, trained on a random set of weather and particle number concentrations (cm^{-3}) collected over the same time period, was able to predict airborne particle number concentrations (cm^{-3}) with an R Squared value of 0.581 for the freshwater HAB in Virginia and an R Squared value of 0.804 for the marine HAB in Florida. The drone-based vertical profiles of the wind velocity showed differences in wind speed and direction at different altitudes, highlighting the need for wind measurements at multiple heights to capture environmental conditions driving the atmospheric transport of aerosolized HAB toxins. A surface flux equation was used to determine the rate of aerosol production at the beach sites based on the measured particle number concentrations (cm^{-3}) and weather conditions. Additional work is needed to better understand the short-term fate and transport of

aerosolized cyanobacterial cells and toxins and how this is influenced by local weather conditions.

3.2 Introduction

Freshwater and marine ecosystems are experiencing an increasing number of harmful algal blooms (HABs)(Backer et al., 2015). HABs often result from the proliferation of toxin-producing cyanobacteria that are harmful to humans and wildlife(Watson et al., 2015; Powers et al., 2018; Schmale et al., 2019; Hu et al., 2020a). HABs known as red tides may occur in marine environments, and aerosolized toxins from blooms of red tide are known to have harmful impacts on people(Pierce et al., 2003; Ross et al., 2022). HABs in lake systems often occur in areas with warmer water and high levels of phosphorus favorable to cyanobacterial growth (Anderson et al., 2002; Hoorman et al., 2008; Bertani et al., 2016). However, ocean HABs are increasingly common as well and may be on the rise due to human influence and ocean acidification(Smayda, 1997; Fu et al., 2012; Dees et al., 2017; Wells and Karlson, 2018). The increase in HAB occurrence is concerning from a human and animal health perspective and requires further study involving higher resolution observations to better pinpoint the factors driving increased occurrence of ocean and lake HABs(Fu et al., 2012; Backer et al., 2015; Wells et al., 2020).

Research is needed to better understand how to address and mitigate the impacts of the ever-increasing HAB threat to shorelines and downwind impact areas(Kirkpatrick et al., 2010; Olson et al., 2020). Generally, water samples are collected by hand from boats and processed at off-site laboratories(Maloney and Carnes, 1966). Recently, robots have presented new opportunities to sample HABs with minimal human exposure (Hanlon et al., 2022, Bilyeu et al., 2022). Such approaches can be used to inform health guidelines and policy around HAB occurrences to best keep exposure risks low(Carmichael and Boyer, 2016; Dueker et al., 2017; Hu et al., 2020a). The negative economic impact of HABs can

also be mitigated through the use of predictive models providing a benefit to the individuals of impacted communities(Moeltner et al., 2022).

Small uncrewed aircraft systems (sUASs or drones) have been used to monitor HABs and assess their potential impact on surrounding communities(González-Rocha et al., 2020, 2023; Bilyeu et al., 2022). Early applications of sUAS for HAB monitoring involved integrating cameras on board fixed- and rotary-wing sUAS for image data collection (Wu, 2019). More recently, sUAS techniques have been developed to sample both air and water affected by HABs. Hanlon et al. (2022) used a drone water sampling system to collect water samples from three lakes with HABs. Bilyeu et al. (2022) used an Airborne DROne Particle-monitoring System (AirDROPS) to monitor, collect, and characterize airborne particles over two HABs. Gonzalez-Rocha et al. (2023) extended a model-based (sensor free) wind estimation technique to measure atmospheric flows in aquatic environments(González-Rocha et al., 2019, 2020).

Though mechanisms of aerosolization in marine and freshwater environments have received considerable attention(Pierce et al., 2003), new information is needed to understand the environmental factors driving high counts of aerosolized HAB cells and toxins(Stumpf, 2001; Hoorman et al., 2008; Harb and Foroutan, 2019; Harb et al., 2021). We hypothesized that wind directions and speed impact airborne particle concentration differently in marine vs freshwater systems. To test this hypothesis, we conducted drone-based and ground-based sampling missions on the shore of a freshwater HAB (bloom of *Rhaphidiopsis*, Lake Anna, Virginia) and a marine HAB (bloom of *Karenia brevis*, Gulf

Coast, Florida). The specific objectives of our work were to: (1) monitor airborne particles on the shore of a freshwater HAB (bloom of *Rhaphidiopsis*, Lake Anna, Virginia) and a marine HAB (bloom of *Karenia brevis*, Gulf Coast, Florida), (2) observe and model potential associations of wind direction, wind speed, and temperature with airborne particle number concentrations (cm^{-3}), and (3) determine onshore and offshore wind profiles at the freshwater HAB site using a small drone platform.

3.3 Methods and Materials

3.3.1 Study Sites

Studies were conducted along the shore of a freshwater HAB at Lake Anna, Virginia, and a marine HAB along the Gulf Coast of Florida (**Figure 1**). Lake Anna is a reservoir lake in North-Central Virginia of 13,000 acres and is the third largest lake in the state(Lake Anna State Park: General information, 2023).

Figure 1. One sampling location at Lake Anna, VA marked in yellow, and the two beaches in Manasota, FL and Seagate FL in red are marked where sampling was performed. Lake Anna consisted of ground level and drone-based sampling while Manasota and Seagate beaches consisted of only ground level sensing.

Our first sampling site was near the inflow of Pamunkey Creek into Lake Anna (Site 1; 38.14132 N, 77.9276 W). The second sampling site on Lake Anna was on the end of a peninsula between the inflows of Gold Mine Creek and Hickory Creek (Site 2; 38.11544 N, 77.94146 W). Both locations are in the Northwest portion of the lake and were chosen

as a sample site due to recent HAB occurrences in the lake(Hanlon et al., 2022). Ground-based sensors were placed on the shoreline within 5-10 meters of the lake or ocean shore (**Table 1**).

Table 1. Shows the date, time, location, and lake/ocean designator for each sampling period.

		Ground Operations			
Date	**Start**	**End**	**Latitude**	**Longitude**	**Description**
12/3/2019	11:15	11:45	26.20848	-81.8169	Ocean
12/3/2019	12:00	12:30	26.20848	-81.8169	Ocean
12/3/2019	12:45	13:15	26.20848	-81.8169	Ocean
12/3/2019	13:30	14:00	26.20848	-81.8169	Ocean
12/3/2019	14:15	14:45	26.20848	-81.8169	Ocean
12/3/2019	15:00	15:30	26.20848	-81.8169	Ocean
12/4/2019	9:45	10:15	27.01129	-82.4135	Ocean
12/4/2019	10:30	11:00	27.01129	-82.4135	Ocean
12/4/2019	11:15	11:45	27.01129	-82.4135	Ocean
12/4/2019	12:00	12:30	27.01129	-82.4135	Ocean
12/4/2019	12:45	13:15	27.01129	-82.4135	Ocean
12/4/2019	13:30	14:00	27.01129	-82.4135	Ocean
30/6/2020	10:15	11:00	38.1416	-77.9274	Lake
30/6/2020	11:15	11:45	38.1416	-77.9274	Lake
7/7/2020	9:15	9:50	38.1413	-77.9276	Lake
7/7/2020	9:55	10:25	38.1413	-77.9276	Lake
7/7/2020	10:35	11:05	38.1413	-77.9276	Lake
7/7/2020	11:20	11:30	38.1413	-77.9276	Lake
7/7/2020	12:00	12:30	38.1413	-77.9276	Lake
7/7/2020	12:45	13:20	38.1413	-77.9276	Lake
7/7/2020	13:35	14:05	38.1413	-77.9276	Lake
7/8/2020	10:40	11:10	38.11543	-77.9415	Lake
7/8/2020	11:25	11:55	38.11543	-77.9415	Lake
7/8/2020	12:05	12:35	38.11543	-77.9415	Lake
7/8/2020	12:45	13:15	38.11543	-77.9415	Lake

Drone measurements were taken over land as well as over the water surface (**Table 2, Figure 2**).

Table 2. Shows the date, time, maximum altitude, location, and onshore or offshore designation of profile.

Drone Flight Operations						
Date	**Start**	**End**	**Height (m)**	**Latitude**	**Longitude**	**Description**
7/7/2020	9:21	9:23	80	38.141046	-77.928161	Offshore
7/7/2020	9:23	9:26	80	38.141177	-77.927314	Onshore
7/7/2020	9:58	10:00	80	38.141046	-77.928161	Offshore
7/7/2020	10:00	10:02	80	38.141177	-77.927314	Onshore
7/7/2020	10:35	10:37	80	38.141046	-77.928161	Offshore
7/7/2020	10:37	10:40	80	38.141177	-77.927314	Onshore
7/7/2020	10:55	10:58	80	38.141046	-77.928161	Offshore
7/7/2020	10:58	11:00	80	38.141177	-77.927314	Onshore
7/7/2020	11:21	11:24	80	38.141046	-77.928161	Offshore
7/7/2020	11:24	11:26	80	38.141177	-77.927314	Onshore
7/7/2020	11:42	11:44	80	38.141046	-77.928161	Offshore
7/7/2020	11:44	11:46	80	38.141177	-77.927314	Onshore
7/7/2020	`12:00	12:02	80	38.141046	-77.928161	Offshore
7/7/2020	12:02	12:05	80	38.141177	-77.927314	Onshore
7/7/2020	12:19	12:22	80	38.141046	-77.928161	Offshore
7/7/2020	12:22	12:24	80	38.141177	-77.927314	Onshore
7/7/2020	13:09	13:12	80	38.141046	-77.928161	Offshore
7/7/2020	13:12	13:15	80	38.141177	-77.927314	Onshore
7/7/2020	13:40	13:42	80	38.141046	-77.928161	Offshore
7/7/2020	13:42	13:44	80	38.141177	-77.927314	Onshore
7/7/2020	13:58	14:01	80	38.141046	-77.928161	Offshore
7/7/2020	14:01	14:03	80	38.141177	-77.927314	Onshore

Two ground-based devices were deployed simultaneously at Lake Anna, Virginia for multiple sampling periods (at least 30 minutes each). Two sampling periods were conducted on June 30th, 2020, seven sampling periods were conducted on July 7th, 2020, and four sampling periods were conducted on July 8th, 2020. Wind profiles were performed at Lake Anna following a 30-minute cadence, on average.

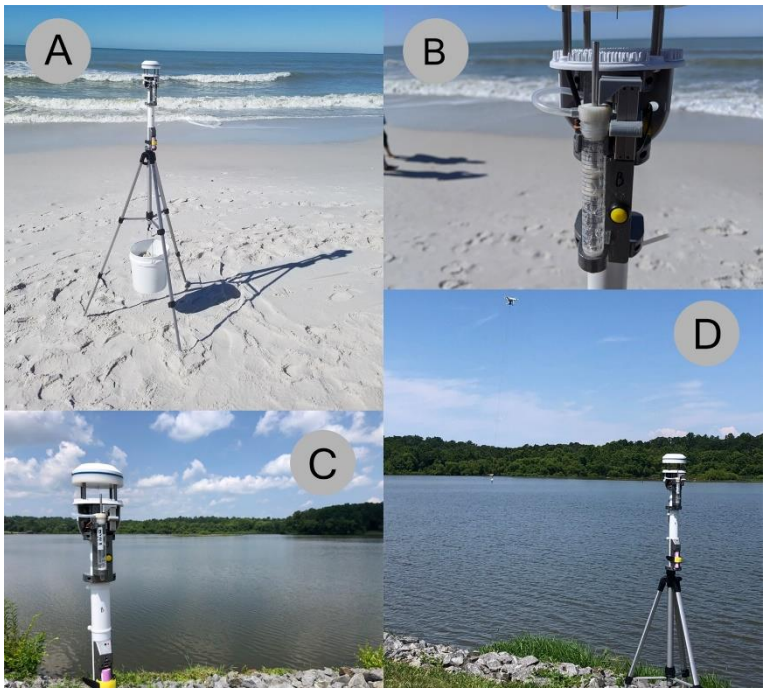

Figure 2. A shows the ground sampling device in location at Seagate Beach FL, December 3, 2019. B shows a closeup of the impinger actively sampling the air while the weather station is running in Florida. C shows the ground sampling device at Lake Anna, Virginia collecting near the lake shore on June 30, 2020. D shows combined drone and ground sampling at Lake Anna.

The Gulf of Mexico experiences intermittent HABs caused by *K. brevis* which makes the Florida Gulf coast a prime location for HAB aerosol sampling(Pierce et al., 2003). Ground-based sensor sampling was chosen for this location by using the Mote Beach Conditions

Reporting System and next-day forecasting from a data-driven model (Ross et al., 2022) to determine a beach with a high probability of HAB irritation(Mote Beach Conditions Reporting System, 2022). Seagate beach was chosen as a site, located at GPS coordinates 26.20848 N, 81.81687 W. To capture samples earlier in the morning, Manasota Beach was chosen for our second sample location. This site was located at GPS coordinates 27.01129 N, 82.41348 W. Two sampling devices were used simultaneously for 30-minute increments. Six sampling periods were performed on December 3rd and 4th, 2019 at Seagate and Manasota Beach, respectively. A total of 24 collected beach weather and particle count measurements were collected during this period.

Fourteen sampling periods were conducted along the Gulf of Mexico coast in Florida, and 11 were conducted at Lake Anna in Virginia (**Table 1**). Sampling periods consisted of ground sensors measuring weather and particle number concentrations (cm^{-3}) approximately 2 meters above ground level near to the shore at all sites (**Table 1**). Drone flights were performed during the Lake Anna sampling periods, both above the shore and above the water alternately, over a range of elevation from 10 to 80 meters to measure the wind speed and direction at different altitudes (**Table 2**).

3.3.2 Ground-based air particle and weather monitoring system

A sensor system integrating weather monitoring, impinger, and particle counting capabilities was utilized to take ground measurements 2 m above ground level. The weather data was collected with a meteorological (MET) sensor, an Atmos 22 sonic anemometer weather station atop the sensor measuring the weather conditions at 1 Hz. The

impinging device and the optical particle counter (OPC; Plantower PMS 7003) operated under the same system as described in Bilyeu et al.(Bilyeu et al., 2022) for the airborne drone particle-monitoring system. Particle number concentrations (cm^{-3}) were measured as the number of particles with diameter beyond 0.3 μm in 0.1 L of air. These numbers were then converted into particle number concentrations (cm^{-3}). The difference between the drone system and the ground-based system was only in operation, with the ground-based sensors being started and stopped manually and the run times for the sensors lasting for 30 minutes or more.

3.3.3 Drone-based wind velocity measurements

Vertical profiles of wind velocity were obtained from wind-induced perturbations to the steady motion of the quadrotor using the model-based wind estimation framework presented by Gonzalez-Rocha et al. (2019, 2020). This wind estimation framework employs linear time-invariant (LTI) models that characterize the vehicle's plunging, yawing, rolling, and pitching dynamics in hovering and steady-ascending flight. The models were characterized by employing an aircraft system identification algorithm developed by Morelli and Klein (2016). Aircraft system identification is a data-driven approach for determining the model structure and parameter estimates that describe the dynamics of an aircraft systems from measurements of pilot-induced excitation commands from equilibrium flight and the vehicle's dynamic response (i.e., position, attitude, translational velocity, and angular rates and control inputs). The LTI models corresponding to each equilibrium flight condition were then used to construct a wind-augmented model, which treats wind disturbances as unmeasured internal states. The wind-augmented model and measurements of position,

attitude, and respective time rates were used to estimate the wind using a state observer. The reliability of the wind velocity estimates obtained from the state observer has been validated in previous studies next to conventional *in-situ* and remote sensors (Gonzalez-Rocha et al., 2020,2023).

3.3.4 Data analyses

Data were saved to microSD cards as csv files and then processed to remove corrupted data in Microsoft Excel. Microsoft Excel was also used to determine trends between measured weather conditions and particle number concentrations (cm^{-3}) before statistical analysis. Potential associations between wind speed, wind direction, temperature and particle number concentrations (cm^{-3}) were examined. Statistical analyses were performed using JMP Pro Version 16 software (Cary, North Carolina, USA). A model was fit using the JMP neural network as described in Bilyeu et al. (2022) using data collected from one ground sensor from Lake Anna and another model was made using a ground sensor from Manasota Beach. The Lake Anna model was trained on 5126 measurements and verified on 2563 measurements, while the Manasota Beach model was trained on 3886 measurements and verified on 1944 measurements.

Using the methods described in Clarke et. al. (2006)(Clarke et al., 2006) we were able to calculate the surface flux for 100% bubble coverage, S_{100}, for the Florida beach testing sites. S_{100} is defined as the number of sea-salt aerosols generated per unit area of ocean surface completely covered by bubbles (100% coverage) per unit time. The equation to determine flux ($cm^{-2}\ s^{-1}$) was as follows:

$$S_{100} = [C_s\ k\ V_{wind}\ h) / (A_{avg}\ L + 0.5\ wo)] \quad (1)$$

Where C_s is the measured average particle number concentration for each 30-minute interval (cm^{-3}), k is the multiplier for tower C_s, set to 1.5, V_{wind} is the average wind speed for each 30-minute interval ($m\ s^{-1}$), h is the height of sampler, which was 200 cm, A_{avg} is the mean bubble fraction coverage, set at 0.5, L is the distance the wave travels to shore, set at 20 m, and wo was the initial width of the bubble front set at 2 m.

3.4 Results

3.4.1 Wind direction and wind speed

3.4.1.1 Lake Anna weather measurements

Onshore wind measurements from the drone showed an increase in wind speed at all altitudes as the sampling period progressed through the morning (**Figure 3**). However, higher altitudes had consistently lower wind speeds until 11:00 AM local time. The offshore winds showed a similar trend of increasing wind speed from the beginning of sampling until 11:00 AM. The offshore winds were different, however, due to higher wind speeds at higher altitudes and lower wind speeds at lower altitudes (**Figure 3**).

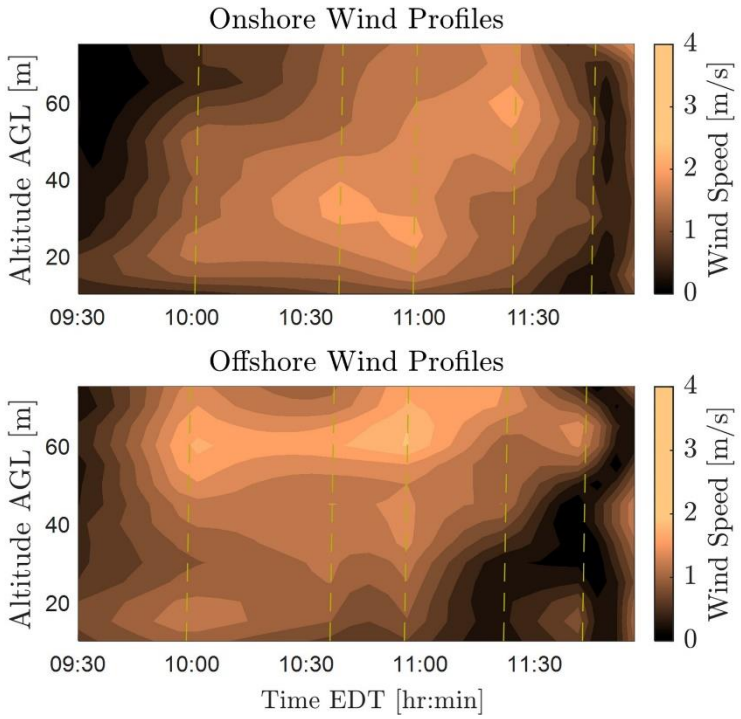

Figure 3. Onshore and offshore wind profiles showing wind speed as a factor of altitude for flights taken over Lake Anna over the course of the day on July 7th, broken down based on wind coming from over the land or over the water.

Comparing the ground sensors with the drone measurements on July 7th showed fairly consistent agreement between the two ground sensors and the drone measurements for wind source (**Figure 4**). This helps validate the measurements taken by the drone while showing that the ground sensor is not capturing the whole picture with regards to the weather effects experienced by HAB particles after emission from lake and ocean sources.

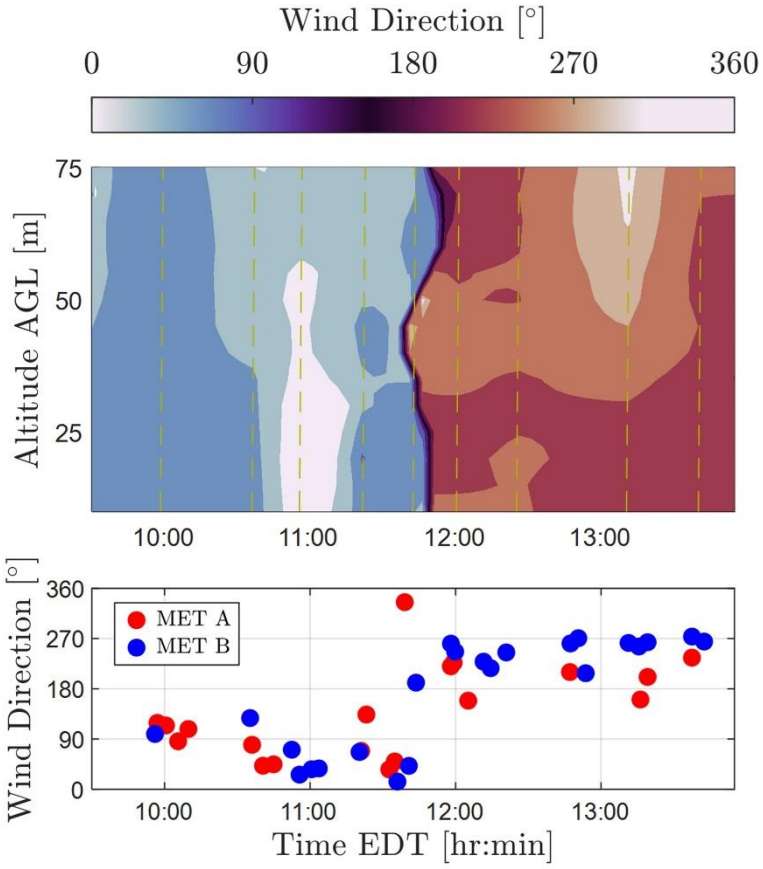

Figure 4. Wind direction at different altitudes over the course of the sampling day on July 7th, and the ground sensor measured wind directions of the corresponding times.

Wind direction measurements at Lake Anna Site 1 indicated sources from all directions, whereas at Site 2, the wind consistently originated from the East throughout the entire sampling period (**Figure 5**).

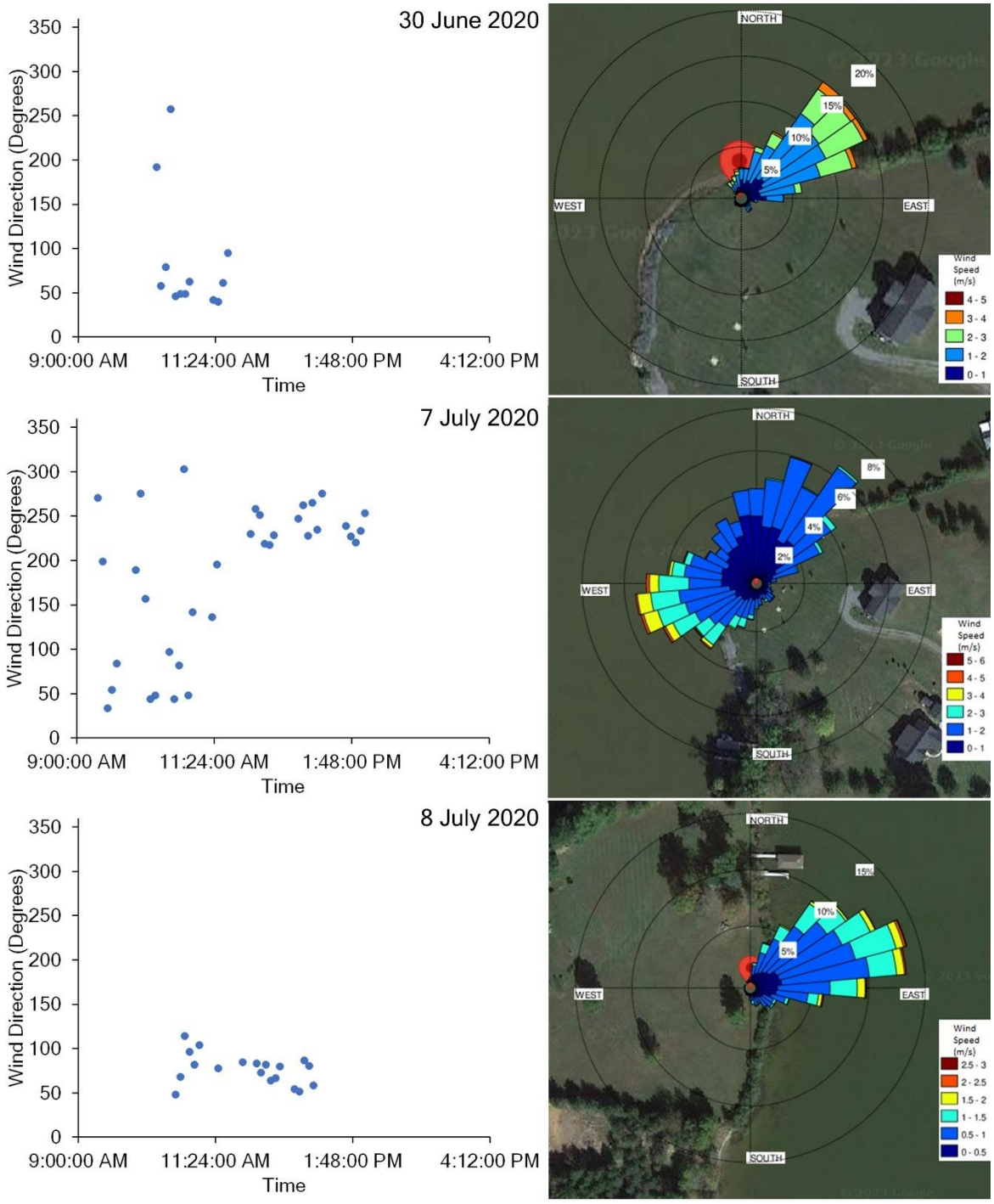

Figure 5. Wind direction source measured over the course of the sampling day, plotted as five-minute averages. The first two graphs show the 30th of June and 7th of July sampling beach along with the sampler location. The third graph shows the second beach site where measurements were made on the 8th of July. To the right of each graph is the sensor location with the wind rose for the day overlaid.

3.4.1.2 Florida ground-based weather measurements

The wind source direction measured at Seagate Beach and Manasota Beach in Florida mostly came from the North during our sampling period. Easterly morning winds shifted to Northwest winds later in the day (**Figure 6**). This trend is more clearly visible at Manasota Beach where sampling was started earlier in the day.

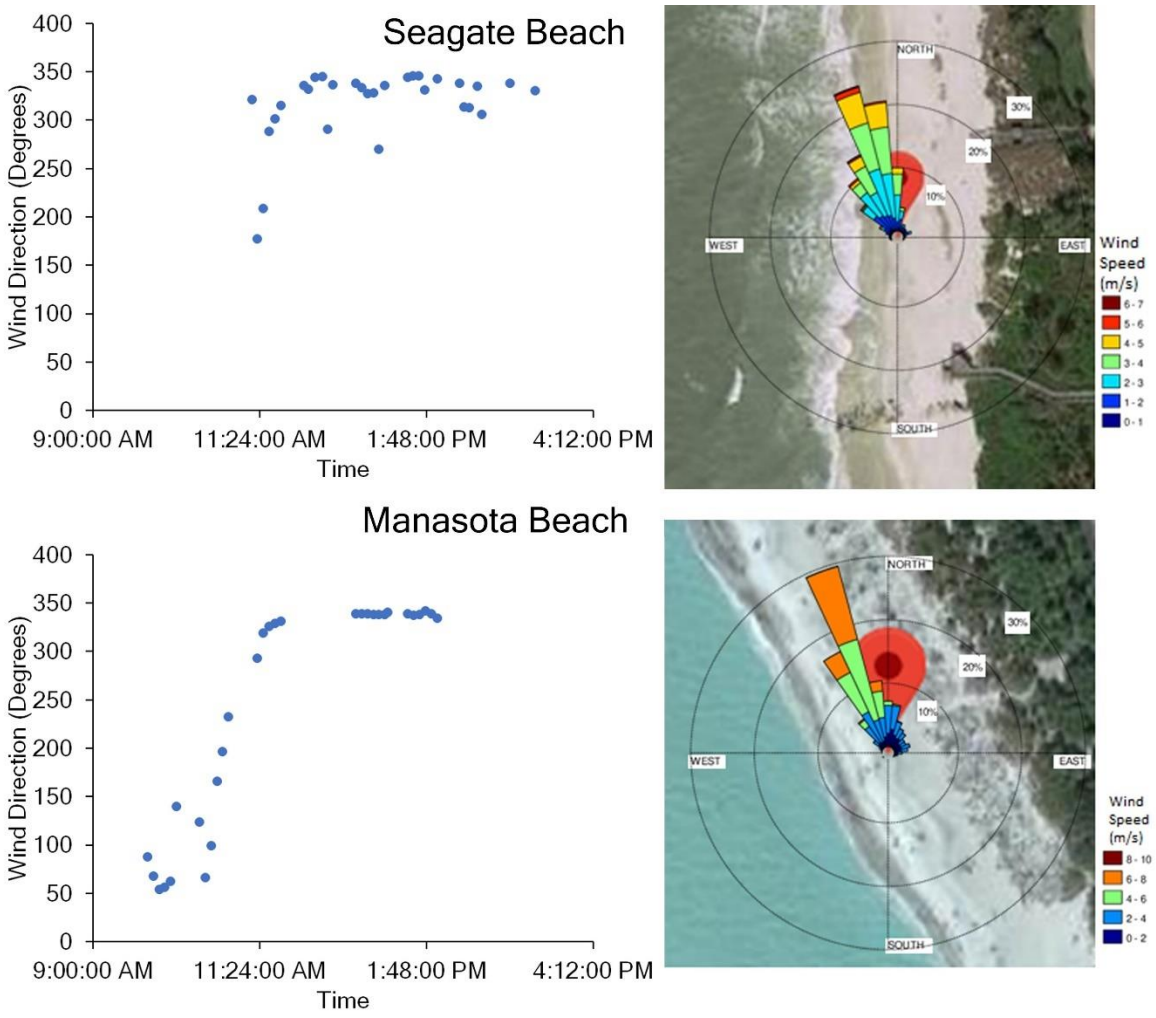

Figure 6. The graphs show wind direction source measured over time at two different Florida beaches in December 2019 plotted as five-minute averages. The top graph shows measurements taken at Seagate beach on December 3rd while the bottom graph shows measurements taken at Manasota beach on December 4th. To the right of each graph is the sensor location with the wind rose for the day overlaid.

3.4.2 Particle number concentrations

3.4.2.1 Lake Anna ground-based airborne particle concentrations

Airborne particle concentrations (cm^{-3}) at Lake Anna varied over the time of day we sampled as well as varying over the different sampling days with Site 1 showing a decrease in particle number concentrations (cm^{-3}) over the course of the sampling periods and Site 2 showing an increase in the particle number concentrations (cm^{-3}) over the course of the sampling periods (**Figure 7**).

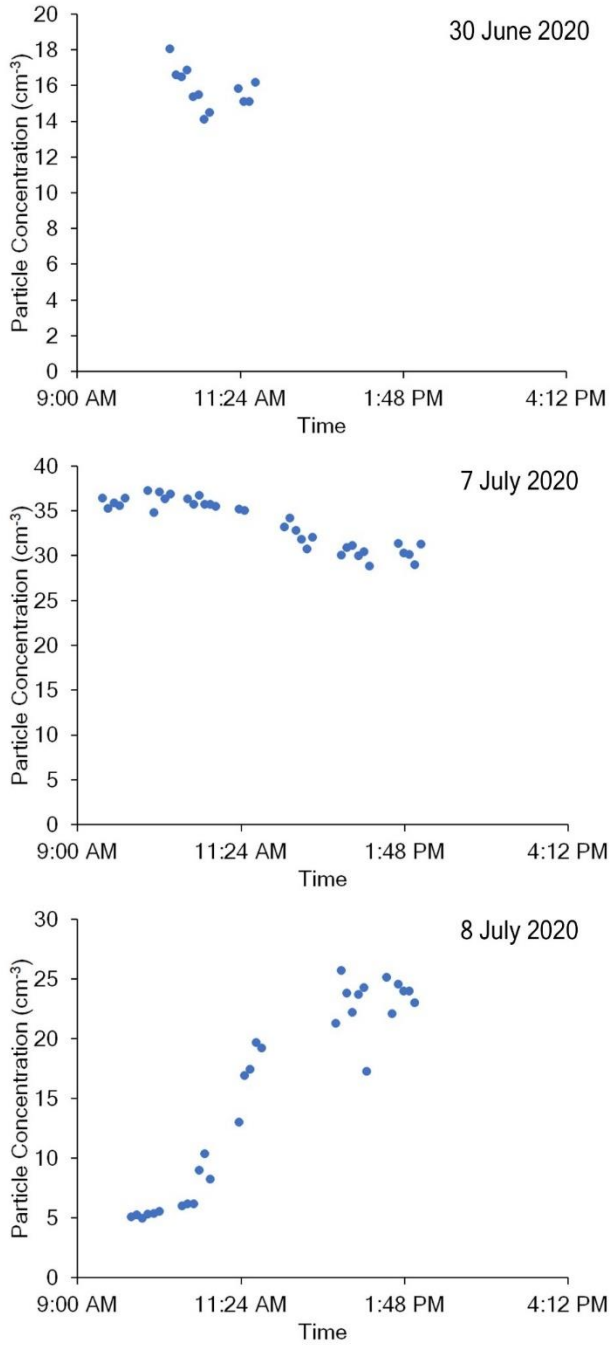

Figure 7. Particle number concentrations (cm^{-3}) greater than 0.3 microns in diameter measured over the course of the day, plotted here as five-minute averages. The first two graphs represent June 30th and July 7th at the first Lake Anna beach site and the third graph represents July 8th at the second Lake Anna beach site.

The particle concentrations at Site 1 appeared to be higher on average than those observed at Site 2, ranging from 15-20 cm^{-3} measured on June 30th and from 25-45 cm^{-3} on July 7th, while Site 2 had a much lower concentration of particles ranging from 4.5-14 cm^{-3}. Particle concentrations also showed some correlation with wind source, having lower concentrations for wind sources over land in the July 7th measurements, with wind direction being statistically significant for predicting particle concentration (**Figure 8**).

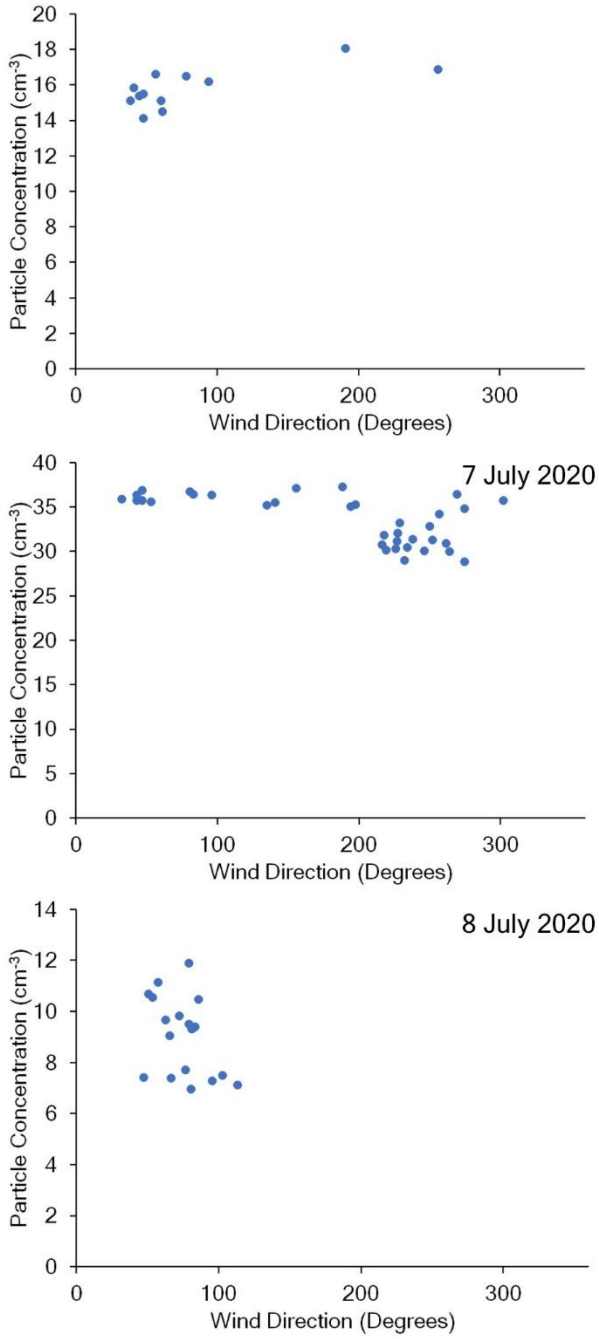

Figure 8. Particle number concentrations (cm^{-3}) greater than 0.3 microns in diameter measured wind direction as five-minute averages during the sampling periods at Lake Anna beach sites one and two. The first two graphs depict beach site one during the sampling period of June 30th and July 7th. The third graph shows the data collected from beach site two on July 8th.

3.4.2.2 Florida ground-based airborne particle concentration

Particle number concentrations (cm^{-3}) at Seagate Beach did not appear to change much over the entire sampling day; however, particle number concentrations (cm^{-3}) measured at Manasota Beach had a noticeable increase starting during the second sampling period (**Figure 9**). Both beaches measured particle number concentrations (cm^{-3}) below 5 and highs of above 30 at Seagate Beach and above 45 at Manasota Beach (**Figure 9**). However, while the average particle number concentrations (cm^{-3}) at Seagate beach remained low throughout the sampling period, we saw an increase in the particle number concentrations (cm^{-3}) at Manasota Beach that started in our second sampling period and continued throughout the day.

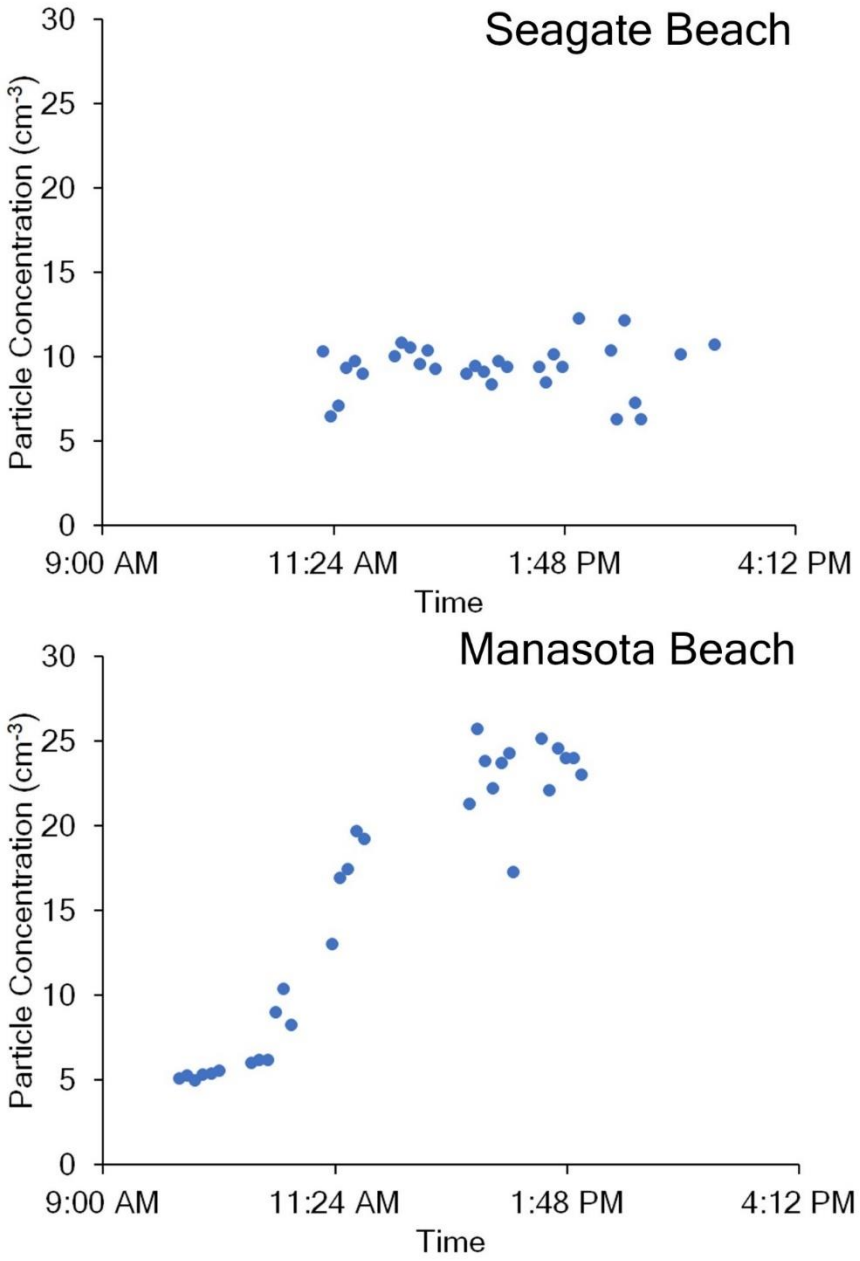

Figure 9. The graphs show particle number concentrations (cm^{-3}) greater than 0.3 microns in diameter measured over time at two different beaches in Florida on two days in December 2019 plotted as five-minute averages. The top graph shows Seagate beach on December 3rd and the bottom graph shows Manasota beach on December 4th.

3.4.3 Prediction modeling of particle concentrations due to weather effects

Ground sensor particle number concentrations (cm^{-3}) of particles greater than 0.3 µm in diameter were matched with the corresponding weather data collected during the same interval. A prediction equation was developed using the wind speed, wind direction, and temperature data from the collected ground sensor data at Lake Anna on July 7th, 2020, and from Manasota Beach on December 4th, 2019, and predicted particle concentrations were compared against the actual measured concentrations (**Figure 10, Figure 11**). The Lake Anna empirical prediction equation produced a model that had an R-Squared of 0.577 and a validation prediction R-Squared value of 0.582. The hidden node equations and prediction equation, are as follows:

$$H_1 = \tanh[0.500 * (–48.213\ 1.354\ WS – 0.014\ WD + 1.621\ T)] \quad (2)$$

$$H_2 = \tanh[0.500\ (26.013 + 0.275\ WS – 0.010WD – 0.789T)] \quad (3)$$

$$H_3 = \tanh[0.500\ (–2.950 + 0.032WS + 0.0007WD + 0.153T)] \quad (4)$$

$$Theta = 76.183 - 316.902H_1 + 640.188H_2 + 4521.478H_3 \quad (5)$$

Where H_1, H_2, and H_3 are the hidden node equations and Theta is the prediction equation giving particle count in number of particles per 0.1 liter as the output. WS is the measured wind speed, WD is the measured wind direction and T is the temperature. The output of the Theta equation is then divided by 100 to get particle count per cubic centimeter.

The Manasota Beach empirical prediction equation produced a model that had a R-Squared of 0.804 and a validation prediction R Square of 0.802. The hidden node equations and prediction equation are as follows:

$$H_1 = \tanh[0.500\ (–8.722 – 0.138\ WS + 0.024WD + 0.104T)] \quad (6)$$

$$H_2 = \tanh[0.500\ (38.925 - 1.193WS - 0.005WD - 1.693T)] \quad (7)$$

$$H_3 = \tanh[0.500\ (9.500 + 0.154WS - 0.026WD - 0.120T)] \quad (8)$$

$$\text{Theta} = -765.521 - 45377.467H_1 - 682.357H_2 - 43301.880H_3 \quad (9)$$

Where H_1, H_2, and H_3 are the hidden node equations and Theta is the prediction equation giving particle count in number of particles per 0.1 liter as the output. WS is the measured wind speed, WD is the measured wind direction and T is the temperature. The output of the Theta equation is then divided by 100 to get particle count per cubic centimeter.

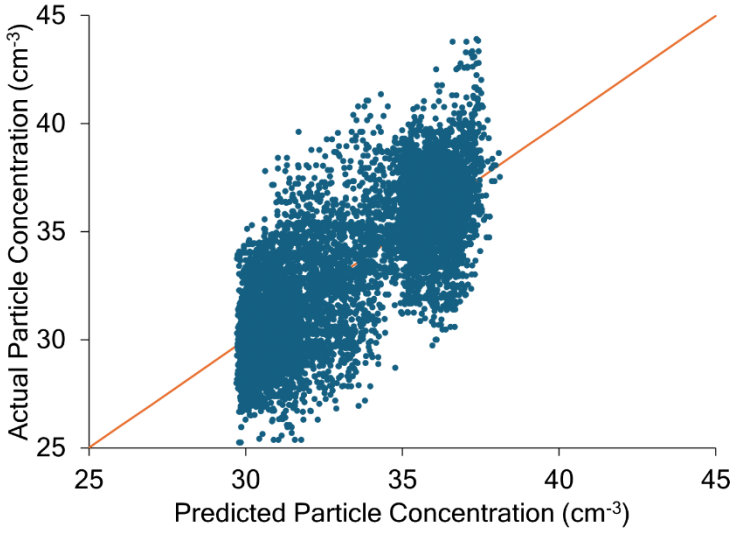

Figure 10. Measured vs. predicted particle number concentrations (cm^{-3}) of air used in the best fit model for Lake Anna collected data. The model was made using wind speed, wind direction, temperature, and particle count data collected by the ground sensors at Lake Anna. The data was then put into JMP Pro neural network modeling where a model equation was trained on a random subset of the data with another subset held back for validation.

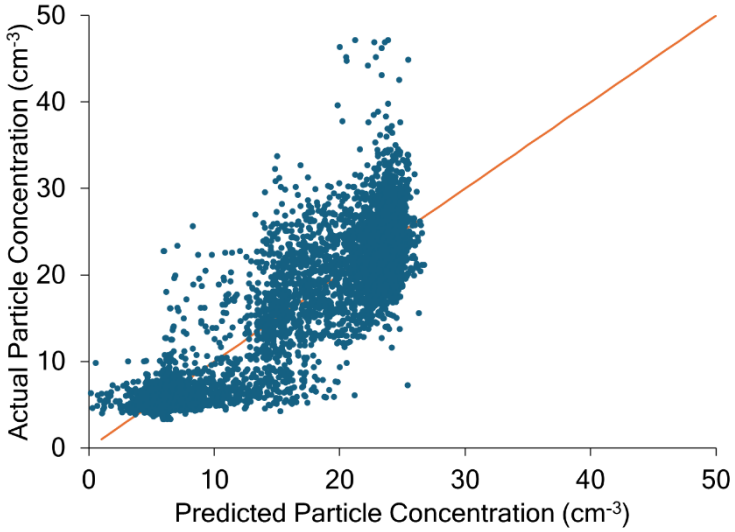

Figure 11. Measured vs. predicted particle number concentrations (cm^{-3}) used in the best fit model for Manasota beach collected data. The model was made using wind speed, wind direction, temperature, and particle count data collected by the ground sensors at Manasota beach. The data was then put into JMP Pro neural network modeling where a model equation was trained on a random subset of the data with another subset held back for validation.

3.4.4 Surface flux calculated for beach sites

By using the values collected by the OPC and attached weather sensor we were able to determine the C_s and V_{wind} for 30-minute intervals at each beach site. Intervals were divided into onshore or offshore wind sources. The S_{100} was calculated for each 30-minute interval and the flux from the onshore source wind was subtracted from offshore source wind. On Seagate beach the calculated flux ranged from 522 to 878 cm^{-2} s^{-1} with an average flux of 645 cm^{-2} s^{-1}. On Manasota beach the calculated flux ranged from 940 to 3549 cm^{-2} s^{-1} with an average flux of 2692 cm^{-2} s^{-1}.

3.5 Discussion

Freshwater and marine HABs behave in different ways and produce aerosols under different weather conditions(May et al., 2016, 2018a; Li et al., 2021). Bubble bursting and wave breaking phenomena contribute to the release of HAB aerosols in lake and ocean systems(Deane and Stokes, 2002; Olson et al., 2020). We used a combination of ground and drone-based sensing to measure wind speed, wind direction, temperature, and airborne particle number concentrations (cm^{-3}) on the shores of active HABs in Florida and Virginia. Our study provides new information on environmental conditions associated with increased particle number concentrations (cm^{-3}) at active HAB sites and could contribute to measurements of potential human exposure to HAB toxins(Pierce et al., 2003, 2005; Carmichael and Boyer, 2016; Hu et al., 2020a).

The particle number concentrations (cm^{-3}) measured by a Plantower PMS 7003 OPC were used for comparison only against their own measurements in this study. Previous work with inexpensive OPCs and with the Plantower brand have shown the total particle number concentrations (cm^{-3}) increased and decreased in tandem with more expensive and more reliable sensors while the bin sizes were less accurate(Levy Zamora et al., 2019; Hagan and Kroll, 2020; He et al., 2020). Our results showed the same inconsistency for the sensor's ability to correctly size particles, so we have chosen to only look at total measured particle number concentrations (cm^{-3}) greater than 0.3 μm diameter. Overall, less expensive OPCs seem to be reliable for measurements showing change in total particle number concentrations (cm^{-3})(Sang-Nourpour and Olfert, 2019; Crilley et al., 2020; He et al., 2020). By using the measured total particle number concentrations (cm^{-3}), which we match with our recorded weather conditions of wind speed, wind direction, and temperature, we

are able to measure how weather affects total particle count. In a previous study it was shown that higher particle number concentrations (cm^{-3}) are likely associated with HAB aerosol(Bilyeu et al., 2022; Hanlon et al., 2022).

At the Lake Anna sites, airborne particle number concentrations (cm^{-3}) decreased over the sampling day at Site 1 and increased over the sampling day at Site 2. When testing the parameters of the prediction model, the measured wind speed was most strongly associated with higher particle number concentrations (cm^{-3}) measured on the shore. Previous studies have shown airborne particle concentrations are influenced by windspeed on a lake surface, while shore based measurements have shown decreases in particle number concentrations (cm^{-3}) associated with higher wind speeds(Dueker et al., 2017; Powers et al., 2018). Studies have shown lake HAB aerosols can contain toxins that may be transported large distances beyond the shore(May et al., 2018b; Sutherland, 2021). We have previously shown that particle number concentrations (cm^{-3}) are significantly influenced by weather effects over the water in lake systems through similar particle and weather monitoring(Bilyeu et al., 2022). At the Florida sites, airborne particle number concentrations (cm^{-3}) increased throughout the day and the wind direction (offshore versus onshore) was strongly associated with these number concentrations (cm^{-3}). Offshore wind sources had particle number concentrations (cm^{-3}) 3 to 4 times higher than those of onshore wind sources. When developing the prediction equation for the Florida sites, the wind direction had the greatest influence on particle number concentrations (cm-3) (P <0.001), followed by temperature (P <0.001), and windspeed (P <0.001). This is consistent with previous studies done on ocean shores measuring aerosols produced by wave breaking

phenomena and their potential to expose the beach to toxins(Pierce et al., 2005; Kirkpatrick et al., 2011; Ross et al., 2022). Our approach of measuring particle levels at the shore using cheap particle counters shows a potential low-cost method for monitoring HAB associated aerosols on beaches.

A predictive model, trained on a random set of weather and particle count measurements collected over the same time period, was able to predict airborne particle number concentrations (cm^{-3}) with an R Squared value of 0.581 for the freshwater HAB in Virginia and an R Squared value of 0.804 for the marine HAB in Florida. Previous methods to monitor HAB severity and inform the public have relied on slow water and aerosol testing or more subjective measurements of respiratory irritation levels(Kirkpatrick et al., 2011; Mote Beach Conditions Reporting System, 2022). We were able to create a prediction equation for a beach and lake site, the conditions that lead to higher levels of particle number concentrations (cm^{-3}) in the prediction equations were different in the lake and ocean system and were different between lakes when compared to a previous study(Bilyeu et al., 2022). For example, the influence of wind speed on the level of particles could be more important for the lake system we measured due to the differences in how aerosols are produced in lake and ocean systems(Dueker et al., 2017; Hu et al., 2020a; Olson et al., 2020). In both ocean and lake systems we were able to predict higher or lower levels of HAB aerosols due to the influence of measured weather conditions. Using this method, any ocean or lake experiencing a HAB could be monitored and set up with a model to predict HAB severity.

Surface flux provides an emission rate for aerosol production at the water surface(Meskhidze et al., 2013). Using known conditions about wave structure, wind speed, and particle number concentrations (cm^{-3}) on shore, the surface flux can be calculated. We were able to calculate the surface flux for the beach sites during our sample period using the equation from Clarke et. al(Clarke et al., 2006). This analysis can be performed with ocean occurring HAB sites but there is currently no similar method for lake systems, as the method of aerosolization is different and less well studied(Slade et al., 2010; May et al., 2016, 2018a). While our current results show that the better understood ocean aerosol system allows for more robust analysis through surface flux calculations, with more research into lake aerosols we will have better prediction equations available.

The drone-based vertical profiles of the wind velocity showed differences in wind speed and direction at different altitudes, highlighting the need for wind measurements at multiple heights to capture environmental conditions driving the atmospheric transport of aerosolized HAB toxins. The comparison of onshore and offshore wind speed profiles shows the wind speed to be higher over the water. The higher wind speed conditions observed over water are likely due to the lower roughness length of the lake surface(May et al., 2016, 2018b). As shown in **Figure 6**, the vertical wind speed gradient was also observed to be larger over the lake. The higher wind speed gradient measured over the lake is likely the result of lower surface temperatures. Lower surface temperatures produce less air mixing in the lower atmosphere, resulting in higher wind gradients due to wind shear(Dueker et al., 2017; Medina-Pérez et al., 2021). Furthermore, the comparison of sUAS and ground sensor wind

measurements shows that sUAS technology can provide reliable observations of wind velocity(González-Rocha et al., 2019, 2023).

Higher resolutions of wind velocity observations such as those collected by drone-based measuring platforms are critical for predicting the transport of toxins produced by HABs. Additional work is needed to better understand the short-term fate and transport of aerosolized cyanobacterial cells and toxins and how the local weather conditions influence their transport. Risks at the shoreline may not accurately measure the risk of long-range transport that could be driven by higher altitude winds(Prijith et al., 2012). Lake aerosols are known to travel long distances and therefore better understanding their downwind fate is important to informing public health surrounding HABs(May et al., 2016; Olson et al., 2020). While our current methods of analysis for lake systems are not as accurate as ocean systems, lakes still play an important part in HAB aerosol production and distribution which requires further study(May et al., 2016; Harb and Foroutan, 2022). This study was focused on the measurements of particles at the shore but combined the wind measurements of different altitudes to give insight into a more unexplored area of HAB aerosol transport. In future studies, combining drone particle count measurements with air and ground wind measurements could help determine not only the near-shore impact of HAB toxins, but also predict their long-term fate. Using this data along with predictive models could then allow for broadcasting air quality as it relates to HABs to inform public safety and use of areas, lake, or ocean, impacted by HABs.

3.6 Author contributions

LB and RH conducted field experiments for the Florida sites. RH and JGR conducted field experiments for the Lake Anna sites. SR assisted in field experiment site selection in Florida. SR and HF assisted in field experiments in Florida. LB analyzed all ground sensor data from all experiments. JGR analyzed all data from drone measurements. NA and HF implemented the surface flux equation. DS planned experiments at Florida and Lake Anna sites along with LB, RH, and JGR. LB and DS led the writing of the manuscript. All authors provided feedback on the manuscript.

3.7 Conflicts of interest

There are no conflicts of interest to declare.

3.8 Acknowledgements

This work was supported in part by grants to DS from the U.S. National Science Foundation (NRI- 2001119) and the Institute for Critical Technology and Applied Science at Virginia Tech (ICTAS-178429). This work was also supported by a grant to HF, SR, and DS from the Global Change Center and the Institute for Society, Culture, and the Environment at Virginia Tech.

Chapter 4. Beach-level 24-hour forecasts of Florida red tide-induced respiratory irritation

Shane D. Ross, Jeremie Fish, Klaus Moeltner, Erik M. Bollt, Landon Bilyeu, Tracy Fanara

Submitted: September 2021

To: Harmful Algae

Status: Accepted January 2022

4.1 Abstract

An accurate forecast of the red tide respiratory irritation level would improve the lives of many people living in areas affected by algal blooms. Using a decades-long database of daily beach conditions, two conceptually different models to forecast the respiratory irritation risk level one day ahead of time are trained. One model is wind-based, using the current days' respiratory level and the predicted wind direction of the following day. The other model is a probabilistic self-exciting Hawkes process model. Both models are trained on beaches in Florida during 2011-2017 and applied to the red tide bloom during 2018-2019. For beaches where there is enough historical data to develop a model, the model which performs best depends on the beach. The wind-based model is the most accurate at half the beaches, correctly predicting the respiratory risk level on average about 84% of the time. The Hawkes model is the most accurate (81% accuracy) at nearly all of the remaining beaches.

Keywords: Red tide, Forecast, Respiratory irritation, Modeling, Hawkes process, Aerosol, HAB, Cyanobacteria, New tools, Public health

4.2 Author contributions

4.2.1 Bilyeu contributions

The paper entitled "Beach-level 24-hour forecasts of Florida red tide-induced respiratory irritation" was significantly influenced by the work of L. Bilyeu. This manuscript shows the development of two models to predict the level of respiratory irritation risk for the next day. The first model, utilizing current day respiratory irritation level and next day wind direction forecast, was in large part developed by the work of L. Bilyeu. The analysis of the data set to determine which factors were correlated with the respiratory irritation was performed by L. Bilyeu. L. Bilyeu and S. Ross worked together to analyze the data set and target specific beaches and times for the most useful periods to build a model from, as per figure 1 and figure 2. L. Bilyeu came up with the next day respiration predictions utilizing wind direction shown in section 2.1 which lead to the definition of onshore and off shore wind shown in figure 4 as well as the results shown in figure 5 and figure 6.

4.3 Introduction

Harmful algal blooms of the toxic dinoflagellate *Karenia brevis*, referred to as "Florida red tide" (henceforth abbreviated as RT) have affected the Florida Gulf coast for centuries. There is emerging evidence that these blooms have increased in frequency, intensity, and geographic spread in recent years (e.g., (Alcock, 2007; Nierenberg et al., 2009, 2010a, 2010b; Fleming et al., 2011; A primer on Gulf of Mexico harmful algal blooms by Mote Marine Laboratory and Aquarium - Issuu, 2014)). *K. brevis* produces brevetoxin, a neurotoxin that can result in massive fish kills and mortalities to marine mammals and sea birds. Indirectly, this can lead to neurotoxic shellfish

poisoning in humans from consuming contaminated shellfish (Kirkpatrick et al., 2006; A primer on Gulf of Mexico harmful algal blooms by Mote Marine Laboratory and Aquarium - Issuu, 2014).

More directly, and of primary interest for this study, brevetoxin is released into near-shore aerosol as RT cells are lysed by wave action, or aerosolized though bubble-mediated (Pietsch et al., 2018) transport. If inhaled by humans, brevetoxin can produce upper and lower respiratory irritation, such as a burning sensation of eyes and nose, and a dry, choking cough. While these symptoms have been found to be relatively short-lived in healthy individuals (upon separation from the harmful aerosol), RT effects can be more severe and longer-lasting for people with chronic respiratory conditions, such as asthma (Backer et al., 2003; Alcock, 2007; Fleming et al., 2009, 2011; Nierenberg et al., 2010b; Kirkpatrick et al., 2011; A primer on Gulf of Mexico harmful algal blooms by Mote Marine Laboratory and Aquarium - Issuu, 2014).

In this study, the potential of forecasting beach-specific respiratory irritation one day ahead of time is assessed, using previous irritation reports at the same location. Two models are proposed: one based on the current respiratory irritation level and a forecast of the next day's wind direction, and the other based on RT as a self-exciting process (or Hawkes process). Both are data-driven, trained on data on from 2011-2017, and tested on data from a severe RT bloom during 2018-2019. Both are compared with a simple persistence model, which assumes the next day's respiratory irritation level will be the same as the current day's.

4.3.1 Monitoring of red tide blooms

Monitoring for *K. brevis* blooms involves the following primary components. Satellite imagery is processed to locate potential blooms. Processed images are made available to managers and state health officials in the Gulf of Mexico through the National Oceanic and

Atmospheric Administration (NOAA) Harmful Algal Bloom Operational Forecast System (HAB-OFS) (National Oceanic and Atmospheric Administration, Harmful Algal Bloom Operational Forecast System, 2021). In Florida, where blooms tend to occur most frequently, water samples are collected weekly along the shore and from offshore transects by the Florida Fish and Wildlife Research Institute once a bloom is identified. Samples are delivered to a laboratory for cell enumeration via microscopy. Microscopic enumeration takes about one hour per sample (Hardison et al., 2019). Typically, samples are processed within 1–2 days and can take longer for more samples from remote areas. The resulting cell counts are then used by HAB-OFS to provide broad, county-wide forecasts of brevetoxin exposure risks. The cell count data for a particular county can be up to a week old by the time it is available to the public. In terms of forecast accuracy, Stumpf et al. (Stumpf et al., 2009) found that while county-wide forecasts of respiratory risk were correct 70% of the time, they were only correct 20% of the time when applied to individual beaches.

Recently, beach-level 24-hour forecasts for respiratory impacts have received the most focus from policy agencies (Moeltner et al., 2022). The Gulf of Mexico Coastal Ocean Observing System (GCOOS) recently developed a beach-level risk forecast that includes more than 20 Gulf Coast beaches (HAB Forecasts, n.d.). The forecast uses current wind forecasts as well as near real-time cell counts of *K. brevis* from water samples enabled by HABscope, a portable microscope system (Hardison et al., 2019). While the beach reporting system described below provides different data (actual beach-level respiratory impact, collected daily over several years), one can envision the potential to tie in to existing forecast frameworks, fusing the multiple data sources for more accurate forecasts or greater spatial coverage.

4.3.2 Beach Conditions Reporting System

To address the need for location-specific conditions, a Beach Conditions Reporting System (BCRS) was initiated in 2006 (Kirkpatrick et al., 2008; Currier et al., 2009; Stumpf et al., 2009; Nierenberg et al., 2011) and was redeveloped in 2015 when it began gaining public usership (Mote Beach Conditions Reporting System, 2022). From 2017-2019, the site gained approximately 1.5 million users. The BCRS provided smartphones to (professional) lifeguards and park rangers with an app designed for reporting beach conditions. Twice each day (10:00 and 15:00 local time), lifeguards and park rangers report occurrence of coughing as described further below (and other conditions such as presence of dead fish). While lacking the quantification and precision of microscopy, the reports provide beachgoers with useful real-time information for adequate planning (i.e., severity of aerosolized toxins, potential risks to asthmatics, presence of dead fish, etc.).

The BCRS is managed by Mote Marine Laboratory with lifeguards and park rangers as the primary reporters in several counties (Mote Beach Conditions Reporting System, 2022). The BCRS data compilation is automated, with timely sharing of data with agencies, including Florida Fish and Wildlife Conservation Commission and NOAA.

Though the BCRS provides more timely information about beach conditions than the weekly sampling described earlier, it does not provide key information needed for consistent forecasts. It provides no direct information on *K. brevis* cell presence, but rather an indirect assessment of *K. brevis* cell presence via water color and the presence of dead fish.

While RT outbreaks can occur throughout the entire year, aerosolized RT impacts have shown substantial variability both in a temporal and spatial sense. They can last from a few hours

to multiple days or even weeks at a given site (e.g., beach), and vary in intensity across sites at a given point in time, with heavily impacted areas at times alternating with completely unaffected shoreline segments (Nierenberg et al., 2009).

While efforts are ongoing to curb RT blooms via prevention and control methods (Alcock, 2007; Vargo et al., 2008; Nierenberg et al., 2010a; Kirkpatrick et al., 2014), the predominant management strategy to date has been mitigation, via early detection and avoidance of human contact (Alcock, 2007; A primer on Gulf of Mexico harmful algal blooms by Mote Marine Laboratory and Aquarium - Issuu, 2014).

4.4 Methods

Below, the RT respiratory irritation data set is described. Afterward, two different models to predict RT irritation risk one day ahead of time are described: a wind-based model and a Hawkes process model.

4.4.1 Respiratory irritation data

Starting in August 2006, the professional lifeguard corps in Sarasota County began twice-daily reports (approx. 10:00 and 15:00 local time) of the presence of respiratory irritation at six sites, as part of the BCRS. In January 2007, two additional lifeguard sites were added in Manatee County. Respiratory irritation is defined by the amount of coughing observed in addition to the personal conditions experienced by the lifeguard. The presence of people coughing is used as a proxy for respiratory irritation (cough, nasal congestion, throat irritation, chest tightness, wheezing, and shortness of breath). Coughing has been documented as a response to *K. brevis* aerosols in studies involving occupationally exposed workers,

recreationally exposed beachgoers, and asthmatics (Backer et al., 2003, 2005; Fleming et al., 2005b, 2007).

Lifeguards 'listen' to beachgoers for the presence and/or frequency of coughing. The symptoms observed by the lifeguards are reported at various levels of respiratory irritation as shown in Table 1. Irritation levels are given

Irritation level	**Risk level**	**In a 30 s audio sample**
None	Low	No coughing/sneezing heard in 30 s
Slight	Low	A few coughs/sneezes heard in 30 s
Moderate	High	A cough/sneeze heard every 5 s
High	High	Coughing/sneezing almost continuously

Table 1: The four-tiered red tide respiratory irritation levels reported in the Beach Condi- tions Reporting System, and the corresponding two-tiered risk level defined for this study.

on a four-tiered scale from 'None' (no coughing noted nearby), 'Slight' (a few coughs and sneezes within 30 seconds), 'Moderate' (A cough/sneeze heard every 5 seconds), and 'High' (continuous coughing and sneezing in nearby surroundings). For portions of the analysis below, moderate and high classes are together as 'high' risk, as these were the level at which impacts affect the general public (Stumpf et al., 2009). The 'none' and 'slight' are grouped as 'low' risk. The two-tiered (binary) classification of RT respiratory irritation risk was used in this study for an initial analysis of forecasting methods, based on historical data.

4.4.2 Statistics describing the data set

Since December 2011, the BCRS has monitored RT conditions at over 40 beaches in nine counties along the Gulf coast via citizen scientists, in most cases local lifeguards. This study considered only the time frame when 40 beaches were reporting. The eight beaches which are the focus of this study (see Figure 1) were chosen because they were the only beaches with enough reports of high respiratory risk days to develop a convergent model, as described in the Methods.

Figure 1: Eight beaches along the Florida Gulf Coast out of 40 for which reporting is available from 2011-2019. These eight have the highest number of reported red tide respiratory events: six are in Sarasota County and two are in Manatee County.

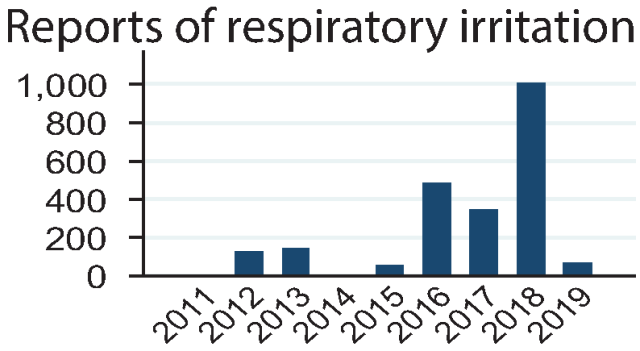

Figure 2: Reports of respiratory irritation caused by red tide for Sarasota County, from December 2011 to April 2019.

Figure 2 shows the annual aggregate sum of RT irritation reports (level 'slight' or higher) from the six beaches in Sarasota County. It is clear that in 2018, the county was especially hard-hit by RT.

For the purposes of the model, only the highest daily irritation level is considered. Reports are given twice per day, separated by only a few hours, and are often the same. When they differ, the higher of the four-tiered irritation level is used to describe the risk-level for that day. For the two-tiered irritation risk of high and low, there was near unanimous agreement between the two daily reports.

Correlation of irritation level across distance and time. From the BCRS database, correlation of the respiratory irritation level with nearby beaches is considered. For the four-tier irritation levels described as None to High (see Table 1), numerical values 1 through 4 were assigned, respectively.

As one can see in the left panel of Figure 3, the correlation of nearby beaches (within a few km) is high, but drops off to about 50% for beaches from 5 km up to approximately 25

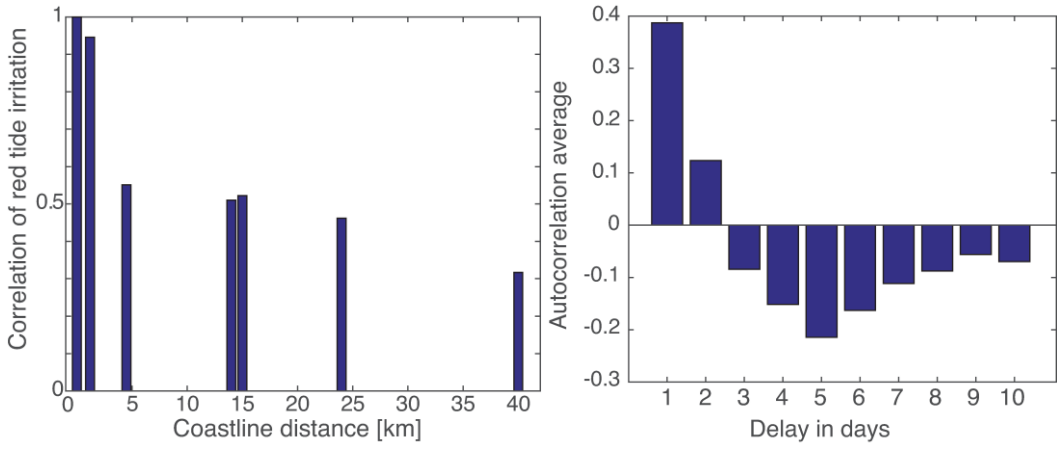

Figure 3: (left) Correlation of red tide respiratory irritation level between the different beaches in Figure 1 as a function of coastline distance. (right) The average auto-correlation of a beach's red tide respiratory irritation level with time.

km away, decreasing approximately monotonically with distance. One can also consider the correlation of irritation level across time for an individual beach. The average autocorrelation of a beach's respiratory irritation level versus time-lag is reported. Notice there is a moderate correlation for 1 day, but the correlation drops to about zero after 2 days. These spatiotemporal correlations are reported merely to describe the data set. They are not incorporated into the models described below.

4.4.3 Partition of data into training and testing sets

The BCRS database contains respiratory irritation reports from December 2011 to April 2019. Following standard practice in machine learning (Brunton and Kutz, 2019), a data set must be partitioned into a training and testing set. A model is constructed from the training set and validated on the testing set. Training on earlier data in order to test on later data is a common method as it mimics forecasting, and this approach will be followed in the current study. The data reveal that there was a timeframe of a significant number of reports during 2018 until early 2019 (Figure 2). The 2018-2019 time-frame therefore

emerges as a testing data set. All earlier data, from 2011-Dec-31 to 2017-Dec-31, are considered as the training data set.

The database has long stretches of no respiratory irritation reports (that is, recorded as None). For forecasting purposes, the ability to predict respiratory irritation during a cluster of such events is a primary focus of this study. To be precise, a *red tide respiratory irritation episode* is defined on a beach-by-beach basis for all data as follows. A RT respiratory irritation episode is said to begin the day when the BCRS irritation report (see Table 1) first goes above None and ends 7 days after the last irritation report above None.

4.4.4 Wind-based model

The wind direction reported from the BCRS at each beach was given as one of the eight usual directional octants of width 45° (N, NE, E, SE, S, SW, W, and NW). For the beaches of interest on the west coast of Florida, onshore winds were defined as winds blowing from 168.75° to 326.25° (S clockwise to NW, following (Stumpf et al., 2003, 2009)), which presumes the 330° to 150° orientation of the coastline, as shown in Figure 4. It is noted that the beach coastlines do not deviate enough from this assumed coastline for the coarseness of the input wind direction to make a difference in modeling.

For a wind-based model, the following statistical analysis from the BCRS database is performed for the training set (years 2011-2017), restricted only to RT respiratory irritation periods. For a respiratory irritation level of r_t on day t, where $r_t \in$ {None, Slight, Moderate, High}, the probability of r_{t+1} on day $t + 1$ is calculated, based on the frequencies of such occurrences in the database. Two conditions are considered: onshore winds on day $t + 1$

Figure 4: Definition of onshore and offshore wind directions for the beaches studied. The standard wind direction convention is used, where direction denotes where the wind is coming from.

And offshore winds on day $t+1$. The results are shown in Figure 5. For instance, if today's respiratory irritation level is Moderate, and there will be onshore winds tomorrow, then with over 60% probability, tomorrow's irritation level will be Moderate or High (high risk). On the other hand, if tomorrow's winds are offshore, then with about 60% probability the irritation level will improve, to Slight or None (low risk).

If this probability distribution is assumed to hold for future events, then one has a straightforward forecast model for the respiratory irritation level based on the weather forecast, in particular, the wind direction forecast. To get a deterministic model in place of a probabilistic model, one can assume that the state with the maximum likelihood is the one which occurs. This leads to the simple model given in Figure 6. For instance, if the irritation

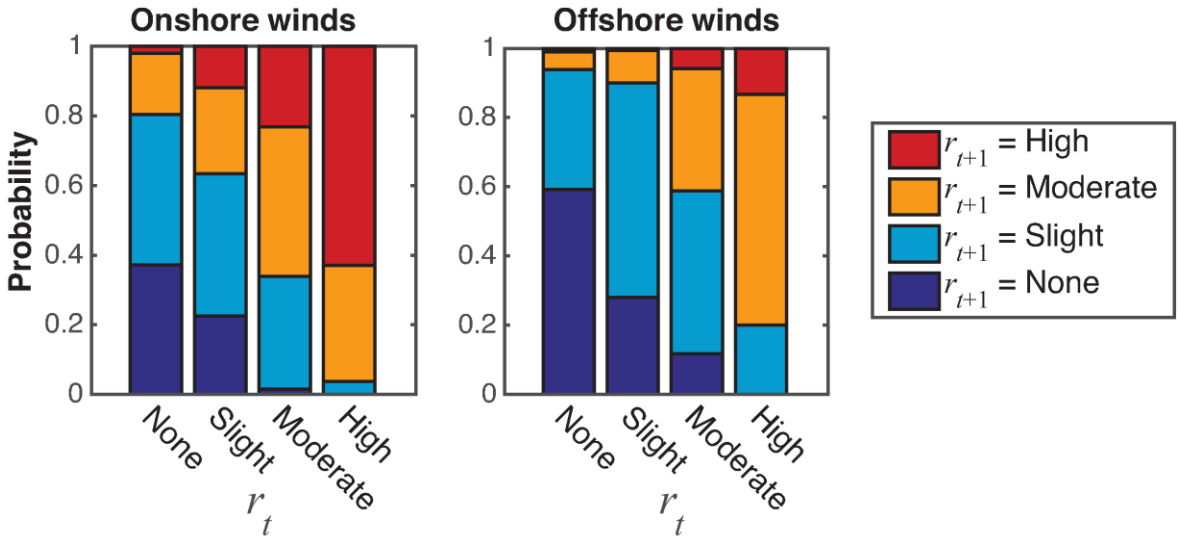

Figure 5: Respiratory irritation level on day $t + 1$ as a function of the level on day t and the wind condition on day $t + 1$; onshore or offshore winds.

level today is at None, but tomorrow has onshore winds, the maximum likelihood is that it will be Slight tomorrow, since the light-blue bar in the first stack of the left panel of Figure 5 is longer than all others. In place of the four-tiered irritation level, one can use the simpler two-tiered irritation risk level, low and high, as given in Table 1. This coarser, binary description of the irritation level is used as it is more amenable to modeling and validation.

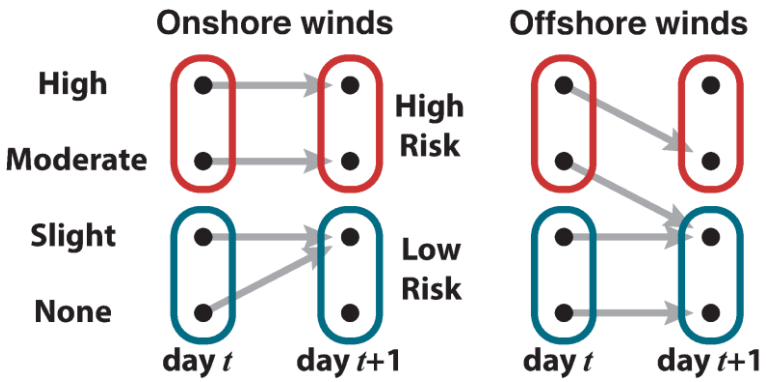

Figure 6: Wind-based respiratory irritation model.

4.4.5 Hawkes process model

Hawkes processes have been used to model a remarkable range of phenomena. From earthquakes (Ogata, 1988; Türkyilmaz et al., 2013), to gang related violence (Mohler et al., 2011; Park et al., 2021) to econometrics (Bacry et al., 2013; Affine Point Processes and Portfolio Credit Risk | SIAM Journal on Financial Mathematics, n.d.). This type of model performs well in situations where there is evidence for a clustering of events in time.

Hawkes processes are a type of temporal point process. The classic temporal point process is the *homogeneous* Poisson process, an example of which is the number of asteroids striking the Earth. Presumably the probability of an asteroid strike is independent of whether or not there was a previous strike. Poisson processes are thus "memoryless" and events are roughly equally spaced in time. An illustrative example of a homogeneous Poisson process compared to a non-homogeneous (Hawkes) Poisson process is provided in Appendix A.

A homogeneous Poisson process is a stochastic point process in which events happen with *constant* rate λ and with probability,

$$P_{\text{Poisson}}(k|\lambda) = \frac{(\lambda t)^k}{k!} e^{-\lambda t} \qquad (1)$$

where λ has units of inverse time. A *non-homogeneous* Poisson process is one in which the rate parameter $\lambda(t)$ is a function of time. A linear Hawkes process with an exponential kernel (HAWKES, 1971) is a non-homogeneous Poisson process where,

$$\lambda(t) = \lambda_0 + \sum_i \alpha e^{-\beta(t-\tau_i)} \qquad (2)$$

where $\lambda_0 \geq 0$ is the background intensity rate, $\alpha > 0$ is the excitation level, $\beta > 0$ is the reversion level, and $\{\tau_1, \tau_2, \ldots \tau_i\}$ is the observed true sequence of past event times (high risk days in the current study).

A Hawkes process is known as a *self-exciting process* because when an excitation happens the rate increases before decaying to the natural unexcited rate λ_0 (see Appendix A). The rate initially increases by the amount α when an event arrives but exponentially decays with rate β towards λ_0. The Hawkes process maintains a finite rate $\lambda(t)$ so long as $\alpha < \beta$ (Laub et al., 2015).

Estimation of the parameters for the Hawkes process is done via maximum likelihood estimation (MLE) of Fisher (On the mathematical foundations of theoretical statistics | Philosophical Transactions of the Royal Society of London. Series A, Containing Papers of a Mathematical or Physical Character, n.d.), a procedure for estimating model parameters from a training set such that the observed data is most probable (Brunton and Kutz, 2019). Details of MLE for a Hawkes process can be found in Appendix B. For each beach, the parameters λ_0, α, β, and $P_{\text{threshold}}$ are estimated based on the training data set for that beach. If the parameters converge to the same values independent of random initial parameters in the MLE process, the Hawkes model has *converged*. Only beaches which have a convergent Hawkes model are included in the Results. It is expected that not all, or even a majority of the beaches will have convergent Hawkes models, as it is known that for some types of

data, parameter estimation is quite sensitive to the random initial guess (Veen and Schoenberg, 2008).

Once the parameters $\{\lambda_0, \alpha, \beta, P_{\text{threshold}}\}$ have been estimated for a given beach, the probability of observing no events (high risk days) at each time is determined by substituting $\lambda(t)$ into eq. (1), where $\lambda(t)$ is given by eq. (2). This gives, on each day t, the probability of the next day, $\Delta t = 1$ d, being a high risk day, which is $1 - P_{\text{Poisson}}(0|\lambda(t))$, that is,

$$P_{\text{highrisk}}(t) = 1 - e^{-\lambda(t)\Delta t}. \quad (3)$$

The model predicts that the next day, $t + 1$, will be a high risk day if

$$P_{\text{highrisk}}(t) > P_{\text{threshold}}. \quad (4)$$

4.5 Results

The Hawkes process model parameter estimation was performed for the training data (years 2011-2017) at all 40 beaches in the BCRS database. The parameter estimation process converged at only 8 of the 40 beaches. They were located in a geographic cluster (see Figure 1) and from north to south are Manatee, Coquina, Lido, Siesta, Nokomis, Venice North, Venice, and Manasota. The set of parameters are calculated independently for each beach, and reported in Table 2. In all the beaches examined, the parameter

Beach	λ_0	α	β	$P_{\text{threshold}}$
Manatee	0.0027	0.2393	0.3151	0.2932
Coquina	0.0039	0.3181	0.4016	0.3451
Lido	0.0054	0.1324	0.2332	0.2600
Siesta	0.0059	0.2370	0.3700	0.3680
Nokomis	0.0041	0.1039	0.1218	0.3137
Venice North	0.0058	0.1457	0.1917	0.3211
Venice	0.0052	0.1449	0.2404	0.2785
Manasota	0.0049	0.2219	0.3182	0.3350
Average	**0.0047**	**0.1929**	**0.2740**	0.3143
(Standard Deviation)	(0.0011)	(0.072)	(0.094)	(0.036)

Table 2: Estimated values of the Hawkes parameters for each of the beaches considered, listed north to south. Units of λ_0, α, and β are inverse days, d^{-1}. The bottom rows shows the average parameter value (across all beaches) along with the standard deviation.

$\beta \approx 0.27$ d^{-1}, which suggests a correlation time-scale of $\beta^{-1} \approx 3.6$ days. A longer probabilistic "memory" timescale can be estimated,

$$T_m = -\log(0.05)/\beta + 1 \qquad \text{(in days)}, \tag{5}$$

which is about 12 days, since a high risk day which happened 12 days ago has a contribution of about 5% compared to that of high risk day which occurred 1 day ago. Also of interest is that the estimates show that $\alpha \approx 0.2$ d^{-1} for all beaches. This is roughly 10^3 times the base rate, $\lambda_0 \approx 0.005$, for each beach, meaning that a single high risk day after several low risk days increases the probability of more high risk days by several orders of magnitude.

The wind-based and Hawkes process models were applied to the test data at each of the eight beaches for which a convergent Hawkes process model was found. For comparison, a persistence model is included as a null hypothesis. The persistence model assumes that tomorrow will be like today. The results are reported in Table 3. For each beach and each

model, the accuracy is reported, or the percent of days for which the respiratory irritation risk was correctly forecast. Also given are the false negative rate (also called the miss rate) and the false positive rate.

Considering only the accuracy, the model which performs the best depends on the beach.

For the two northern-most beaches and Siesta, the Hawkes model is the most accurate. For the four southernmost beaches, the wind model performs best. Only at Lido does the simple persistence model perform best. But notice that even when a model is the most accurate, it might not have the lowest false negative rate, or percent of true high risk days that were not predicted. At all but the two northern-most beaches, persistence has the lowest false negative rate. At all but one beach (Siesta),

Beach and Time-frame	Model	Accuracy	False Negative Rate	False Positive Rate
Manatee, 181 days				
2018-Aug-03 to 2019-Jan-30	Persistence	77%	44%	16%
	Wind	78%	69%	5%
	Hawkes	80%	42%	13%
Coquina, 181 days				
2018-Aug-03 to 2019-Jan-30	Persistence	75%	46%	18%
	Wind	75%	68%	9%
	Hawkes	78%	44%	14%
Lido, 239 days				
2018-Jun-06 to 2019-Jan-30	Persistence	85%	36%	10%
	Wind	83%	62%	5%
	Hawkes	83%	56%	6%
Siesta, 237 days				
2018-Jun-08 to 2019-Jan-30	Persistence	83%	36%	12%
	Wind	84%	43%	8%
	Hawkes	85%	46%	6%
Nokomis, 239 days				
2018-Jun-06 to 2019-Jan-30	Persistence	80%	44%	13%
	Wind	82%	60%	5%
	Hawkes	74%	65%	14%
Venice North, 239 days				
2018-Jun-06 to 2019-Jan-30	Persistence	80%	43%	13%
	Wind	81%	61%	6%
	Hawkes	75%	64%	13%
Venice, 238 days				
2018-Jun-05 to 2019-Jan-22	Persistence	79%	47%	13%
	Wind	85%	53%	4%
	Hawkes	78%	59%	11%
Manasota, 232 days				
2018-Jun-07 to 2019-Jan-30	Persistence	81%	43%	13%
	Wind	87%	48%	3%
	Hawkes	78%	57%	11%

Table 3: For each beach, the percent of days for which the respiratory irritation risk was correctly forecast by each model during the dates shown is reported as the accuracy. Also given are the false negative rate (also called the miss rate) and the false positive rate.

the wind model has the lowest false positive rate (predicting a high risk day which is in fact low risk).

The self-excitation behavior characteristic of the Hawkes process can be seen in the example of Coquina Beach, Figure 7. The probability of the

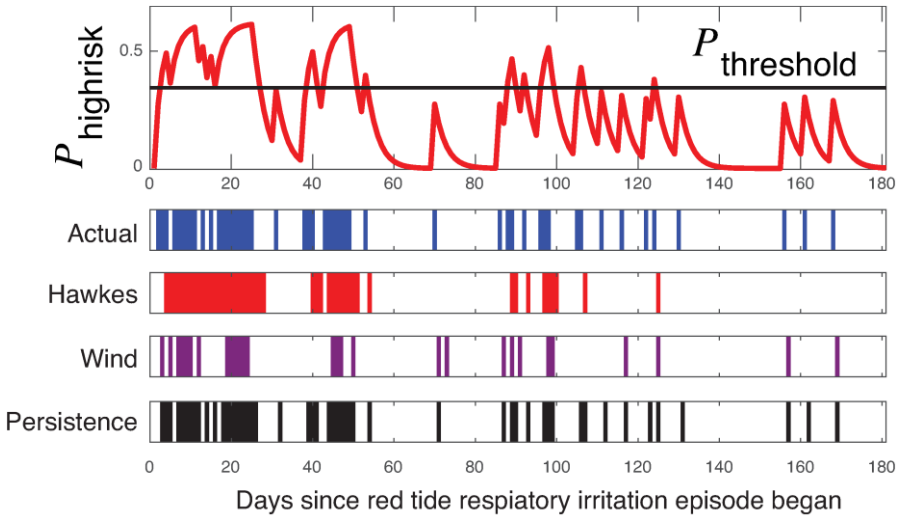

Figure 7: For Coquina Beach, Manatee County, Florida, the days of actual high respiratory risk level are shown, and several 1-day forecast models, during the red tide respiratory irritation episode that began August 2018. The probability of a high risk day using the Hawkes process model is shown at top. The flat black line represents the threshold. When the probability of a high risk day exceeds the threshold, the day is forecast as a high risk day. Otherwise, it will forecast as a low risk day. The Hawkes model performs best in this case. The wind-based and persistence models are shown for comparison.

275

following day being high risk is a function of all actual high risk days in the recent past. When the probability exceeds the threshold, the model predicts the following day will be high risk day. For this beach, the Hawkes model had the highest accuracy. The wind and persistence models are shown for

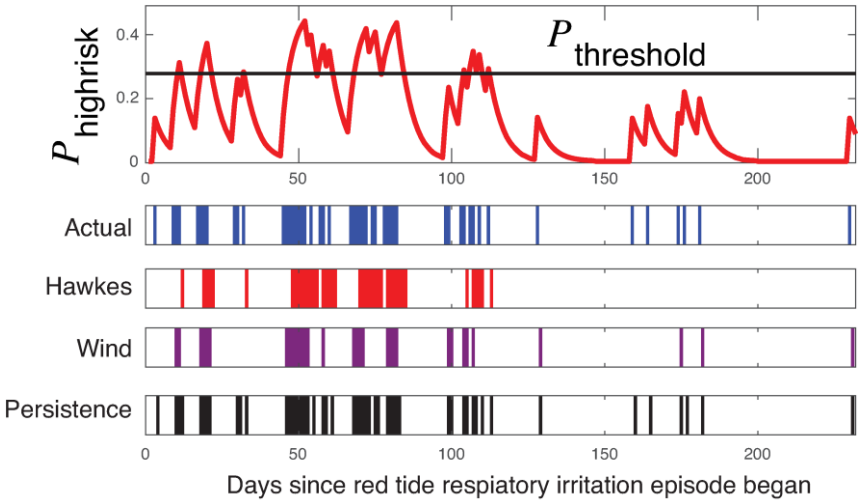

Figure 8: Same data as in Figure 7 but for Venice Beach, Sarasota County, Florida during the red tide respiratory irritation episode that began June 2018. The wind model performs best in this case.

comparison. Results for Venice Beach are also shown, an example where the wind model had the highest accuracy, in Figure 8.

4.6 Discussion

The BCRS has accumulated a significant amount of data since its launch in 2006. In the absence of a more sophisticated first-principles-based forecasting system, the historical data could be utilized to provide a near-term beach-level forecast at the locations considered. For forecasting the beach-specific respiratory irritation risk level one day ahead of time, all the models perform similarly during the 2018-2019 RT respiratory irritation episode, between 75% and 85% accuracy (see Table 3). The simple persistence model (tomorrow will be like today) does rather well, near 80% accuracy, and at one beach (Lido), was the best performer.

The wind-based model is the most accurate for half the beaches for which a model was developed. All were geographically located near each other, in the southern part of Sarasota County.

Interestingly, the probabilistic self-exciting Hawkes process model, which does not contain wind as an input, outperforms the more intuitive wind-based model at nearly half of the beaches. Fortuitously, there were enough events to get numerical estimates for the parameters of a univariate Hawkes process, but not enough for a multivariate analysis (i.e., including wind data). With additional data containing high-risk events, adding wind data to the Hawkes process model may be possible. That is, a hybrid of the models considered here could potentially improve accuracy, but the amount of historical data available to train the model would need to increase significantly.

Limitations. The given models do not predict when a RT bloom will occur, or when a RT respiratory irritation episode will occur at any given beach. However, when a RT respiratory irritation episode does begin, the models provide a method for forecasting the respiratory irritation risk for the next day, based on the recent risk history.

Data for all 40 beaches goes back only to December 2011. The total number of high risk days during the 2,193-day training period ranges from a low of zero to a high of 46. Among the eight beaches for which a model was developed, high risk days account for only about 1% of the training period. This is very little data for which to train a model. With more data, the Hawkes and wind models may improve.

Data from different blooms were lumped together to get enough data to train the models. Yet RT blooms are known to be patchy and highly variable from bloom to bloom. Thus, the training data may combine behavior from different blooms with different dynamics. This is a limitation of the data set used.

To simplify the modeling, the four-tiered respiratory irritation scale was coarsened into a two-tiered risk scale (Table 1). Ideally, respiratory irritation could be measured on a continuous scale, using for example sensors for automatic cough detection and counting at beaches. Modeling of a continuous variable would increase the number of available data-driven modeling methods.

4.7 Conclusions

The Beach Condition Reporting System which has been operational forover decade, has accumulated a wealth of data. In particular, red tide-induced respiratory irritation levels at individual beaches have been reported daily over this time period. The analysis performed here provides one of the first reports of the statistics of this data set.

Moreover, beach-level next-day forecasts of the respiratory irritation risk were developed on a beach-by-beach basis, if there was enough data in the training set for a model to be developed. Training on data from red tide respiratory irritation episodes during the time period 2011-2017, only eight beaches had enough data for a model to be developed (i.e., for parameter values for the probabilistic Hawkes model to converge). Two types of models provided a forecast of the respiratory level 24-hours ahead of time during the extensive red time bloom of 2018-2019, and were compared with a simple persistence model. One model was wind-based, using the current days' respiratory level and the predicted wind direction of the following day. The other model was a probabilistic self-exciting Hawkes process model, which used as input the record of the recent risk history. No single model performed the best at all the beaches. The wind-based model performed the best at four of the eight beaches, correctly predicting the respiratory risk level an average of 84% of the time. At three of the eight beaches, the Hawkes model was the most accurate,

accurately predicting the next day's risk level an average of 81% of the time. At one beach, the persistence model outperformed both the wind and Hawkes models, with an accuracy of 85%. The accuracy of the Hawkes process model at nearly half the beaches for which a model was developed suggests it may be fruitful to consider self-excitation-based approaches in larger-scale models of harmful algal blooms. Interestingly, the Hawkes process model does not require water samples of *K. brevis*, nor ocean or wind forecasts, and will likely improve by their inclusion.

These results suggest that beach-level on-site reports of respiratory irritation are a valuable data source, providing an excellent means to forecast the following day's beach-specific respiratory irritation risk at the same location. Moreover, the efficacy of the BCRS suggests that timely and regular reports of red tide-induced respiratory irritation level should continue to be supported and should be incorporated in operational forecasts used by resource managers and the public.

4.8 Acknowledgements

We thank the Mote Marine Laboratory & Aquarium, the Florida Fish and Wildlife Conservation Commission, the Sarasota County Beach Patrol, the Manatee County Department of Public Safety, the Marine Rescue Division, and all of the beach lifeguards, park rangers, and citizen scientists responsible for providing data into the Beach Conditions Reporting System. This project was partially supported by the Global Change Center, the Fralin Life Sciences Institute, and the Institute for Society, Culture, and Environment at Virginia Tech. Moeltner also acknowledges partial support by the USDA/NIFA Multi-State project #VA-136344. Ross acknowledges partial support by the National Science Foundation (NSF) under grant number 1922516.

Chapter 5. Predicting particle concentration in smoke plumes using imagery calibrated by direct sensing

Landon Bilyeu ORCID[1], Noor Janjua[2], Regina Hanlon ORCID[1], Hosein Foroutan ORCID[3], Shane D. Ross ORCID[4], Manu Nimmala ORCID [5], and David G. Schmale III ORCID[1*]

[1]School of Plant and Environmental Sciences, Virginia Tech, Blacksburg, VA, USA

[2]Computational Modeling and Data Analytics, Virginia Tech, Blacksburg, VA, USA

[3]Department of Civil and Environmental Engineering, Virginia Tech, Blacksburg, VA, USA

[4]Department of Aerospace and Ocean Engineering, Virginia Tech, Blacksburg, VA, USA

[5]Engineering Science and Mechanics, Virginia Tech, Blacksburg, VA, USA

***Corresponding author:**

David G. Schmale III, dschmale@vt.edu / Phone 540-231-6943/ FAX 540-231-7477

Status: Draft

5.1 Abstract

New information is needed to monitor the distribution and identify emission sources of aerosols. Plumes of colored smoke were generated using small smoke emitters, and a series of fixed (ground) and mobile (drone) sensors were used to sample and track the plumes at different distances from the source. Concentrations of particles 0.5 microns and larger observed with optical particle counters (OPCs) ranged from 400 to 27000 cm^{-3} of air at ground level, with decreasing concentrations observed at greater distances downwind from the emitters. An OPC mounted on a drone was used to sample the smoke plume at different heights and distances from the emitters, with in-plume concentrations of particles ranging from 490 to 21086 cm^{-3} for three different flights. Top-down drone imagery was processed to extract color profiles of the smoke intensity using two methods. In the first method, an image-processing algorithm was developed to categorize smoke intensity into five different intensity levels using RGB values. This imagery data was combined with OPC measurements to match the smoke intensity levels with particle concentrations at specific times and distances from the emitters. A neural model was created to predict smoke concentrations from RGB drone image-based intensity levels, and the best model was able to accurately predict smoke intensity from the measured smoke concentrations with an R-Squared of 0.764. The Second method of smoke intensity detection trained a machine learning model, Detectron2, classifies and segments the plume in both top-down drone imagery and side-view imagery (ground-based cameras). Smoke plume intensity within the segmented plume was then estimated using hue saturation value (HSV) values. After matching the plume intensity values with particle concentrations, a new neural model was developed that resulted in a particle concentration prediction equation with an R-Squared of 0.532. This study develops novel methodologies for airborne dispersal through image-processing and particle sampling. This information is critical for the development of targeted mitigation strategies to reduce exposure

risks and alleviate the adverse effects of aerosol-induced pollution on ecosystems and public health.

5.2 Introduction

Aerosols may contain harmful toxins, irritants, pollen, pathogens, or smoke (Pierce et al., 2003; Wei et al., 2009). New techniques are needed to track the sources and transport of aerosols (Wei et al., 2009; Esfahlani, 2019; Mommert et al., 2020; Mtz-Enriquez et al., 2020; Taha et al., 2022). Insights gained from aerosol tracking may contribute to targeted mitigation strategies to reduce exposure risks and alleviate the adverse effects of aerosol-induced pollution on ecosystems and public health (Jimenez et al., 2003; Kirkpatrick et al., 2011; Moeltner et al., 2022). In recent years, sensors onboard drones (uncrewed aerial systems) have been used to track the movement of aerosols in the atmosphere (Esfahlani, 2019; Rahman et al., 2021).

Improved methods are necessary for tracking aerosol plumes as they move through the environment (Mommert et al., 2020). Cost-efficient optical particle counters (OPCs) are valuable tools for real-time measurement of particle movement (Giordano et al., 2021). For example, OPCs can provide insights into airborne particle dynamics within a sampling area (Zhao et al., 2012; Wiedensohler et al., 2013), and deliver accurate measurements of both high and low particle concentrations under varying weather conditions (Heim et al., 2008; Dubey et al., 2022). Integrating OPCs into drone platforms has allowed for the sampling of plumes that are otherwise inaccessible or too hazardous for human sampling (Rahman et al., 2021; Bilyeu et al., 2022; Hanlon et al., 2022).

High-volume air filter samplers can complement OPC measurements, particularly in situations where low concentrations of particles may be observed (Marple et al., 1990; Vincent, 2007). The

increased sampling volume improves the overall effectiveness of monitoring efforts and provides a cumulative measurement of particulate matter levels throughout a sample period (Bishop et al., 2012). Imagery can also complement OPCs, allowing real-time visualization of particle plumes and identification of areas with varying airborne particle concentrations (Ho and Kuo, 2009; Wei et al., 2009; Feng et al., 2020).

Visual aerosol tracking is commonly used for smoke detection (Ho and Kuo, 2009; Rahman et al., 2021), which is crucial for the early identification and monitoring of wildfire movement (Holm et al., 2021; Rahman et al., 2021; McClure et al., 2023). Advancements in computer vision and machine learning have led to extremely accurate object detection models, which can be utilized for smoke detection and analysis, with research employing deep learning architectures such as regional-based convolutional neural networks. Visual smoke tracking is typically performed to track the movement of wildfire, but additional work is needed to estimate smoke concentrations from images (Ho and Kuo, 2009; Frizzi et al., 2016). Some progress has been made in using satellite imagery to track smoke and fires. However, this data is limited to regions within satellite coverage and often experiences delays due to the time needed to access the data (Chen et al., 2022). Images from drones have been used to study plumes of dye in water, and these techniques could be applied to terrestrial environments (Powers et al., 2018; Filippi et al., 2021). While some research primarily focused on using the HSV color space (hue, saturation, and value) for smoke segmentation in images, the information obtained from this color space can also aid in interpreting the relative concentration of smoke plumes (Xing et al., 2015). The saturation channel refers to how intense a color is, while the value channel refers to the relative lightness or darkness of a

color. Utilizing the saturation and value channels of a smoke pixel can provide insights into the concentration of a smoke plume, thanks to the semi-transparent nature of smoke.

Although significant progress has been made in aerosol tracking using individual sensing techniques (Ho and Kuo, 2009; Wiedensohler et al., 2013; Crilley et al., 2020), a combination of sensors can be used to develop a model which extracts more information from drone imagery alone. This approach reduces the need for deploying multiple sensors within a plume. In this paper, we describe a series of release-recapture experiments to track the movement of colored smoke from a series of small smoke emitters. We hypothesized that concentrations of aerosols in colored smoke (cm^{-3}) can be predicted in the plume by using top-down drone images and side view shots from fixed cameras. To test this hypothesis, we conducted drone-based and ground-based sampling of plumes of colored smoke at different distances from the source. Empirical data were used to validate estimations of plume intensity from processed drone images, and a neural model was developed to predict concentrations of aerosols in smoke at different distances from the source. Our specific objectives were to: (1) monitor plumes of colored smoke at different distances from the source using a series of fixed and mobile sensors under varying weather conditions, (2) evaluate the potential for imagery to accurately estimate concentrations of aerosols in colored smoke, and (3) create prediction models which can identify plume area and intensity as well determine which model provides the most functionality in different use cases.

5.3 Methods and Materials

5.3.1 Study Site

The study was conducted at Virginia Tech's Kentland experimental aerial systems (KEAS) laboratory in Blacksburg, Virginia (**Figure 1**). Drone mounted sensors and video footage from a drone platform and several ground-based cameras were used alongside ground sensors to measure smoke plume intensity. Smoke was produced by setting off smoke emitters (Enola Gaye), activated one at a time over a 20-minute period. Smoke was released centrally on the KEAS's runway (Site: 37.197147, -80.578041). Three smoke release periods were sampled for 20 minutes each. Each emitter contained 50 grams of composition weight, and 18 emitters were released during each period, releasing 0.6 g s^{-1} of particles (Wire Pull Smoke (WP40) - EG Products, 2020). During each release, a drone-mounted OPC was used for the first half, followed by drone video for the second half. At the sample site, six high-volume filter samplers and three OPCs were used in varying layouts to measure the plume intensity (**Table 1**).

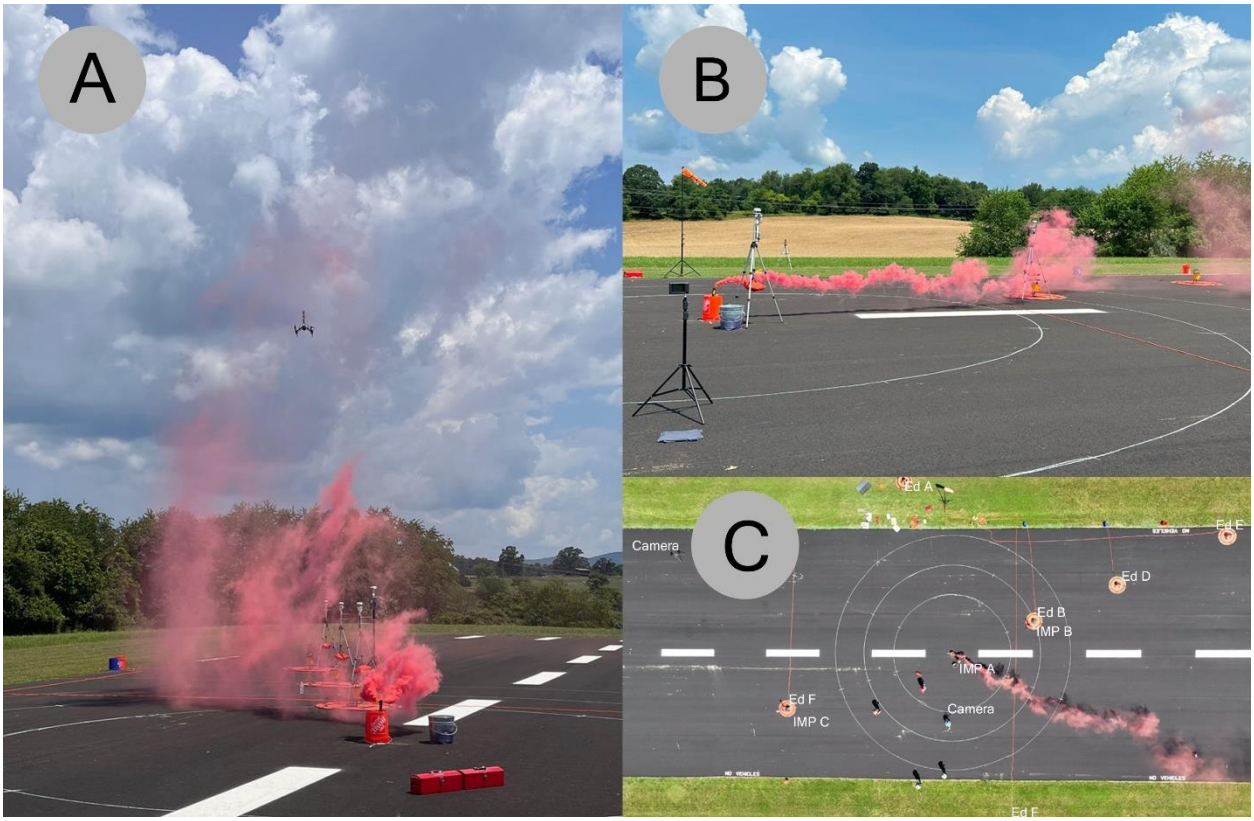

Figure 1. 3 panels depicting the smoke release experiments. Panel A shows smoke passing over ground sampling devices with a drone sampler flying overhead. Panel B shows a different configuration of ground sampling devices with high wind speed creating a low plume. Panel C shows the top-down image of smoke release as captured by the drone video camera.

Table 1.

Sampler ID	Sample Start Time (EDT)	Sample End Time (EDT)	Distance from Base (m)	Direction from Base	Release Period	Emitters Released
Ed A	11:20 AM	11:40 AM	15	NW	1	18
Ed B	11:20 AM	11:40 AM	7.5	NE	1	18
Ed C	11:20 AM	11:40 AM	15	SE	1	18
Ed D	11:20 AM	11:40 AM	15	NE	1	18
Ed E	11:20 AM	11:40 AM	25	NE	1	18
Ed F	11:20 AM	11:40 AM	15	SW	1	18
Ed A	12:10 PM	12:30 PM	5	NE	2	18
Ed B	12:10 PM	12:30 PM	10	NE	2	18
Ed C	12:10 PM	12:30 PM	15	NE	2	18
Ed D	12:10 PM	12:30 PM	10	SE	2	18
Ed E	12:10 PM	12:30 PM	10	NW	2	18
Ed F	12:10 PM	12:30 PM	10	SW	2	18
Ed A	1:10 PM	1:30 PM	5	NW	3	18
Ed B	1:10 PM	1:30 PM	10	NW	3	18
Ed C	1:10 PM	1:30 PM	15	NW	3	18
Ed D	1:10 PM	1:30 PM	10	NE	3	18
Ed E	1:10 PM	1:30 PM	10	SW	3	18
Ed F	1:10 PM	1:30 PM	10	SE	3	18
OPC A	11:20 AM	11:40 AM	7.5	NE	1	18
OPC B	11:20 AM	11:40 AM	0	N/A	1	18
OPC C	11:20 AM	11:40 AM	15	SW	1	18
OPC A	12:10 PM	12:30 PM	5	NE	2	18
OPC B	12:10 PM	12:30 PM	10	NE	2	18
OPC C	12:10 PM	12:30 PM	15	NE	2	18
OPC A	1:10 PM	1:30 PM	5	NW	3	18
OPC B	1:10 PM	1:30 PM	10	NW	3	18
OPC C	1:10 PM	1:30 PM	15	NW	3	18
DR V	11:30 AM	11:41 AM	0	N/A	1	18
DR V	12:20 PM	12:29 PM	0	N/A	2	18
DR V	1:18 PM	1:38 PM	0	N/A	3	18
DR OPC	11:20 AM	11:25 AM	15	NE	1	18
DR OPC	12:10 PM	12:16 PM	10	NE	2	18
DR OPC	1:10 PM	1:15 PM	N/A	Follows smoke	3	18

Table 1. Sampler name, start time, stop time, distance, direction from the smoke source, and number of smoke emitters released during sampling period is shown for the sampling equipment during the July 6, 2023, smoke release experiments. Ed refers to the high volume filter samplers. IMP refers to the ground-based sensors containing OPC and weather sensors. DR V refers to the drone collecting video data. DR OPC refers to the drone with the mounted OPC.

5.3.2 Ground-based air particle concentration and weather monitoring

An integrated sensor system, including weather monitoring and an OPC, was used for ground measurements approximately 2 m above ground level (labeled OPC A, OPC B, and OPC C) (Bilyeu et al., 2022). Weather data was collected using an Atmos 22 sonic anemometer measuring windspeed, wind direction, temperature, and relative humidity at about 1 Hz. The impinging device and OPC (Plantower PMS 7003) operated under the same system as described for the drone-based particle monitoring system in Bilyeu et al. (Bilyeu et al., 2022). The OPC recorded particle number concentrations as the number of particles with diameter over 0.5 μm in 0.1 L of air, which were then converted to particle number concentrations per cubic centimeter (cm^{-3}). The ground sensors differed from the drone-based sensor (DR OPC) only in that they were manually started and stopped, allowing longer run times since drone battery life was not a limiting factor on the ground-based packages. Sensors were arrayed to mimic a previous experiment done for pollen release (Nimmala et al., 2023), as well as a layout downwind to show the effects of distance on plume intensity and shape. Six air samplers (Science First High-Volume Air Samplers) were used alongside the OPCs, positioned approximately 0.3 meters above the ground at fixed locations (**Table 1**). The samplers drew air at 650 L/min onto Whatman Grade 1 Cellulose 125 mm, 11 μm pore size filter paper, which collected particles from the emitted smoke.

5.3.3 Drone-based measurements

Two different drone platforms were used for tracking the smoke plume: one equipped with an OPC and impinging device (DJI Inspire 2, labeled DR OPC), and another equipped with a downward facing gimballed camera (DJI Mavic Air 2, labeled DR V). During the first half of each smoke release period, the OPC and impinging drone was flown above the ground samplers, moving into and out of the plume at a height of 10 meters +/- 30 cm. The sampling setup for this drone was the same as described in Bilyeu et al. (Bilyeu et al., 2022). The drone used to capture images of the plume was flown 30 meters +/- 30 cm above the smoke release point with the camera pointed directly at the ground. The video was recorded in 4k resolution at 120 Hz, capturing approximately 10 minutes of smoke release for each release period.

5.3.4 Optical particle counter (OPC) calibration

The Plantower PMS 7003 OPCs were found to inaccurately measure total particle concentrations and sizes when compared to more expensive and reliable instruments such as the Aerodynamic Particle Sizer (APS) (TSI Model 3321, Shoreview, MN, United States). In some cases of low particle concentrations one OPC would measure twice the concentration of another OPC and be significantly different from the values measured by the APS. Polystyrene latex beads with mean sizes of 0.8 µm, 2 µm, and 10 µm were chosen to be released in an attempt to calibrate the OPCs total and individual bin particle counts (which are reported to sort particles into size bins ranging from 0.3-0.5 µm, 0.5-1.0 µm, 1.0-2.5 µm, 2.5-5.0 µm, 5.0-10 µm, and greater than 10 µm particle diameter). Utilizing a nebulizer with HEPA filtered air we aerosolized the polystyrene latex beads and passed the aerosol through a dryer (TSI Model 3062, Shoreview, MN, United States), a Kr85 neutralizer (TSI, Shoreview, MN, United States), and into a 280L chamber

(AtmosBag two-hand, size M, Cat. #Z530212, Sigma-Aldrich, St. Louis, MO, United States) as per Powers et al.(Powers et al., 2018). Utilizing the APS the true aerosol size distribution and concentration were determined. Air was released into the chamber before the beads were added to run an empty bag test prior to each bead release period. Beads were released one size group at a time allowing 5 minutes to fill the bag, after which the APS and OPCs began recording data during a 3-minute interval collecting 18 samples for each of the three different bead size releases. Measurements from the Plantower PMS 7003 OPCs were compared with true values from the APS and the Microsoft Excel solver function was utilized to fit the OPC data to the APS data (see S. Equation 1-4).

5.3.5 High-volume air filter calibration

High-volume air filters (labeled Ed A, Ed B, Ed C, Ed D, Ed E, and Ed F) were calibrated by releasing smoke directly from the smoke emitters onto the filters for set periods of time---2, 5, 10, and 15 seconds---replicated three times. High-volume filter samples were collected and taken to the lab where five 1 cm cuttings were taken from each sample and soaked in a 1mL 25% ethanol solution. The red smoke collected in the filter stained the liquid solution, which was then run through a Beckman Coulter DU 800 spectrophotometer (Brea, California, USA) to measure absorbance at the peak of 515 nm. Measurements were taken in triplicate and averaged for each sample.

5.3.6 Data storage and analysis

Data from OPCs were saved to microSD cards as CSV files and processed in Microsoft Excel to remove corrupted data. Excel was also used to convert the raw data to corrected particle concentrations for comparison between multiple OPCs. Associations linking particle concentration with wind speed, wind direction, and temperature were analyzed in Excel, and statistical analyses were performed with JMP Pro Version 16 software (Cary, North Carolina, USA). Weather data were saved on the same files as the OPC data and were converted from 0-360 degrees to a 0-180 degree scale. In this scale, 180 degrees represented the wind blowing directly from the source (smoke emitter) toward the sampler, and 0 degrees represented the wind blowing directly from the sampler to the source (**Figure 2**).

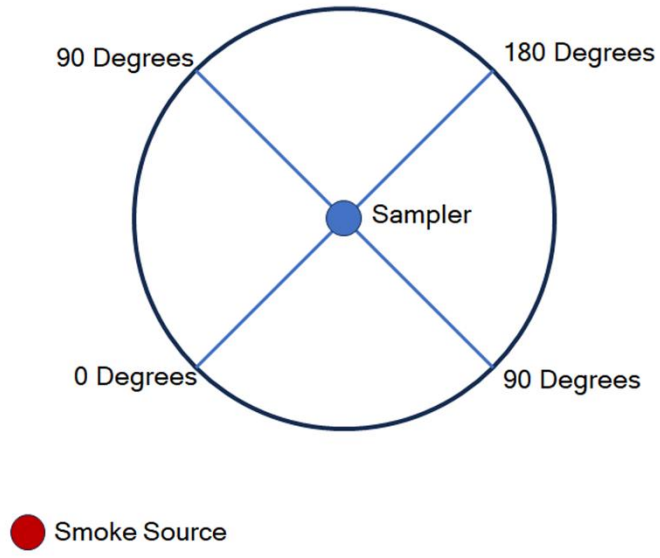

Figure 2. The method of wind direction processing for each ground sampler with an attached weather sensor. When the wind blew in the 180 degree line from the smoke source to the sampler it was set to 180 degrees and when the wind blew from the sampler towards the smoke source it was set to 0 degrees. Each direction had a range of 1 to 180 degrees. Crosswinds from either direction would be 90 degrees.

Two methods were used to process the drone imagery (videos) both utilizing Adobe Media Encoder 2024 (San Jose, California, USA) software to convert the video into still frames. The technique of extracting color intensity was similar to that done by Filippi et al. (Filippi et al., 2021) when they released colored dye into the ocean to track surface drift. In the first method the frames were further analyzed using an in-house MATLAB code (supplemental code 1) to determine the relative intensity of the smoke plume. The analysis used the red values of each pixel, creating four different intensity levels based on the difference between red values and green and blue values. The intensity levels were categorized as 4, 3, 2, and 1, corresponding to differences of 100, 50, 20, and 10, respectively. These bins were chosen as they were found to be the most consistently correlated with measurements taken from out OPCs, with greater numbers of bins decreasing the accuracy of matching intensity level to particle concentration. By matching the time stamps of the OPC data and the video recording of the smoke plume, we created a range of particle concentrations for each intensity level from images extracted from the drone video. OPC concentrations were matched with the plume intensity as measured by the sensors, and values were sorted into concentrations for each intensity level. The average concentration and standard deviation were determined using Microsoft Excel and JMP software.

The second method took the still frames and utilized the implementation of a machine learning model Detectron2, an open-source object detection and segmentation model developed by Facebook AI Research, to segment the smoke plumes(facebookresearch/detectron2, 2024). This method employed a Mask R-CNN model with a ResNet-50 backbone and Feature Pyramid Network, pre-trained on the COCO dataset and fine-tuned for smoke plume segmentation. Randomly picked images from cameras placed around the smoke release area were used for

training and validation and were prepared using COCO format annotations and registered with Detectron2's catalogs. The model was trained with Detectron2's DefaultTrainer with parameters including a learning rate of 0.00025 and 1000 iterations. A smoke concentration visualization function was implemented using OpenCV. To estimate smoke plume intensity the segmented plume image was converted to the HSV color space and a mask for reddish hues within the plume was applied. We then extracted the averages of the saturation and value channels for interpretation of the intensity of the smoke. Afterwards, we applied a Gaussian blur for smoother results and generated a corresponding heatmap for varying intensities within the plume. This method involves using a continuous color bar for the corresponding intensities, specifically a range of values from 0-255 since this was OpenCV's default range.

JMP 16 Pro software was used on data collected from ground OPCs along with matching smoke intensity levels to create prediction models for smoke intensity levels and for particle concentrations. Smoke intensity level was read at one pixel near to each ground OPC during the entire release periods. By using the neural modeling JMP software the smoke intensity levels from one sensor were used as an input for determining the particle concentrations measured by said sensor. Another model was created using smoke concentration to determine smoke intensity level utilizing the same measured pixels and OPC measured concentrations. A third model was created using the value and saturation of pixels measured near to the OPCs and one set was utilized to predict particle concentration at the OPC. The models were made by using the neural modeling 3 node TanH model provided in the JMP 16 Pro software. In each instance the model was trained on 1/3 of the data set and contained 1 hidden layer.

5.4 Results

The smoke release experiments were performed on 6 July 2023 involving three release periods of 18 smoke emitters, each release period lasting approximately 20 minutes. The release periods began at 11:20 AM, 12:10 PM, and 1:10 PM. During these times, three ground-based OPC and six high-volume air filter samplers collected data continuously. During the first approximate 10 minutes of the smoke release a drone mounted OPC was in flight sampling the smoke plume, and during the second approximate 10 minutes of the smoke release a drone was flown 30 meters above the smoke release to capture video of the sampling space. Ground-based cameras also collected captured video of the sampling space.

5.4.1 Ground particle concentration measurements

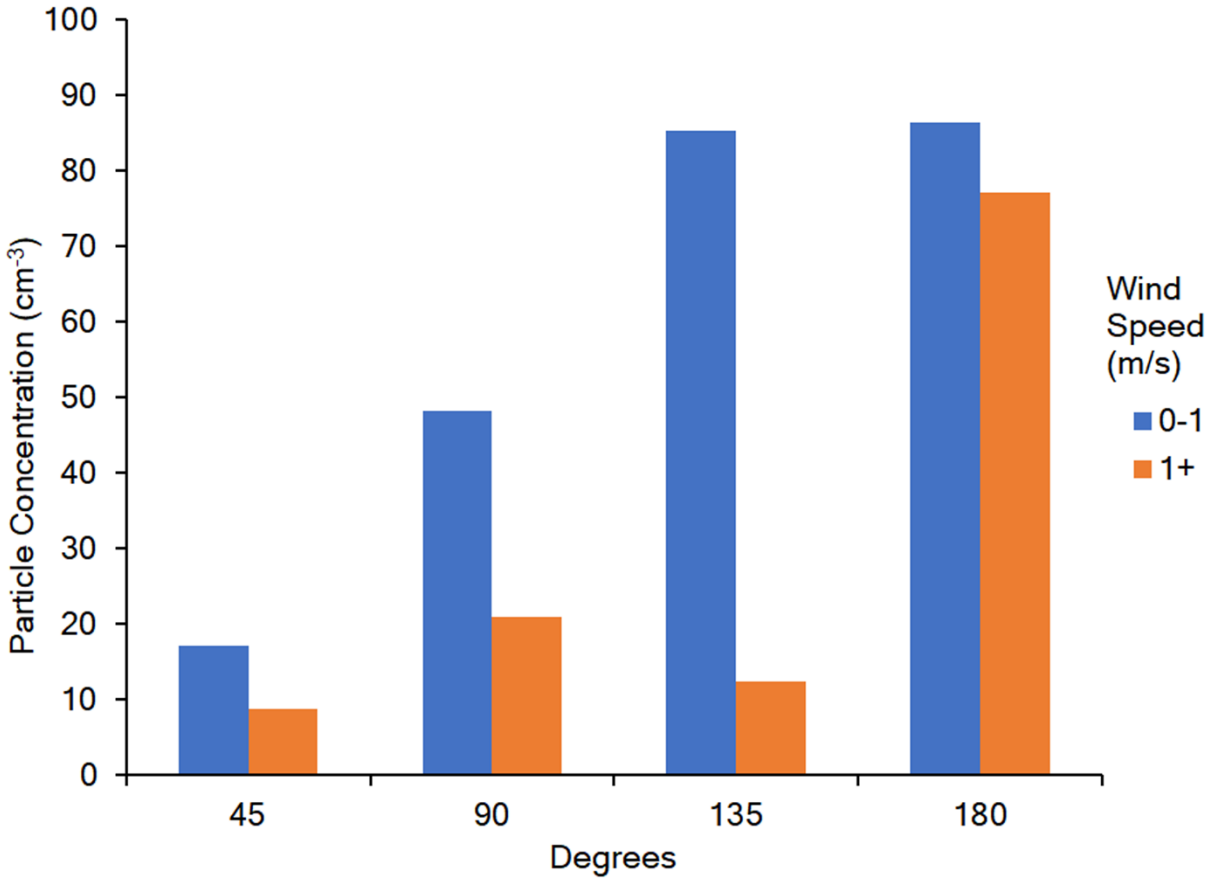

Figure 3. The correlation between wind speed and direction with the particle concentration measured 10 meters from the smoke plume source. Higher concentrations are associated with wind direction blowing the plume towards the sampler, and lower wind speeds are associated with higher particle concentrations when the wind is not directly towards the sampler.

During all of our sampling periods, wind speed and wind direction were correlated with particle concentration (**Figure 3**). However, wind direction had a more significant impact on particle concentrations, with the effect of wind speed being overshadowed. Background particle concentrations ranged from as low as 400 cm^{-3} outside the smoke plume to peaks reaching the sensor's maximum of 27000 cm^{-3} within the highest intensity of the plume. When looking at our downwind OPC orientation in release period 2 and 3 the closest OPC (OPC A) had a range of 400-27000 cm^{-3}, the middle OPC (OPC B) had a range of 400-19000 cm^{-3} while the farthest

OPC (OPC C) had a range of 400-26400 cm^{-3}. We can see differences in plume intensity shown in OPC measured values as well as plume intensity readings when looking at combined video and OPC data (**Figure 4**). The background particle concentration level was chosen by using the measurements of OPC A, OPC B, and OPC C when not in the smoke plume and was determined to be less than 1000 cm^{-3}. During release period 2 and 3 the value reported by the closest OPC averaged 9539 cm^{-3} for the reported seconds above the background particle concentration (229 of 1603 or 14.3%), the middle OPC averaged 7903 cm^{-3} for the reported seconds above the background particle concentration (187 of 1606 or 11.6%), and the farthest OPC averaged 9230 cm^{-3} for the reported seconds above the background particle concentration (89 of 665 or 13.4%). Particle concentrations greater than 20000 cm^{-3} during release periods 2 and 3 were reported by the closest OPC for 70 of 1603 (4.37%) seconds and the farthest OPC for 11 of 665 (1.65%) seconds.

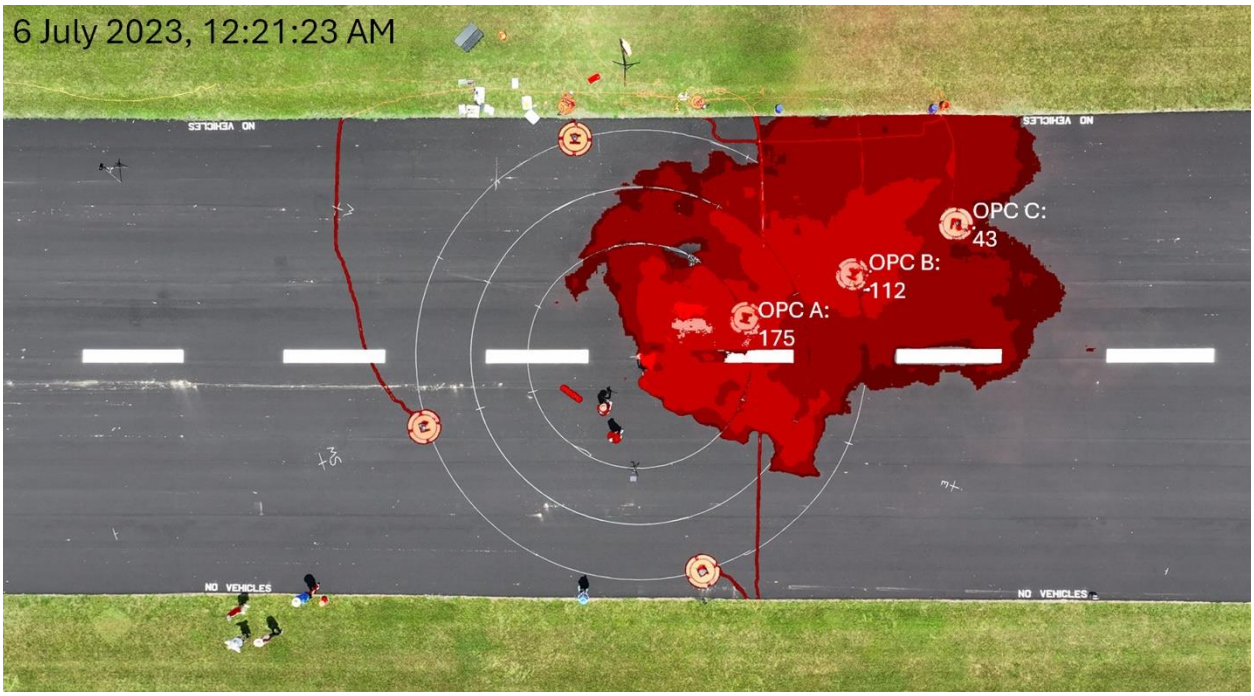

Figure 4. Optical particle counter measurements to have higher concentrations of smoke the closer the sensor was to the plume source, as seen with OPC A having a higher concentration of particles than OPC B despite similar smoke intensity levels.

5.4.2 High-volume filter measurements

Our equipment was arranged to capture upwind, sidewind, and especially downwind directions. However, the wind direction changed during the sampling period, often resulting in the crosswind setup receiving the majority of the smoke plume. Distance from the plume source also appears to impact plume intensity, with sensors closer to the source recording higher concentrations than those farther from the smoke plume source (**Figure 5**). This is seen particularly clearly in the absorbance measured in the high-volume filter samples where during release period 1, Ed B, Ed D, and Ed E were downwind at 7.5, 15, and 25 meters, respectively. We see Ed B had 0.24 absorbance, Ed D had 0.18 absorbance, and Ed E had 0.12 absorbance. A similar downward trend was also seen in release period 2 and 3 where Ed A, Ed B, and Ed C were downwind at 5, 10, and 15 meters, respectively. Ed A had 0.14 absorbance, Ed B had 0.10 absorbance, and Ed C had 0.06 absorbance during sampling period 2 and Ed A had 0.11 absorbance, Ed B had 0.04 absorbance, and Ed C had 0.0 absorbance during sampling period 3.

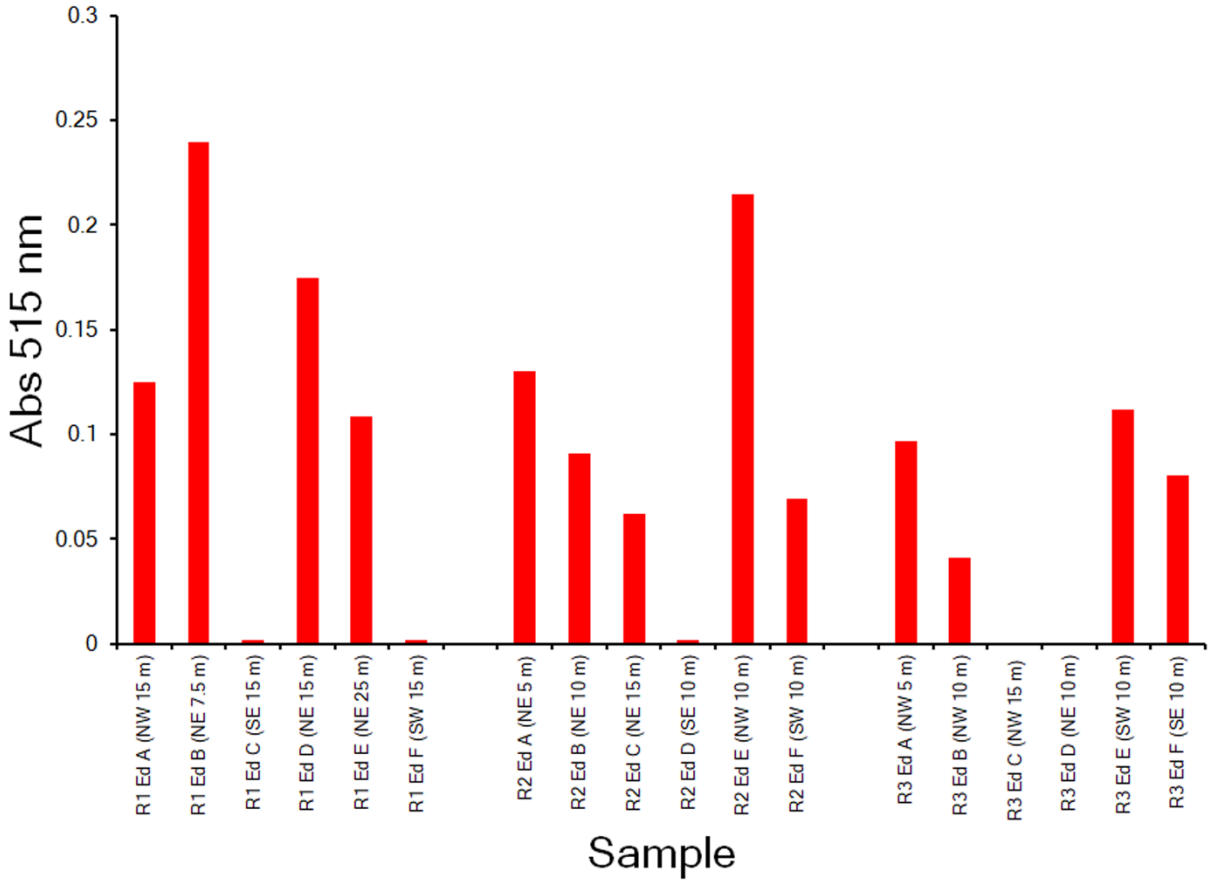

Figure 5. The absorbance measured from each of the 6 high volume samplers. R1 refers to the first sample period, R2 the second sample period, and R3 the third sample period. In R1 Ed samplers B, D, and E were downwind at 7.5, 15, and 25 meters, A and F were crosswind at 15 meters and C was upwind at 15 meters. For R2 and R3 Ed samplers A, B, and C were downwind 5, 10, and 15 meters, D and E were crosswind at 15 meters, and F was upwind at 15 meters. We see as distance increased for our downwind samplers that absorbance decreased, meaning less exposure to smoke was measured as the distance from the plume increased.

5.4.3 Drone measurements

5.4.3.1 Drone optical particle counter measurements

During the first two releases, the drone was flown above a downwind ground sensor. Weather conditions, such as low wind speed, caused the drone OPC to show higher concentrations of particles simultaneously with the ground OPC. However, under high wind speeds, the smoke plume went below the drone-mounted OPC, resulting in increased concentrations at ground level

but not in the air 10 meters above (**Figure 6**). Specifically, the drone-mounted OPC measured an average particle concentration of 4084 cm^{-3} under wind speeds 0.1 to 1 m/s, and 2155 cm^{-3} under wind speeds 1 to 2.7 m/s, respectively. Wind speeds measured from 0.1 m/s to 2.7 m/s. When flying the drone into and out of the smoke plume, we observed clear spikes in particle concentrations that could be matched with video footage taken from the ground.

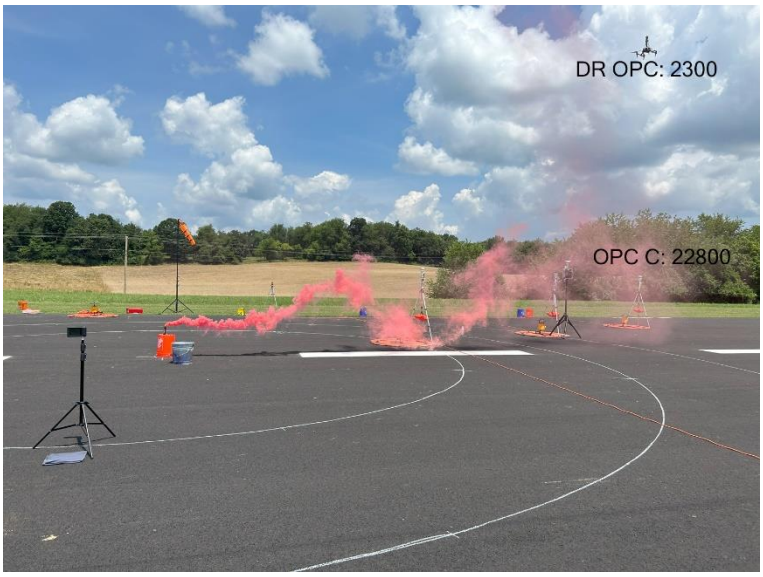

Figure 6. A side view of a period when the drone mounted sensor (DR OPC) was flying above OPC C (12:14:32 PM July 6th, 2023). OPC C is within the plume while the drone sensor was above the plume, which is shown by a high concentration measured from OPC C and a much lower concentration measured from the drone mounted sensor.

5.4.3.2 Drone video

For the RGB image processing we saw that the interior of the plume close to the source showed the highest intensity, while the outside of the plume near to the source showed the lowest intensity (**Figure 7**). As the plume expanded downwind, the intensity level decreased throughout, with even the interior of the plume showing lower levels of intensity (**Figure 7**). The video struggled to capture areas of the plume with very low intensity, causing the edges of the plume to be unmarked by the image processing program.

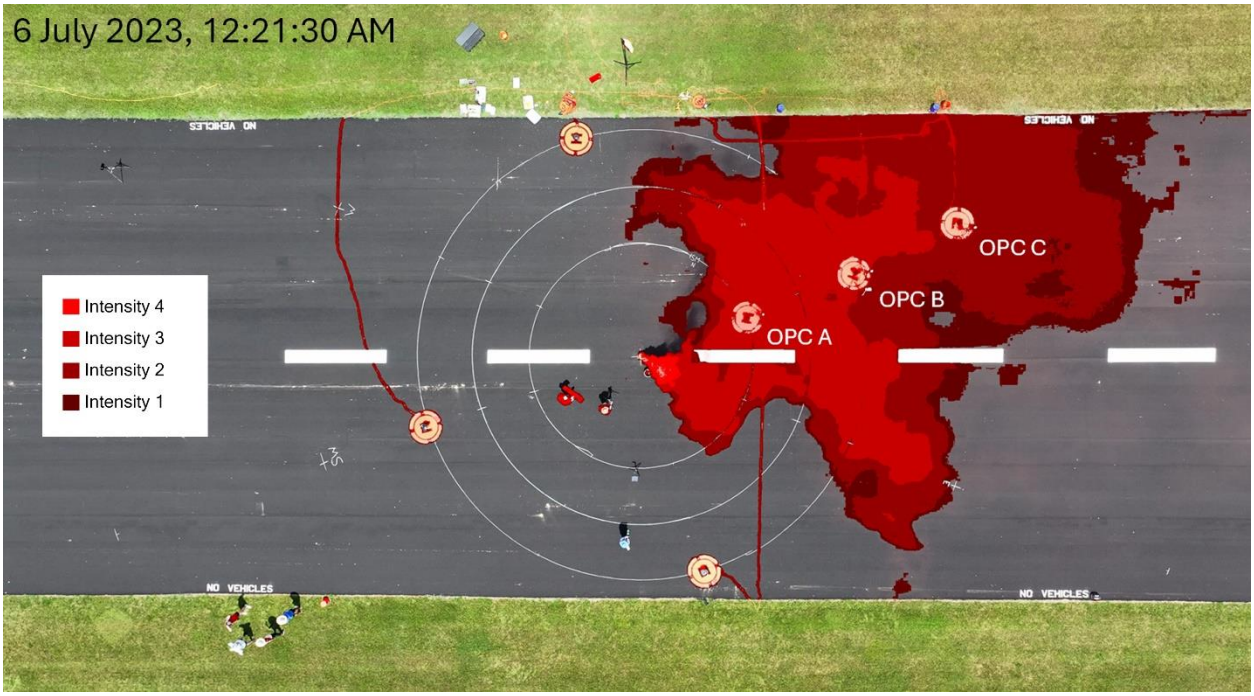

Figure 7. The smoke plume as seen from above by the drone processed into 4 different intensity levels. The edges of the smoke plume near to the source can be seen to be level 2 with the center being level 4. As the distance from the source increased, the center of the plume intensity level tapered off from level 3 (at OPCs A and B) to level 2 (at OPC C), to level 1 before no longer being detected. At the furthest extent of the plume the center was only intensity level 2 with an outside edge of level 1.

5.4.4 Combined drone image and ground concentrations

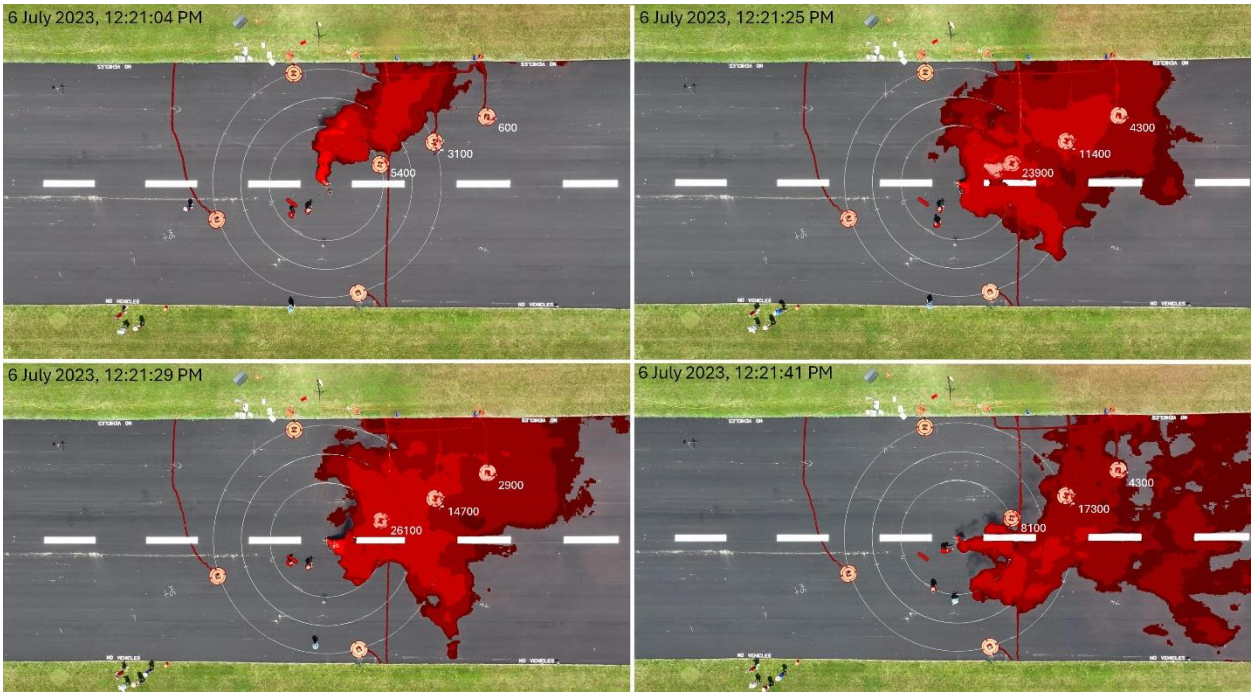

Figure 8. 4 panels of processed smoke images as seen from above along with the associated optical particle counter concentration measurements (cm^{-3}). In the top left panel, the edge of the smoke plume intersected with OPCs A and B. In the top right and bottom left panel, the smoke plume engulfed all 3 OPCs with higher intensity levels on OPCs A and B. In the bottom right panel, the plume drifted away from OPC A. As the plume ascended, OPC B was fully covered, and OPC C was partially covered.

The drone video was processed to show smoke intensity levels from a top-down view, which was matched with spikes in OPC concentrations measured on the ground (**Figure 8**). Intensity levels were determined by reading RGB pixel intensity at each ground sensor location and matching the determined intensity level with OPC concentrations during release period 2. For each intensity level the average particle concentration as measured by all OPC sensors was calculated. The five intensity levels were associated with specific average particle concentrations:

Intensity level 0 – 1012 cm^{-3}

Intensity level 1 – 4024 cm^{-3}

Intensity level 2 – 8026 cm^{-3}

Intensity level 3 – 12311 cm^{-3}

Intensity level 4 – 17956 cm^{-3}

There were periods when the OPCs recorded higher particle concentrations, but the video processing would not identify the plume as being over the OPC. This indicates that, while the video can broadly track the smoke plume, it struggles to detect lower concentrations at the edges. When attempting to utilize the plume intensity code on images taken from the side of the plume the smoke was not accurately identified and labeled. This leads to the video analysis using RGB to struggle to determine the height of the plume as it can only track the two-dimensional horizontal movement of the smoke.

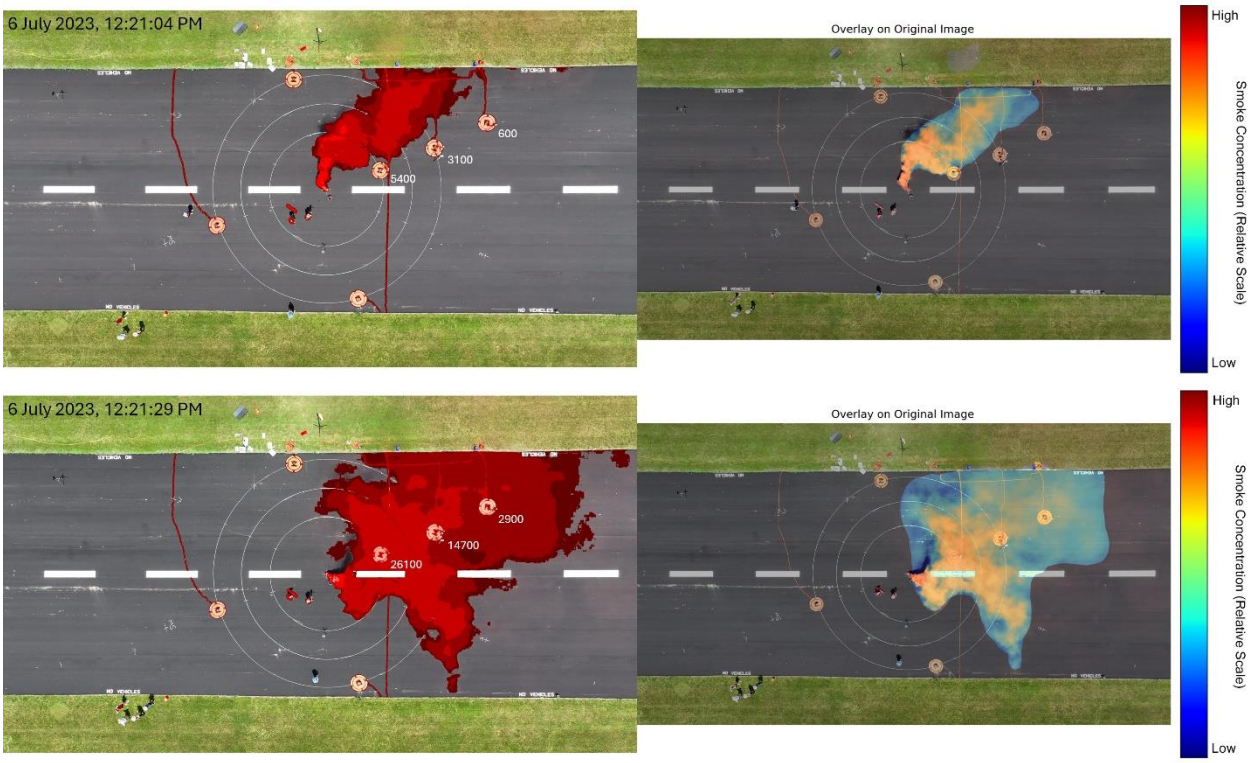

Figure 9. 2 sets of processed smoke images as seen from above along with the associated optical particle counter concentration measurements (cm^{-3}) overlaid on the left image. In the top left and bottom left the smoke plume was divided into smoke intensity bins based on the relative red intensity of the RGB readout of each pixel. In the top right and bottom right panel, the smoke plume was measured by average saturation and the value of each measured pixel was displayed as a continuous color gradient.

Utilizing the same images processed for red color intensity we can also process for saturation and value of pixels within the detected plume area. When we mapped the average saturation and value channels to the smoke plume, we were able to detect higher resolution plume density than was visible with just the red value smoke intensity levels (**Figure 9**). Mapping the saturation and value was also possible for side view imagery of the smoke plume (**Figure 10**) showing how the plume behaves both horizontally and vertically.

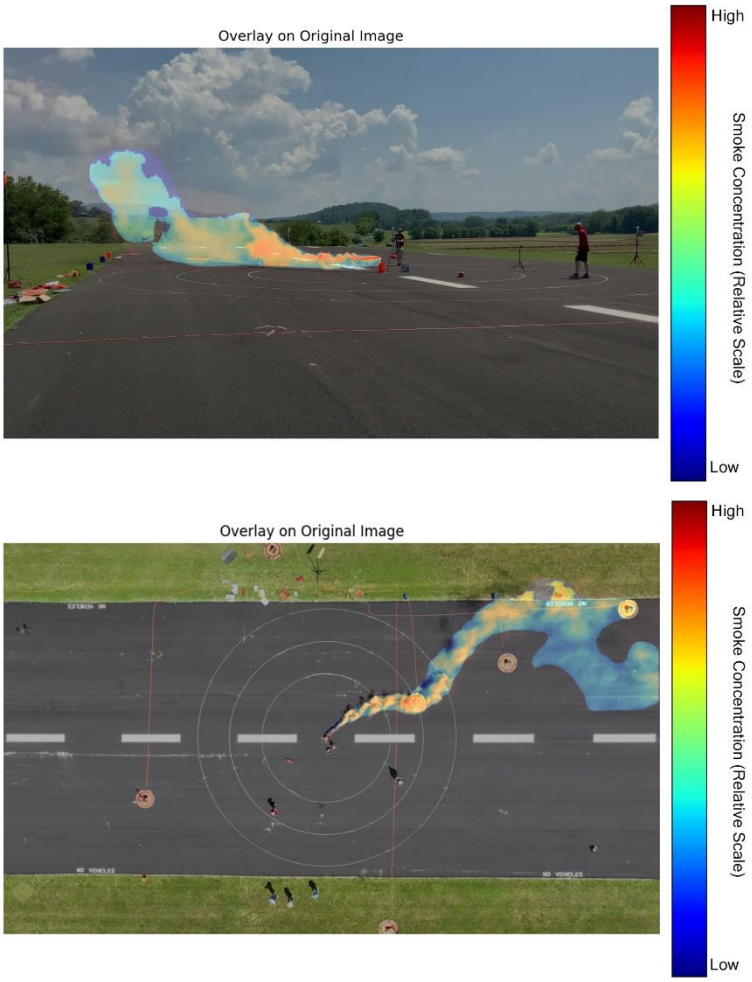

Figure 10. The processed side (top) and top-down (bottom) view of the smoke plume. Processed images had the plume identified via a trained Detectron2 AI and the plume density was color mapped using the averaged saturation and value read at each pixel within the plume.

5.4.5 Image-based predictive model for concentration

Using JMP 16 software we were able to train a neural network model to predict particle concentrations at a single ground OPC (OPC B) from the color intensity measured by the RGB smoke intensity processed drone imagery. The five model predicted concentrations are shown below:

Intensity level 0 – 1143 cm^{-3}

Intensity level 1 – 4323 cm^{-3}

Intensity level 2 – 8235 cm^{-3}

Intensity level 3 – 12042 cm^{-3}

Intensity level 4 – 16144 cm^{-3}

These results had an R-Squared value of 0.612 for the training data and 0.559 for the validation data (**Figure 11**).

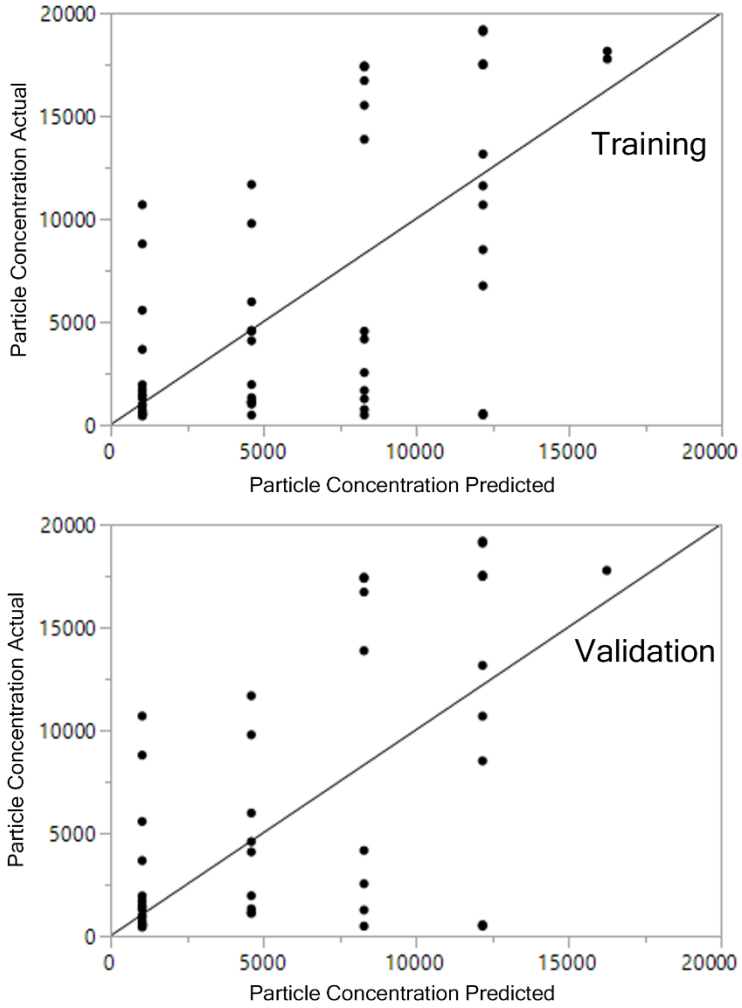

Figure 11. The training and validation predicted vs actual plots for the particle concentrations measured by the OPC and predicted by the neural model trained with smoke intensity data. These results had an R-Squared value of 0.612 for the training data and 0.559 for the validation data.

A model using ground OPC (OPC B) data to predict the smoke intensity level (as determined by RGB image processing) was more accurate with an R-Squared of 0.661 for the training data and 0.764 on the validation data. The neural model was accurately able to sort 239 of 314 training samples and 119 of 158 validation data points. (**Table 2**).

Training Data

Actual	Predicted Count				
Intensity Level	**0**	**1**	**2**	**3**	**4**
0	188	7	0	5	0
1	19	13	0	5	0
2	12	8	9	3	0
3	11	0	0	29	0
4	0	0	0	5	0

Validation Data

Actual	Predicted Count				
Intensity Level	**0**	**1**	**2**	**3**	**4**
0	96	1	0	3	0
1	9	7	0	3	0
2	4	4	7	1	0
3	1	0	0	19	0
4	0	0	0	3	0

Table 2. Training and validation data for the model predicting smoke intensity level using particle concentrations as inputs.

JMP 16 software was used to train a neural model to create a prediction equation to determine particle concentration by utilizing top-down imagery and reading the averaged saturation and value of pixels near to the ground sensor OPC A during one release period. The empirical prediction equation produced a model that had an R-Squared of 0.532 and a validation prediction R-Squared value of 0.382 (**Figure 12**). The hidden node equations and prediction equation are as follows:

$$H_1 = \tanh(1.443 - 1.020SV) \quad (1)$$

$$H_2 = \tanh(10.296 - 12.471SV) \quad (2)$$

$$H_3 = \tanh(-1.785 + 4.507SV) \quad (3)$$

$$Theta = 754855.512 + 777687.745H_1 - 1349246.363H_2 + 86676.265H_3 \quad (4)$$

Where H_1, H_2, and H_3 are the hidden node equations and Theta is the prediction equation giving particle concentration in cm^{-3} as the output. Tanh is the hyperbolic tangent function, SV is the measured average saturation and value read from top-view images at the location closest to the OPC that could be measured accurately.

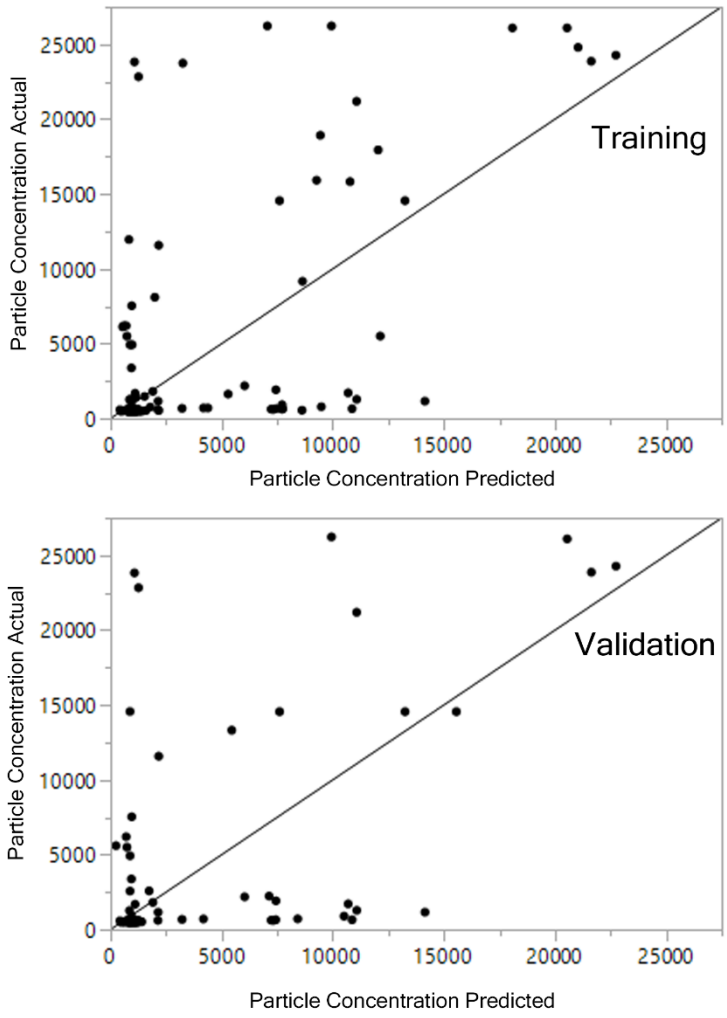

Figure 12. The training and validation predicted vs actual plots for the particle concentrations measured by the OPC and predicted by the neural model trained with the averaged saturation and value measurements of pixel readings taken near the OPC as seen by the drone video. The empirical prediction equation produced a model that had an R-Squared of 0.532 and a validation prediction R-Squared value of 0.382

5.5 Discussion

Aerosol tracking plays a pivotal role in understanding the complex dynamics of airborne particles and their impacts on environmental and human health (Cheng et al., 2007; Esfahlani, 2019). Tracking aerosols enables researchers to quantify their spatial distributions, identify emission sources, and assess their transport pathways (González-Rocha et al., 2022). By understanding aerosol behavior, scientists can develop targeted mitigation strategies to reduce exposure risks and mitigate the adverse effects of aerosol-induced pollution on ecosystems and public health (Fleming et al., 2005a; Zhao et al., 2012). We used a combination of ground-based and drone-based sensing to measure smoke plume intensity. Our study showcases the strengths and weaknesses of multiple aerosol tracking devices and provides a novel way to determine smoke concentration using only video or images of the smoke plume.

Ground sensors showed a range of particles from 400-500 cm^{-3} to 27000 cm^{-3}, with distance from the smoke source being the greatest predictor of highest peak smoke intensity. Measurements taken inside the plume were done with OPCs and high-volume filter samplers, which is consistent with smoke measurements done in studies like Wang et al. (Wang et al., 2020) and Zhang et al. (Zhang et al., 2017). Our results showed that OPCs can consistently with each other measure both high and low particle concentrations, even under varying weather conditions. When sensors are arrayed around the particle source, measurements reveal which criteria produce higher or lower particle concentrations, allowing for predictions of particle movement in the sampled area (Prank et al., 2013; Hecker et al., 2022). There was a similar percentage of particles measured above background levels at the close and far OPC (14.3% and 13.4%) the highest concentrations (above 20000 cm^{-3}) occurred more than 2.5 times as often at the closest OPC when compared to the farthest OPC,

having 4.4% and 1.7% of the time spent in the highest concentration of the plume. This is consistent with the greater spreading of the smoke plume and the exposure time of the sensors(Ho and Kuo, 2009; Mommert et al., 2020). We observed concentrations ranging from 400 cm^{-3} to beyond the sensor maximum of 27000 cm^{-3}.

A decreasing concentration of collected smoke was observed with the high-volume filter sampling as the distance from the source was increased. We utilized high-volume samplers to see the effect of distance and smoke exposure time over the entire smoke release period. We observed higher levels of absorbance from samples collected from samplers closer to the source and from those with more exposure time to the plume. High-volume air filter samplers are useful for supplementing measurements and detecting lower concentrations that may be missed by OPCs (Sang-Nourpour and Olfert, 2019). While high-volume samplers lack the temporal resolution of OPCs, they provide an average over a longer period, showing which areas received the most aerosol exposure on average more precisely than averaging OPC measurements. High-volume filter samplers can collect a much larger parcel of air than OPCs and can potentially detect lower concentrations of exposure that OPCs might miss (Marple et al., 1990; Enamorado-Báez et al., 2015). These samplers are best utilized when looking for low concentrations of aerosols, where the specific timing and movement of particles are less important.

Drone mounted OPC results showed high sensitivity to in and out of plume measurements, with particle concentrations jumping as soon as the drone moved into the plume, going from levels as low as 400 cm^{-3} to as high as 3334 cm^{-3} in only one second, and reaching a peak of 17000 cm^{-3}

within 10 seconds. OPCs are excellent for capturing aerosol plume movement with second-to-second accuracy (Crilley et al., 2020; He et al., 2020). By matching drone OPC measurements with the OPC on the ground we can see the difference in plume density at different altitudes downwind from the smoke emission source. In most cases we saw lower concentrations measured by the drone than by the ground OPCs. During the second release period the drone had an average concentration reading of only 513 cm^{-3} while the ground sensor below averaged 1741 cm^{-3}. The drone was observed often as being at the edge of the plume, which would be less concentrated than the ground sensors which would occasionally be in the center of the plume. Only having one drone operator limited our ability to take drone video and drone OPC data simultaneously. As such, the drone concentrations cannot be matched with smoke intensity levels determined by the drone video.

Drone video collected from above the smoke source was able to be processed to reliably track smoke movement and intensity with 5 different intensity levels. The red ratio of pixels from the RGB color space in images extracted from the drone video was chosen to be used as the smoke release was performed using a red smoke emitter. We were able to track the movement of the plume over time and identify areas exposed to higher and lower concentrations at any given moment. Smoke intensity was sorted into bins with intensity level 0 at 1143 cm^{-3}, intensity level 1 at 4323 cm^{-3}, intensity level 2 at 8235 cm^{-3}, intensity level 3 at 12042 cm^{-3}, and intensity level 4 at 16144 cm^{-3}. Smoke tracking through video has been used for wildfires and industrial pollutants, but matching these results with other sensors is less well described (Mommert et al., 2020; Rahman et al., 2021; Chen et al., 2022; McClure et al., 2023). We found that video tracking from directly above could not determine the height of the smoke plume, leading to

inconsistencies between ground sensors and video analysis. Previous studies have shown that resolving three-dimensional smoke plumes is challenging, especially when background conditions are not uniform, which can cause the tracking to miss plume movement through differently colored areas (Zhao et al., 2012; Gagliardi and Saponara, 2020; Gupta et al., 2021). Although we successfully created a smoke tracking program for the release runway where experiments were conducted, the smoke could not be tracked across the grass beyond the sampling area for the RGB smoke intensity levels. This limitation restricts our implementation of visual smoke tracking to areas with more consistent terrain and aerosols that can be visually distinguished from the background using this method. However, the HSV tracking was able to track the aerosol over the grass as well as different backgrounds seen from the side view. When utilizing the RGB color model to track the smoke plumes our restriction of top-down drone video only allowed the ability to analyze the smoke plume in a method limited to treating the 30-meter space between the release point and our drone as a 2-dimensional space. This simplified way of observing the plume will treat plumes of greater height the same as plumes of greater density. Therefore our visual smoke tracking implementation is most effective when the aerosol is clearly visible, relatively flat along the horizontal plane, and horizontal movement needs to be measured (Ho and Kuo, 2009; Zhao et al., 2012; Zhou et al., 2016). By utilizing drone and ground imagery processed to determine plume density using saturation and value within the trained AI plume detection we were able to track smoke density continuously from above and beside the smoke plume (**Figure 10**). This is the first step in creating a three-dimensional model of the plume movement and could be utilized to help understand smoke or invisible aerosol movement.

Drone video data was combined with OPC concentrations to match the smoke intensity levels with particle concentrations at specific times. A single pixel was used to match as closely to the position of the OPC as possible to read conditions the OPC would experience, and one OPC was used for each model to reduce the effects distance from the plume source may have had on the measured conditions of the plume. Utilizing the combined data, a neural model was created in JMP 16 software which is capable of predicting smoke concentrations from the video intensity and is capable of predicting the smoke intensity from the reported smoke concentrations. Using the RGB intensity levels, the model is only able to predict a set concentration for each intensity level giving an R-Squared value of 0.612 for the training data and 0.559 for the validation data. However, this prediction value is similar to the average particle concentration measured at each intensity level and does not provide much extra utility. Since this model only predicts one value for each intensity level it is of limited use for giving as single estimate of particle concentrations for each intensity level and suffers from high levels of variance at the higher levels of concentration, in some cases seeing differences in the real and predicted values of more than 10000 cm^{-3}. This technique is novel as well as informative as it provides a way to determine the particle concentrations without needing to measure in the plume (Mommert et al., 2020; Mtz-Enriquez et al., 2020). A finer resolution of concentrations is preferred, but with only 5 input levels the model is only capable of producing 5 output levels of concentration. However, this data can be utilized more effectively to train a model to predict smoke intensity level from the measured particle counts using JMP 16 software. The neural model was capable of sorting 76% of training samples and 75% validation data points correctly into different smoke intensity levels. This shows the intensity bins are correlated with the smoke concentrations and one can create predictions in both directions with the collected data. To address the lack of resolution in the RGB color to particle concentration

model, another model was made using the averaged saturation and value recorded from pixels near to OPC A in the drone video. By utilizing the averaged S and V components of the pixel values this allowed for a continuous scale from 0 to 1 to map to the particle concentrations. The continuous scale allows for more precise predictions of particle concentrations in the air than the 5 levels provided by the bin model and has an R-Squared value of 0.532 for the training data set and 0.382 for the validation training data set. While the HSV model gave a lower fit than the RGB intensity model the HSV model gives values continuously as an output which may make it better to define higher resolution scales of plume shape and density. Both the RGB and HSV models were unable to address the plume height vs density problem created by a lack of adequate 3-dimensional tracking of the plume movement due to the sole data source being the top-down drone video. Despite this inadequacy both models provide potential for the tracking of plume movement when combined with other sensing equipment.

Validated OPC sensing methods are necessary alongside video tracking of visual aerosols and as standalone tools for tracking invisible aerosols. Additional work is required to better understand how to integrate these sensing systems for aerosol tracking (Wei et al., 2009; Vaidyanathan et al., 2018). Current aerosol tracking methods, such as wildfire smoke tracking, utilize particle sensors and visual smoke detection, but are mostly focused on large-scale or long-distance measurements (Krüll et al., 2012; Gupta et al., 2021). The potential of video particle tracking of not just the plume size and shape, but also density is not fully explored and could be crucial for understanding the movement of aerosol plumes above traditional sensing regions (Esfahlani, 2019; Chen et al., 2021; Rahman et al., 2021). Our study examines a controlled smoke release on a smaller scale, demonstrating that OPCs can be used on the ground or mounted on drones to train a model which

can accurately track aerosol plumes with high temporal and spatial resolution. Future studies should include flying a drone-based sensor alongside a top-down video to determine the plume height, which cannot be determined accurately with just the top-down video. By combining the 2 drone sampling approach with an array of ground cameras the smoke plume dimensions, intensity, and concentration could be tracked in 3 dimensions and through time as the plume dispersed. This approach would also help elucidate the vertical movement of the plume, providing better insights into the plume's path under different weather conditions.

5.6 Author contributions

LB designed and conducted field experiments for the Kentland smoke release. RH coordinated the use of high-volume samplers during the experiments at Kentland. HF, SR, assisted with ground level data collection during the sampling experiment. DS was the pilot in command and performed all drone-based operations for the experiments. LB analyzed OPC, Ed, and RGB drone video data collected from the experiments. NJ and MN analyzed HSV drone and ground video data collected from the experiments. LB and DS led the writing of the manuscript. All authors provided feedback on the manuscript.

5.7 Conflicts of interest

There are no conflicts of interest to declare.

Chapter 6. Conclusions and Future Directions

This research has shown that levels of HAB-associated particles can be quantified and predicted using a combination of sensing and modeling techniques. Weather impacts the rate of aerosolized particles produced, and the location those particles will ultimately be transported. Microorganisms collected from the water and the air displayed morphological similarities indicating the source of the organisms in the air to likely be from the HAB experiencing lake. Using lightweight and relatively cheap OPCs, particle counts were accurately measured in an effort to predict HAB aerosol levels. There was a strong correlation between weather effects and measured particle counts which allowed for the prediction of HAB aerosol levels with weather forecasts. With a large amount of beach condition data collected across a wide geographic area, HAB aerosol effects on beach goers can be predicted and potential exposure warnings can be recommended. Drone mounted sensors tested here as a way to collect particle data for HABs can also be utilized in other applications such as the tracking of pollen, smoke, pathogens, or other particles that only have part of the information gathered from ground sensing. The ability of drones to take measurements at different altitudes highlights the differences between what is measured at ground level and what is occurring above (González-Rocha et al., 2020), and these differences can have influences on the long-distance transport of aerosols.

In the future, sampling could be done at more lakes and beaches that experience recurring HABs. By utilizing cost-effective OPC and weather stations the sampling area could be constantly monitored for indications of HAB aerosol activity. Our sampling was limited to three lakes and two ocean beaches. Collection of air and water samples along with weather and particle count data could be used to create a local model to predict conditions which would cause higher levels of HAB aerosols. Larger data sets, like the Mote Beach Conditions Reporting System (BCRS) which

includes thousands of observations across more than 75 beaches, could be combined with collected weather and particle count data to make more robust prediction models for HAB exposure. Eventually, with enough collected data from lakes and beaches a general prediction model could be created to determine HAB aerosol likelihood at any known HAB site.

HAB tracking and mitigation are important to people and there is a willingness to pay for these services (Moeltner et al., 2022). By offering low cost OPCs and weather sensors which can be mounted permanently or temporarily in an at-risk area, people will be safer and more likely to enjoy these beach and lake spaces at times when toxin exposure risk is low. Current HAB reports are rarely predictive, and many may not even know to look for the signs of a HAB if there is not adequate reporting (Smith et al., 2014). With better sensing techniques and predictive capabilities, we will be able to determine high and low risk areas of HAB aerosol exposure at individual beach or county level. With better predictive capability, affected people will have access to information regarding health risks associated with their homes or recreation areas. By increasing knowledge and awareness about HABs people can be motivated to avoid more dangerous areas and potentially change habits that lead to increased instances of HAB occurrence (Hathaway et al., 2012).

Drone-based sensors are not limited to external sensing devices attached to the drone. We show that drone cameras can be utilized to track visible aerosol plumes. With future work tracking plumes via combining data collected from drone cameras and ground-based cameras a 3 dimensional model of plume movement is possible (Krüll et al., 2012; Gupta et al., 2021). By better understanding the visual plume movement and corresponding measurements from ground and drone-based OPC data plumes of non-visible particles could also be tracked using a combination of ground and drone sensors in an array around suspected plume sources. By matching the OPC data from multiple sensors with the known plume intensity levels, we could

create a map of plume movement without being able to visually identify the plume. This could be particularly useful over larger areas to determine where potentially dangerous plumes of aerosols are transported and what areas will be most impacted (Kirkpatrick et al., 2010).

Targeting sensor placement to HAB likely water bodies could be done through satellite imagery detection and bloom prediction models (Ahn and Shanmugam, 2006; Glibert et al., 2010). Watershed characteristics can be used to model HAB likelihood for different lake systems (Weber et al., 2020). Models can be checked against known HAB sites and may help determine at risk HAB locations. Better HAB targeting with the use of lightweight and cost-effective sensors mounted on drones or permanently on shore would provide invaluable data about the fluctuations of HAB aerosol production and transport. A HAB lake prediction model would also allow for the prevention of new HABs by providing insight into what development changes would best mitigate HAB formation in at-risk lakes. Measures could be taken to prevent a lake from becoming a HAB site that would occur without action due to climate change induced land use fluctuations (Bethke and Nudds, 1995; Álvarez et al., 2017).

The questions of each objective outlined in the introduction to this document were addressed by the research conducted in each of the main chapters outlining work that has been published or in in progress towards publication as scientific literature. These chapters work towards the overall goal of characterizing the influence of weather phenomenon such as wind speed, wind direction, and temperature on measured aerosol levels above and around HABs. This was done by taking measurements using ground and drone mounted sensors along with water and air sampling techniques. Objective one, looking to explore associations between measured weather conditions and the particle counts measured above and beside active HABs and HAB sites found relationships between weather and particle concentrations that were able to be predicted with statistical neural

modeling. Objective two, looking to create a model to predict concentrations of particles associated with HABs in the air at downwind sites was able to successfully predict particle concentrations on the shore of both lake and ocean HAB events. Objective three, looking to create a model to predict what location will have high levels of HAB aerosols found beach level HAB intensity forecasting was possible using current conditions along with future weather forecasts. Objective four, looking to combine visual smoke tracking with weather and particle measurements to improve particle behavior predictions found that aerosol plumes could be track visually through drone and ground cameras alongside traditional air quality sensors to improve tracking capabilities of aerosol plumes both visible and invisible. Overall this work ties together weather and particle concentrations associated with HABs helping to define the ways weather influences HAB aerosols.

Bibliography

A primer on Gulf of Mexico harmful algal blooms by Mote Marine Laboratory and Aquarium - Issuu (2014). Available at: https://issuu.com/motemarinelab/docs/habprimer_10_16_2013_4web (Accessed June 17, 2024).

AAAAI (2021). Available at: https://pollen.aaaai.org/#/ (Accessed July 19, 2024).

Affine Point Processes and Portfolio Credit Risk | SIAM Journal on Financial Mathematics (n.d.). Available at: https://epubs.siam.org/doi/abs/10.1137/090771272 (Accessed June 17, 2024).

Ahn, Y.-H., and Shanmugam, P. (2006). Detecting the red tide algal blooms from satellite ocean color observations in optically complex Northeast-Asia Coastal waters. *Remote Sens. Environ.* 103, 419–437. doi: 10.1016/j.rse.2006.04.007

Ai, H., Zhang, K., Sun, J., and Zhang, H. (2023). Short-term Lake Erie algal bloom prediction by classification and regression models. *Water Res.* 232, 119710. doi: 10.1016/j.watres.2023.119710

Alcock, F. (2007). An assessment of Florida red tide: causes, consequences and management strategies. Marine Policy Institute, Mote Marine Laboratory, Sarasota, FL. Available at: https://dspace.mote.org:8443/xmlui/handle/2075/2911 (Accessed July 18, 2024).

Álvarez, X., Valero, E., Santos, R. M. B., Varandas, S. G. P., Sanches Fernandes, L. F., and Pacheco, F. A. L. (2017). Anthropogenic nutrients and eutrophication in multiple land use watersheds: Best management practices and policies for the protection of water resources. *Land Use Policy* 69, 1–11. doi: 10.1016/j.landusepol.2017.08.028

Anderson, D. M., Glibert, P. M., and Burkholder, J. M. (2002). Harmful algal blooms and eutrophication: Nutrient sources, composition, and consequences. *Estuaries* 25, 704–726. doi: 10.1007/BF02804901

Backer, L. C., Fleming, L. E., Rowan, A., Cheng, Y.-S., Benson, J., Pierce, R. H., et al. (2003). Recreational exposure to aerosolized brevetoxins during Florida red tide events. *Harmful Algae* 2, 19–28. doi: 10.1016/S1568-9883(03)00005-2

Backer, L. C., Kirkpatrick, B., Fleming, L. E., Cheng, Y. S., Pierce, R., Bean, J. A., et al. (2005). Occupational exposure to aerosolized brevetoxins during Florida red tide events: Effects on a healthy worker population. *Environ. Health Perspect.* 113, 644–649. doi: 10.1289/ehp.7502

Backer, L. C., Manassaram-Baptiste, D., LePrell, R., and Bolton, B. (2015). Cyanobacteria and algae blooms: Review of health and environmental data from the Harmful Algal Bloom-Related Illness Surveillance System (HABISS) 2007–2011. *Toxins* 7, 1048–1064. doi: 10.3390/toxins7041048

Bacry, E., Delattre, S., Hoffmann, M., and Muzy, J. F. (2013). Modelling microstructure noise with mutually exciting point processes. *Quant. Finance* 13, 65–77. doi: 10.1080/14697688.2011.647054

Bansod, B., Singh, R., Thakur, R., and Singhal, G. (2017). A comparision between satellite based and drone based remote sensing technology to achieve sustainable development: a review. *J. Agric. Environ. Int. Dev. JAEID* 111, 383–407. doi: 10.12895/jaeid.20172.690

Belyaev, S. P., and Levin, L. M. (1974). Techniques for collection of representative aerosol samples. *J. Aerosol Sci.* 5, 325–338. doi: 10.1016/0021-8502(74)90130-X

Bertani, I., Obenour, D. R., Steger, C. E., Stow, C. A., Gronewold, A. D., and Scavia, D. (2016). Probabilistically assessing the role of nutrient loading in harmful algal bloom formation in western Lake Erie. *J. Gt. Lakes Res.* 42, 1184–1192. doi: 10.1016/j.jglr.2016.04.002

Bethke, R. W., and Nudds, T. D. (1995). Effects of Climate Change and Land Use on Duck Abundance in Canadian Prairie-Parklands. *Ecol. Appl.* 5, 588–600. doi: 10.2307/1941969

Bieber, P., Seifried, T. M., Burkart, J., Gratzl, J., Kasper-Giebl, A., Schmale, D. G., et al. (2020). A drone-based bioaerosol sampling system to monitor ice nucleation particles in the lower atmosphere. *Remote Sens.* 12, 552. doi: 10.3390/rs12030552

Bilyeu, L., Bloomfield, B., Hanlon, R., González-Rocha, J., J. Jacquemin, S., P. Ault, A., et al. (2022). Drone-based particle monitoring above two harmful algal blooms (HABs) in the USA. *Environ. Sci. Atmospheres* 2, 1351–1363. doi: 10.1039/D2EA00055E

Birbeck, J. A., Peraino, N. J., O'Neill, G. M., Coady, J., and Westrick, J. A. (2019a). Dhb microcystins discovered in USA using an online concentration LC–MS/MS platform. *Toxins* 11, 653. doi: 10.3390/toxins11110653

Birbeck, J. A., Westrick, J. A., O'Neill, G. M., Spies, B., and Szlag, D. C. (2019b). Comparative analysis of microcystin prevalence in Michigan lakes by online concentration LC/MS/MS and ELISA. *Toxins* 11, 13. doi: 10.3390/toxins11010013

Bishop, J. K. B., Lam, P. J., and Wood, T. J. (2012). Getting good particles: Accurate sampling of particles by large volume in-situ filtration. *Limnol. Oceanogr. Methods* 10, 681–710. doi: 10.4319/lom.2012.10.681

Boyer, G. L. (2008). "Cyanobacterial toxins in New York and the lower Great Lakes ecosystems," in *Cyanobacterial Harmful Algal Blooms: State of the Science and Research Needs*, ed. H. K. Hudnell (New York, NY: Springer), 153–165. doi: 10.1007/978-0-387-75865-7_7

Brittain, S. M., Wang, J., Babcock-Jackson, L., Carmichael, W. W., Rinehart, K. L., and Culver, D. A. (2000). Isolation and characterization of microcystins, cyclic heptapeptide hepatotoxins from a Lake Erie strain of Microcystis aeruginosa. *J. Gt. Lakes Res.* 26, 241–249. doi: 10.1016/S0380-1330(00)70690-3

Brunton, S. L., and Kutz, J. N. (2019). *Data-driven science and engineering: Machine learning, dynamical systems, and control*. Cambridge University Press.

Bulot, F. M. J., Johnston, S. J., Basford, P. J., Easton, N. H. C., Apetroaie-Cristea, M., Foster, G. L., et al. (2019). Long-term field comparison of multiple low-cost particulate matter sensors in an outdoor urban environment. *Sci. Rep.* 9, 7497. doi: 10.1038/s41598-019-43716-3

Carmichael, W. W., and Boyer, G. L. (2016). Health impacts from cyanobacteria harmful algae blooms: Implications for the North American Great Lakes. *Harmful Algae* 54, 194–212. doi: 10.1016/j.hal.2016.02.002

Chen, M., and Chen, C. (2020). Optimize Neural Network Algorithm of Missing Value Imputation for Clustering Chocolate Product Type Following “STEAMS” Methodology. *CATA* 69, 230–241.

Chen, S., Cao, Y., Feng, X., and Lu, X. (2021). Global2Salient: Self-adaptive feature aggregation for remote sensing smoke detection. *Neurocomputing* 466, 202–220. doi: 10.1016/j.neucom.2021.09.026

Chen, X., and Huang, J. (2019). Design and Performance Evaluation of a Particle Filter-based Algorithm for Smoke Plume Path Tracking., in *2019 IEEE 4th International Conference on Advanced Robotics and Mechatronics (ICARM)*, 156–161. doi: 10.1109/ICARM.2019.8834337

Chen, Y., Hantson, S., Andela, N., Coffield, S. R., Graff, C. A., Morton, D. C., et al. (2022). California wildfire spread derived using VIIRS satellite observations and an object-based tracking system. *Sci. Data* 9, 249. doi: 10.1038/s41597-022-01343-0

Cheng, Y. S., Yue, Z., Irvin, C. M., Kirkpatrick, B., and Backer, L. C. (2007). Characterization of aerosols containing microcystin. *Mar. Drugs* 5, 136–150. doi: 10.3390/md504136

Clarke, A. D., Owens, S. R., and Zhou, J. (2006). An ultrafine sea-salt flux from breaking waves: Implications for cloud condensation nuclei in the remote marine atmosphere. *J. Geophys. Res. Atmospheres* 111. doi: 10.1029/2005JD006565

Crilley, L. R., Singh, A., Kramer, L. J., Shaw, M. D., Alam, M. S., Apte, J. S., et al. (2020). Effect of aerosol composition on the performance of low-cost optical particle counter correction factors. *Atmospheric Meas. Tech.* 13, 1181–1193. doi: 10.5194/amt-13-1181-2020

Cunliffe, M., Engel, A., Frka, S., Gašparović, B., Guitart, C., Murrell, J. C., et al. (2013). Sea surface microlayers: A unified physicochemical and biological perspective of the air–ocean interface. *Prog. Oceanogr.* 109, 104–116. doi: 10.1016/j.pocean.2012.08.004

Currier, R. D., Boyes, C., Hails, A., Nierenberg, K., Kirkpatrick, B., and Kirkpatrick, G. (2009). An ocean observing system for harmful algal bloom detection and tracking., in *OCEANS 2009*, 1–4. doi: 10.23919/OCEANS.2009.5422308

de Boisblanc, I., Dodbele, N., Kussmann, L., Mukherji, R., Chestnut, D., Phelps, S., et al. (2014). Designing a hexacopter for the collection of atmospheric flow data., in *2014 Systems and Information Engineering Design Symposium (SIEDS)*, 147–152. doi: 10.1109/SIEDS.2014.6829915

de Leeuw, G., Andreas, E. L., Anguelova, M. D., Fairall, C. W., Lewis, E. R., O’Dowd, C., et al. (2011). Production flux of sea spray aerosol. *Rev. Geophys.* 49. doi: 10.1029/2010RG000349

Deane, G. B., and Stokes, M. D. (2002). Scale dependence of bubble creation mechanisms in breaking waves. *Nature* 418, 839–844. doi: 10.1038/nature00967

Dees, P., Bresnan, E., Dale, A. C., Edwards, M., Johns, D., Mouat, B., et al. (2017). Harmful algal blooms in the eastern north Atlantic Ocean. *Proc. Natl. Acad. Sci.* 114, E9763–E9764. doi: 10.1073/pnas.1715499114

Deng, J., Paerl, H. W., Qin, B., Zhang, Y., Zhu, G., Jeppesen, E., et al. (2018). Climatically-modulated decline in wind speed may strongly affect eutrophication in shallow lakes. *Sci. Total Environ.* 645, 1361–1370. doi: 10.1016/j.scitotenv.2018.07.208

Dubey, R., Patra, A. K., Joshi, J., Blankenberg, D., Kolluru, S. S. R., Madhu, B., et al. (2022). Evaluation of low-cost particulate matter sensors OPC N2 and PM Nova for aerosol monitoring. *Atmospheric Pollut. Res.* 13, 101335. doi: 10.1016/j.apr.2022.101335

Dueker, M. E., O'Mullan, G. D., Martínez, J. M., Juhl, A. R., and Weathers, K. C. (2017). Onshore wind speed modulates microbial aerosols along an urban waterfront. *Atmosphere* 8, 215. doi: 10.3390/atmos8110215

Enamorado-Báez, S. M., Gómez-Guzmán, J. M., Chamizo, E., and Abril, J. M. (2015). Levels of 25 trace elements in high-volume air filter samples from Seville (2001–2002): Sources, enrichment factors and temporal variations. *Atmospheric Res.* 155, 118–129. doi: 10.1016/j.atmosres.2014.12.005

Esfahlani, S. S. (2019). Mixed reality and remote sensing application of unmanned aerial vehicle in fire and smoke detection. *J. Ind. Inf. Integr.* 15, 42–49. doi: 10.1016/j.jii.2019.04.006

facebookresearch/detectron2 (2024). Available at: https://github.com/facebookresearch/detectron2 (Accessed July 29, 2024).

Fang, S., Del Giudice, D., Scavia, D., Binding, C. E., Bridgeman, T. B., Chaffin, J. D., et al. (2019). A space-time geostatistical model for probabilistic estimation of harmful algal bloom biomass and areal extent. *Sci. Total Environ.* 695, 133776. doi: 10.1016/j.scitotenv.2019.133776

Feng, L., Yang, T., Wang, D., Wang, Z., Pan, Y., Matsui, I., et al. (2020). Identify the contribution of elevated industrial plume to ground air quality by optical and machine learning methods. *Environ. Res. Commun.* 2, 021005. doi: 10.1088/2515-7620/ab7634

Filippi, M., Hanlon, R., Rypina, I. I., Hodges, B. A., Peacock, T., and Schmale, D. G. (2021). Tracking a surrogate hazardous agent (rhodamine dye) in a coastal ocean environment using in situ measurements and concentration estimates derived from drone images. *Remote Sens.* 13, 4415. doi: 10.3390/rs13214415

Fleming, L. E., Backer, L. C., and Baden, D. G. (2005a). Overview of aerosolized Florida red tide toxins: Exposures and effects. *Environ. Health Perspect.* 113, 618–620. doi: 10.1289/ehp.7501

Fleming, L. E., Bean, J. A., Kirkpatrick, B., Cheng, Y. S., Pierce, R., Naar, J., et al. (2009). Exposure and effect assessment of aerosolized red tide toxins (brevetoxins) and asthma. *Environ. Health Perspect.* 117, 1095–1100. doi: 10.1289/ehp.0900673

Fleming, L. E., Kirkpatrick, B., Backer, L. C., Bean, J. A., Wanner, A., Dalpra, D., et al. (2005b). Initial evaluation of the effects of aerosolized Florida red tide toxins (brevetoxins) in persons with asthma. *Environ. Health Perspect.* 113, 650–657. doi: 10.1289/ehp.7500

Fleming, L. E., Kirkpatrick, B., Backer, L. C., Bean, J. A., Wanner, A., Reich, A., et al. (2007). Aerosolized red-tide toxins (brevetoxins) and asthma. *Chest* 131, 187–194. doi: 10.1378/chest.06-1830

Fleming, L. E., Kirkpatrick, B., Backer, L. C., Walsh, C. J., Nierenberg, K., Clark, J., et al. (2011). Review of Florida red tide and human health effects. *Harmful Algae* 10, 224–233. doi: 10.1016/j.hal.2010.08.006

Frizzi, S., Kaabi, R., Bouchouicha, M., Ginoux, J.-M., Moreau, E., and Fnaiech, F. (2016). Convolutional neural network for video fire and smoke detection., in *IECON 2016 - 42nd Annual Conference of the IEEE Industrial Electronics Society*, 877–882. doi: 10.1109/IECON.2016.7793196

Fu, F. X., Tatters, A. O., and Hutchins, D. A. (2012). Global change and the future of harmful algal blooms in the ocean. *Mar. Ecol. Prog. Ser.* 470, 207–233. doi: 10.3354/meps10047

Gagliardi, A., and Saponara, S. (2020). AdViSED: Advanced Video SmokE Detection for real-time measurements in antifire indoor and outdoor systems. *Energies* 13, 2098. doi: 10.3390/en13082098

Giordano, M. R., Malings, C., Pandis, S. N., Presto, A. A., McNeill, V. F., Westervelt, D. M., et al. (2021). From low-cost sensors to high-quality data: A summary of challenges and best practices for effectively calibrating low-cost particulate matter mass sensors. *J. Aerosol Sci.* 158, 105833. doi: 10.1016/j.jaerosci.2021.105833

Glibert, P. M., Allen, J. I., Bouwman, A. F., Brown, C. W., Flynn, K. J., Lewitus, A. J., et al. (2010). Modeling of HABs and eutrophication: Status, advances, challenges. *J. Mar. Syst.* 83, 262–275. doi: 10.1016/j.jmarsys.2010.05.004

González-Rocha, J., Bilyeu, L., D. Ross, S., Foroutan, H., J. Jacquemin, S., P. Ault, A., et al. (2023). Sensing atmospheric flows in aquatic environments using a multirotor small uncrewed aircraft system (sUAS). *Environ. Sci. Atmospheres* 3, 305–315. doi: 10.1039/D2EA00042C

González-Rocha, J., De Wekker, S. F. J., Ross, S. D., and Woolsey, C. A. (2020). Wind profiling in the lower atmosphere from wind-induced perturbations to multirotor UAS. *Sensors* 20, 1341. doi: 10.3390/s20051341

González-Rocha, J., Woolsey, C. A., Sultan, C., and De Wekker, S. F. J. (2019). Sensing wind from quadrotor motion. *J. Guid. Control Dyn.* 42, 836–852. doi: 10.2514/1.G003542

González-Rocha, Ross, and Schmale III (2022). Application of multirotor sUAS wind profiling for resolving microscale flows in complex environments. *Environ. Sci. Atmospheres* In Preparation.

Gotwalt, C. M. (2011). JMP Neural Network Methodology. *SAS Inst.*, 11.

Graham, J. L., Loftin, K. A., Meyer, M. T., and Ziegler, A. C. (2010). Cyanotoxin mixtures and taste-and-odor compounds in cyanobacterial blooms from the midwestern United States. *Environ. Sci. Technol.* 44, 7361–7368. doi: 10.1021/es1008938

Gray, P. C., Ridge, J. T., Poulin, S. K., Seymour, A. C., Schwantes, A. M., Swenson, J. J., et al. (2018). Integrating Drone Imagery into High Resolution Satellite Remote Sensing Assessments of Estuarine Environments. *Remote Sens.* 10, 1257. doi: 10.3390/rs10081257

Gupta, T., Liu, H., and Bhanu, B. (2021). Early wildfire smoke detection in videos., in *2020 25th International Conference on Pattern Recognition (ICPR)*, 8523–8530. doi: 10.1109/ICPR48806.2021.9413231

HAB Forecasts (n.d.). Available at: https://habforecast.gcoos.org/ (Accessed June 17, 2024).

Hagan, D. H., and Kroll, J. H. (2020). Assessing the accuracy of low-cost optical particle sensors using a physics-based approach. *Atmospheric Meas. Tech.* 13, 6343–6355. doi: 10.5194/amt-13-6343-2020

Hanlon, R., Jacquemin, S. J., Birbeck, J. A., Westrick, J. A., Harb, C., Gruszewski, H., et al. (2022). Drone-based water sampling and characterization of three freshwater harmful algal blooms in the United States. *Front. Remote Sens.* 3. Available at: https://www.frontiersin.org/articles/10.3389/frsen.2022.949052 (Accessed August 25, 2022).

Harb, C., and Foroutan, H. (2019). A systematic analysis of the salinity effect on air bubbles evolution: Laboratory experiments in a breaking wave analog. *J. Geophys. Res. Oceans* 124, 7355–7374. doi: 10.1029/2019JC015337

Harb, C., and Foroutan, H. (2022). Experimental development of a lake spray source function and its model implementation for Great Lakes surface emissions. *Atmospheric Chem. Phys.* 22, 11759–11779. doi: 10.5194/acp-22-11759-2022

Harb, C., Pan, J., DeVilbiss, S., Badgley, B., Marr, L. C., Schmale, D. G., et al. (2021). Increasing freshwater salinity impacts aerosolized bacteria. *Environ. Sci. Technol.* 55, 5731–5741. doi: 10.1021/acs.est.0c08558

Hardison, D. R., Holland, W. C., Currier, R. D., Kirkpatrick, B., Stumpf, R., Fanara, T., et al. (2019). HABscope: A tool for use by citizen scientists to facilitate early warning of respiratory irritation caused by toxic blooms of Karenia brevis. *PLOS ONE* 14, e0218489. doi: 10.1371/journal.pone.0218489

Hathaway, J. M., Moore, T. L. C., Burkholder, J. M., and Hunt, W. F. (2012). Temporal analysis of stormwater control measure effluent based on windows of harmful algal bloom (HAB) sensitivity: Are annual nutrient EMCs appropriate during HAB-sensitive seasons? *Ecol. Eng.* 49, 41–47. doi: 10.1016/j.ecoleng.2012.08.014

HAWKES, A. G. (1971). Spectra of some self-exciting and mutually exciting point processes. *Biometrika* 58, 83–90. doi: 10.1093/biomet/58.1.83

He, M., Kuerbanjiang, N., and Dhaniyala, S. (2020). Performance characteristics of the low-cost Plantower PMS optical sensor. *Aerosol Sci. Technol.* 54, 232–241. doi: 10.1080/02786826.2019.1696015

Hecker, J. G., He, J., Rochlin, R., Brannen, C., Teng, S., Glenn, K., et al. (2022). Measuring aerosols in the operating theatre and beyond using a real-time sensor network. *Anaesthesia* 77, 1097–1105. doi: 10.1111/anae.15842

Heim, M., Mullins, B. J., Umhauer, H., and Kasper, G. (2008). Performance evaluation of three optical particle counters with an efficient “multimodal” calibration method. *J. Aerosol Sci.* 39, 1019–1031. doi: 10.1016/j.jaerosci.2008.07.006

Ho, C.-C., and Kuo, T.-H. (2009). Real-time video-based fire smoke detection system., in *2009 IEEE/ASME International Conference on Advanced Intelligent Mechatronics*, 1845–1850. doi: 10.1109/AIM.2009.5229791

Holm, S. M., Miller, M. D., and Balmes, J. R. (2021). Health effects of wildfire smoke in children and public health tools: a narrative review. *J. Expo. Sci. Environ. Epidemiol.* 31, 1–20. doi: 10.1038/s41370-020-00267-4

Hoorman, J., Hone, T., Sudman, T., Dirksen, T., Iles, J., and Islam, K. R. (2008). Agricultural impacts on lake and stream water quality in Grand Lake St. Marys, western Ohio. *Water. Air. Soil Pollut.* 193, 309–322. doi: 10.1007/s11270-008-9692-1

Hu, J., Liu, J., Zhu, Y., Diaz-Perez, Z., Sheridan, M., Royer, H., et al. (2020a). Exposure to aerosolized algal toxins in south Florida increases short- and long-term health risk in drosophila model of aging. *Toxins* 12, 787. doi: 10.3390/toxins12120787

Inspire 2 - Product Information - DJI (n.d.). *DJI Off.* Available at: https://www.dji.com/inspire-2/info (Accessed August 25, 2022).

Jacquemin, S. J., Johnson, L. T., Dirksen, T. A., and McGlinch, G. (2018). Changes in water quality of Grand Lake St. Marys watershed following implementation of a distressed watershed rules package. *J. Environ. Qual.* 47, 113–120. doi: 10.2134/jeq2017.08.0338

Jimenez, J. L., Jayne, J. T., Shi, Q., Kolb, C. E., Worsnop, D. R., Yourshaw, I., et al. (2003). Ambient aerosol sampling using the Aerodyne Aerosol Mass Spectrometer. *J. Geophys. Res. Atmospheres* 108. doi: 10.1029/2001JD001213

Jones, B., and Sall, J. (2011). JMP statistical discovery software. *WIREs Comput. Stat.* 3, 188–194. doi: 10.1002/wics.162

Kirkpatrick, B., Currier, R., Nierenberg, K., Reich, A., Backer, L. C., Stumpf, R., et al. (2008). Florida red tide and human health: A pilot beach conditions reporting system to minimize human exposure. *Sci. Total Environ.* 402, 1–8. doi: 10.1016/j.scitotenv.2008.03.032

Kirkpatrick, B., Fleming, L. E., Backer, L. C., Bean, J. A., Tamer, R., Kirkpatrick, G., et al. (2006). Environmental exposures to Florida red tides: Effects on emergency room respiratory diagnoses admissions. *Harmful Algae* 5, 526–533. doi: 10.1016/j.hal.2005.09.004

Kirkpatrick, B., Fleming, L. E., Bean, J. A., Nierenberg, K., Backer, L. C., Cheng, Y. S., et al. (2011). Aerosolized red tide toxins (brevetoxins) and asthma: Continued health effects after 1h beach exposure. *Harmful Algae* 10, 138–143. doi: 10.1016/j.hal.2010.08.005

Kirkpatrick, B., Kohler, K., Byrne, M., Fleming, L. E., Scheller, K., Reich, A., et al. (2014). Human responses to Florida red tides: policy awareness and adherence to local fertilizer ordinances. *Sci. Total Environ.* 493, 898–909. doi: 10.1016/j.scitotenv.2014.06.083

Kirkpatrick, B., Pierce, R., Cheng, Y. S., Henry, M. S., Blum, P., Osborn, S., et al. (2010). Inland transport of aerosolized Florida red tide toxins. *Harmful Algae* 9, 186–189. doi: 10.1016/j.hal.2009.09.003

Krüll, W., Tobera, R., Willms, I., Essen, H., and von Wahl, N. (2012). Early forest fire detection and verification using optical smoke, gas and microwave sensors. *Procedia Eng.* 45, 584–594. doi: 10.1016/j.proeng.2012.08.208

Lake Anna State Park: General information (2023). Available at: https://www.dcr.virginia.gov/state-parks/lake-anna#general_information

Laub, P. J., Taimre, T., and Pollett, P. K. (2015). Hawkes Processes. doi: 10.48550/arXiv.1507.02822

Levy Zamora, M., Xiong, F., Gentner, D., Kerkez, B., Kohrman-Glaser, J., and Koehler, K. (2019). Field and laboratory evaluations of the low-cost Plantower Particulate Matter Sensor. *Environ. Sci. Technol.* 53, 838–849. doi: 10.1021/acs.est.8b05174

Li, P., Li, L., Yang, K., Zheng, T., Liu, J., and Wang, Y. (2021). Characteristics of microbial aerosol particles dispersed downwind from rural sanitation facilities: Size distribution, source tracking and exposure risk. *Environ. Res.* 195, 110798. doi: 10.1016/j.envres.2021.110798

Maguire, J., Cusack, C., Ruiz-Villarreal, M., Silke, J., McElligott, D., and Davidson, K. (2016). Applied simulations and integrated modelling for the understanding of toxic and harmful algal blooms (ASIMUTH): Integrated HAB forecast systems for Europe's Atlantic Arc. *Harmful Algae* 53, 160–166. doi: 10.1016/j.hal.2015.11.006

Maloney, T. E., and Carnes, R. A. (1966). Toxicity of a Microcystis waterbloom from and Ohio pond. 4.

Marple, V. A., Liu, B. Y. H., and Burton, R. M. (1990). High-volume Impactor for Sampling Fine and Coarse Particles. *J. Air Waste Manag. Assoc.* 40, 762–767. doi: 10.1080/10473289.1990.10466722

May, N. W., Axson, J. L., Watson, A., Pratt, K. A., and Ault, A. P. (2016). Lake spray aerosol generation: A method for producing representative particles from freshwater wave breaking. Aerosols/Laboratory Measurement/Instruments and Platforms. doi: 10.5194/amt-2016-115

May, N. W., Gunsch, M. J., Olson, N. E., Bondy, A. L., Kirpes, R. M., Bertman, S. B., et al. (2018a). Unexpected contributions of sea spray and lake spray aerosol to inland particulate matter. *Environ. Sci. Technol. Lett.* 5, 405–412. doi: 10.1021/acs.estlett.8b00254

May, N. W., Olson, N. E., Panas, M., Axson, J. L., Tirella, P. S., Kirpes, R. M., et al. (2018b). Aerosol emissions from Great Lakes harmful algal blooms. *Environ. Sci. Technol.* 52, 397–405. doi: 10.1021/acs.est.7b03609

McClure, C. D., Pavlovic, N. R., Huang, S., Chaveste, M., and Wang, N. (2023). Consistent, high-accuracy mapping of daily and sub-daily wildfire growth with satellite observations. *Int. J. Wildland Fire* 32, 694–708. doi: 10.1071/WF22048

Medina-Pérez, N. I., Dall'Osto, M., Decesari, S., Paglione, M., Moyano, E., and Berdalet, E. (2021). Aerosol toxins emitted by harmful algal blooms susceptible to complex air–sea interactions. *Environ. Sci. Technol.* 55, 468–477. doi: 10.1021/acs.est.0c05795

Meskhidze, N., Petters, M. D., Tsigaridis, K., Bates, T., O'Dowd, C., Reid, J., et al. (2013). Production mechanisms, number concentration, size distribution, chemical composition, and optical properties of sea spray aerosols. *Atmospheric Sci. Lett.* 14, 207–213. doi: 10.1002/asl2.441

Moeltner, K., Fanara, T., Foroutan, H., Hanlon, R., Lovko, V., Ross, S., et al. (2022). Harmful algal blooms and toxic air: The economic value of improved forecasts. *Mar. Resour. Econ.*, 000–000. doi: 10.1086/722598

Mohler, G. O., Short, M. B., Brantingham, P. J., Schoenberg, F. P., and Tita, G. E. (2011). Self-exciting point process modeling of crime. *J. Am. Stat. Assoc.* 106, 100–108. doi: 10.1198/jasa.2011.ap09546

Mommert, M., Sigel, M., Neuhausler, M., Scheibenreif, L., and Borth, D. (2020). Characterization of industrial smoke plumes from remote sensing data. doi: 10.48550/arXiv.2011.11344

Montero, A., Dueker, M. E., and O'Mullan, G. D. (2016). Culturable bioaerosols along an urban waterfront are primarily associated with coarse particles. *PeerJ* 4, e2827. doi: 10.7717/peerj.2827

Mote Beach Conditions Reporting System (2022). Available at: https://visitbeaches.org/map (Accessed November 13, 2022).

Mtz-Enriquez, A. I., Padmasree, K. P., Oliva, A. I., Gomez-Solis, C., Coutino-Gonzalez, E., Garcia, C. R., et al. (2020). Tailoring the detection sensitivity of graphene based flexible smoke sensors by decorating with ceramic microparticles. *Sens. Actuators B Chem.* 305, 127466. doi: 10.1016/j.snb.2019.127466

National Oceanic and Atmospheric Administration, Harmful Algal Bloom Operational Forecast System (2021). Available at: https://tidesandcurrents.noaa.gov/hab/gomx.html/ (Accessed May 19, 2021).

Nierenberg, K., Byrne, M. M., Fleming, L. E., Stephan, W., Reich, A., Backer, L. C., et al. (2010a). Florida red tide perception: Residents versus tourists. *Harmful Algae* 9, 600–606. doi: 10.1016/j.hal.2010.04.010

Nierenberg, K., Hollenbeck, J., Fleming, L. E., Stephan, W., Reich, A., Backer, L. C., et al. (2011). Frontiers in outreach and education: The Florida red tide experience. *Harmful Algae* 10, 374–380. doi: 10.1016/j.hal.2011.01.004

Nierenberg, K., Kirner, K., Hoagland, P., Ullmann, S., LeBlanc, W. G., Kirkpatrick, G., et al. (2010b). Changes in work habits of lifeguards in relation to Florida red tide. *Harmful Algae* 9, 419–425. doi: 10.1016/j.hal.2010.02.005

Nierenberg, K., Reich, A., Currier, R., Kirkpatrick, B., Backer, L. C., Stumpf, R., et al. (2009). Beaches and HABs: Successful expansion of the Florida red tide reporting system for protection of public health through community education and outreach. *Fla. J. Environ. Health*, 18–24.

Nimmala, M., Gruszewski, H., Hanlon, R., Bilyeu, L., Newton, T., Schmale III, D. G., et al. (2023). Modeling the dispersal kernel across scales: Local validation and regional insights into seasonal patterns and spatial variability., (Portland, OR). Available at: https://aaarabstracts.com/2023/view_abstract.php?pid=384 (Accessed August 13, 2024).

Nolan, P. J., Pinto, J., González-Rocha, J., Jensen, A., Vezzi, C. N., Bailey, S. C. C., et al. (2018). Coordinated Unmanned Aircraft System (UAS) and ground-based weather measurements to predict Lagrangian Coherent Structures (LCSs). *Sensors* 18, 4448. doi: 10.3390/s18124448

O'Dowd, C. D., and de Leeuw, G. (2007). Marine aerosol production: a review of the current knowledge. *Philos. Trans. R. Soc. Math. Phys. Eng. Sci.* 365, 1753–1774. doi: 10.1098/rsta.2007.2043

Ogata, Y. (1988). Statistical models for earthquake occurrences and residual analysis for point processes. *J. Am. Stat. Assoc.* 83, 9–27. doi: 10.1080/01621459.1988.10478560

Olson, N. E., Cooke, M. E., Shi, J. H., Birbeck, J. A., Westrick, J. A., and Ault, A. P. (2020). Harmful algal bloom toxins in aerosol generated from inland lake water. *Environ. Sci. Technol.* 54, 4769–4780. doi: 10.1021/acs.est.9b07727

On the mathematical foundations of theoretical statistics | Philosophical Transactions of the Royal Society of London. Series A, Containing Papers of a Mathematical or Physical Character (n.d.). Available at: https://royalsocietypublishing.org/doi/abs/10.1098/rsta.1922.0009 (Accessed June 17, 2024).

Pant, V., Deshpande, C. G., and Kamra, A. K. (2008). On the aerosol number concentration–wind speed relationship during a severe cyclonic storm over south Indian Ocean. *J. Geophys. Res. Atmospheres* 113. doi: 10.1029/2006JD008035

Park, J., Schoenberg, F. P., Bertozzi, A. L., and Brantingham, P. J. (2021). Investigating clustering and violence interruption in gang-related violent crime data using spatial–temporal point processes with covariates. *J. Am. Stat. Assoc.* 116, 1674–1687. doi: 10.1080/01621459.2021.1898408

Pierce, R. H., Henry, M. S., Blum, P. C., Hamel, S. L., Kirkpatrick, B., Cheng, Y. S., et al. (2005). Brevetoxin composition in water and marine aerosol along a Florida beach: Assessing potential human exposure to marine biotoxins. *Harmful Algae* 4, 965–972. doi: 10.1016/j.hal.2004.11.004

Pierce, R. H., Henry, M. S., Blum, P. C., Lyons, J., Cheng, Y. S., Yazzie, D., et al. (2003). Brevetoxin concentrations in marine aerosol: Human exposure levels during a Karenia brevis harmful algal bloom. *Bull. Environ. Contam. Toxicol.* 70, 161–165. doi: 10.1007/s00128-002-0170-y

Pietsch, R. B., Grothe, H., Hanlon, R., Powers, C. W., Jung, S., Ross, S. D., et al. (2018). Wind-driven spume droplet production and the transport of Pseudomonas syringae from aquatic environments. *PeerJ* 6, e5663. doi: 10.7717/peerj.5663

Plaas, H. E., and Paerl, H. W. (2021). Toxic cyanobacteria: A growing threat to water and air quality. *Environ. Sci. Technol.* 55, 44–64. doi: 10.1021/acs.est.0c06653

Pochwała, S., Gardecki, A., Lewandowski, P., Somogyi, V., and Anweiler, S. (2020). Developing of low-cost air pollution sensor—measurements with the unmanned aerial vehicles in Poland. *Sensors* 20, 3582. doi: 10.3390/s20123582

Powers, C. W., Hanlon, R., Grothe, H., Prussin, A. J., Marr, L. C., and Schmale, D. G. (2018). Coordinated sampling of microorganisms over freshwater and saltwater environments using an Unmanned Surface Vehicle (USV) and a Small Unmanned Aircraft System (sUAS). *Front. Microbiol.* 9. Available at: https://www.frontiersin.org/article/10.3389/fmicb.2018.01668 (Accessed May 13, 2022).

Prank, M., Chapman, D. S., Bullock, J. M., Belmonte, J., Berger, U., Dahl, A., et al. (2013). An operational model for forecasting ragweed pollen release and dispersion in Europe. *Agric. For. Meteorol.* 182–183, 43–53. doi: 10.1016/j.agrformet.2013.08.003

Prijith, S. S., Aloysius, M., Mohan, M., Beegum, N., and Krishna Moorthy, K. (2012). Role of circulation parameters in long range aerosol transport: Evidence from Winter-ICARB. *J. Atmospheric Sol.-Terr. Phys.* 77, 144–151. doi: 10.1016/j.jastp.2011.12.008

Quinn, P. K., Collins, D. B., Grassian, V. H., Prather, K. A., and Bates, T. S. (2015). Chemistry and related properties of freshly emitted sea spray aerosol. *Chem. Rev.* 115, 4383–4399. doi: 10.1021/cr500713g

Rahman, E. U., Khan, M. A., Algarni, F., Zhang, Y., Irfan Uddin, M., Ullah, I., et al. (2021). Computer vision-based wildfire smoke detection using UAVs. *Math. Probl. Eng.* 2021, e9977939. doi: 10.1155/2021/9977939

Ralston, D. K., and Moore, S. K. (2020). Modeling harmful algal blooms in a changing climate. *Harmful Algae* 91, 101729. doi: 10.1016/j.hal.2019.101729

Ross, S. D., Fish, J., Moeltner, K., Bollt, E. M., Bilyeu, L., and Fanara, T. (2022). Beach-level 24-hour forecasts of Florida red tide-induced respiratory irritation. *Harmful Algae* 111, 102149. doi: 10.1016/j.hal.2021.102149

Sang-Nourpour, N., and Olfert, J. S. (2019). Calibration of optical particle counters with an aerodynamic aerosol classifier. *J. Aerosol Sci.* 138, 105452. doi: 10.1016/j.jaerosci.2019.105452

Schmale, D. G., Ault, A. P., Saad, W., Scott, D. T., and Westrick, J. A. (2019). Perspectives on Harmful Algal Blooms (HABs) and the cyberbiosecurity of freshwater systems. *Front. Bioeng. Biotechnol.* 7. Available at: https://www.frontiersin.org/article/10.3389/fbioe.2019.00128 (Accessed May 13, 2022).

Schmale, D. G., and Ross, S. D. (2015). Highways in the sky: Scales of atmospheric transport of plant pathogens. *Annu. Rev. Phytopathol.* 53, 591–611. doi: 10.1146/annurev-phyto-080614-115942

Shin, J., Khim, B.-K., Jang, L.-H., Lim, J., and Jo, Y.-H. (2022). Convolutional neural network model for discrimination of harmful algal bloom (HAB) from non-HABs using Sentinel-3 OLCI imagery. *ISPRS J. Photogramm. Remote Sens.* 191, 250–262. doi: 10.1016/j.isprsjprs.2022.07.012

Slade, J. H., VanReken, T. M., Mwaniki, G. R., Bertman, S., Stirm, B., and Shepson, P. B. (2010). Aerosol production from the surface of the Great Lakes. *Geophys. Res. Lett.* 37. doi: 10.1029/2010GL043852

Smayda, T. J. (1997). Harmful algal blooms: Their ecophysiology and general relevance to phytoplankton blooms in the sea. *Limnol. Oceanogr.* 42, 1137–1153. doi: 10.4319/lo.1997.42.5_part_2.1137

Smith, E. A., Blanchard, P. B., and Bargu, S. (2014). Education and public outreach concerning freshwater harmful algal blooms in Southern Louisiana. *Harmful Algae* 35, 38–45. doi: 10.1016/j.hal.2014.03.008

Steffen, M. M., Belisle, B. S., Watson, S. B., Boyer, G. L., and Wilhelm, S. W. (2014). Status, causes and controls of cyanobacterial blooms in Lake Erie. *J. Gt. Lakes Res.* 40, 215–225. doi: 10.1016/j.jglr.2013.12.012

Stumpf, R. P. (2001). Applications of satellite ocean color sensors for monitoring and predicting harmful algal blooms. *Hum. Ecol. Risk Assess. Int. J.* 7, 1363–1368. doi: 10.1080/20018091095050

Stumpf, R. P., Culver, M. E., Tester, P. A., Tomlinson, M., Kirkpatrick, G. J., Pederson, B. A., et al. (2003). Monitoring *Karenia brevis* blooms in the Gulf of Mexico using satellite ocean color imagery and other data. *Harmful Algae* 2, 147–160. doi: 10.1016/S1568-9883(02)00083-5

Stumpf, R. P., Tomlinson, M. C., Calkins, J. A., Kirkpatrick, B., Fisher, K., Nierenberg, K., et al. (2009). Skill assessment for an operational algal bloom forecast system. *J. Mar. Syst.* 76, 151–161. doi: 10.1016/j.jmarsys.2008.05.016

Sutherland, J. (2021). The detection of airborne anatoxin-a (ATX) on glass fiber filters during a harmful algal bloom. *Lake Reserv. Manag.* 37, 113–119. doi: 10.1080/10402381.2021.1881191

Taha, G., Loughman, R., Colarco, P. R., Zhu, T., Thomason, L. W., and Jaross, G. (2022). Tracking the 2022 Hunga Tonga-Hunga Ha'apai aerosol cloud in the upper and middle stratosphere using space-based observations. *Geophys. Res. Lett.* 49, e2022GL100091. doi: 10.1029/2022GL100091

Türkyilmaz, K., van Lieshout, M. N. M., and Stein, A. (2013). Comparing the Hawkes and Trigger Process Models for aftershock sequences following the 2005 Kashmir earthquake. *Math. Geosci.* 45, 149–164. doi: 10.1007/s11004-012-9438-x

Vaidyanathan, A., Yip, F., and Garbe, P. (2018). Developing an online tool for identifying at-risk populations to wildfire smoke hazards. *Sci. Total Environ.* 619–620, 376–383. doi: 10.1016/j.scitotenv.2017.10.270

VanCuren, R. A., Cahill, T., Burkhart, J., Barnes, D., Zhao, Y., Perry, K., et al. (2012). Aerosols and their sources at Summit Greenland – First results of continuous size- and time-resolved sampling. *Atmos. Environ.* 52, 82–97. doi: 10.1016/j.atmosenv.2011.10.047

Vargo, G., Heil, C., Fanning, K., Dixon, L., Neely, M., Lester, K., et al. (2008). Nutrient availability in support of Karenia brevis blooms on the central West Florida Shelf: What keeps Karenia blooming? *Cont. Shelf Res.* 28, 73–98. doi: 10.1016/j.csr.2007.04.008

Veen, A., and Schoenberg, F. P. (2008). Estimation of space–time branching process models in seismology using an EM–Type algorithm. *J. Am. Stat. Assoc.* 103, 614–624. doi: 10.1198/016214508000000148

Vincent, J. H. (2007). *Aerosol Sampling: Science, Standards, Instrumentation and Applications*. John Wiley & Sons.

Wang, X., Zhou, H., Arnott, W. P., Meyer, M. E., Taylor, S., Firouzkouhi, H., et al. (2020). Evaluation of gas and particle sensors for detecting spacecraft-relevant fire emissions. *Fire Saf. J.* 113, 102977. doi: 10.1016/j.firesaf.2020.102977

Watson, S. B., Whitton, B. A., Higgins, S. N., Paerl, H. W., Brooks, B. W., and Wehr, J. D. (2015). "Chapter 20 - Harmful Algal Blooms," in *Freshwater Algae of North America (Second Edition)*, eds. J. D. Wehr, R. G. Sheath, and J. P. Kociolek (Boston: Academic Press), 873–920. doi: 10.1016/B978-0-12-385876-4.00020-7

Weber, S. J., Mishra, D. R., Wilde, S. B., and Kramer, E. (2020). Risks for cyanobacterial harmful algal blooms due to land management and climate interactions. *Sci. Total Environ.* 703, 134608. doi: 10.1016/j.scitotenv.2019.134608

Wei, Z., Wang, X., An, W., and Che, J. (2009). Target-tracking based early fire smoke detection in video., in *2009 Fifth International Conference on Image and Graphics*, 172–176. doi: 10.1109/ICIG.2009.173

Welch, E. B. (2009). Should nitrogen be reduced to manage eutrophication if it is growth limiting? Evidence from Moses Lake. *Lake Reserv. Manag.* 25, 401–409. doi: 10.1080/07438140903323757

Wells, M. L., and Karlson, B. (2018). "Harmful Algal Blooms in a Changing Ocean," in *Global Ecology and Oceanography of Harmful Algal Blooms*, eds. P. M. Glibert, E. Berdalet, M. A. Burford, G. C. Pitcher, and M. Zhou (Cham: Springer International Publishing), 77–90. doi: 10.1007/978-3-319-70069-4_5

Wells, M. L., Karlson, B., Wulff, A., Kudela, R., Trick, C., Asnaghi, V., et al. (2020). Future HAB science: Directions and challenges in a changing climate. *Harmful Algae* 91, 101632. doi: 10.1016/j.hal.2019.101632

Wiedensohler, A., Birmili, W., Putaud, J.-P., and Ogren, J. (2013). "Recommendations for Aerosol Sampling," in *Aerosol Science*, (John Wiley & Sons, Ltd), 45–59. doi: 10.1002/9781118682555.ch3

Wire Pull Smoke (WP40) - EG Products (2020). Available at: https://eg-products.com/information/safety/psds-wire-pull-smoke-wp40 (Accessed August 1, 2024).

Xing, D., Zhongming, Y., Lin, W., and Jinlan, L. (2015). Smoke image segmentation based on color model. *J. Innov. Sustain. RISUS* 6, 130–138. doi: 10.24212/2179-3565.2015v6i2p130-138

Zhang, T., Zhao, T., Takahashi, H., Hata, M., Toriba, A., Ikeda, T., et al. (2017). High volume air sampler for environmental nanoparticles using a sharp-cut inertial filter combined with an impactor. *Meas. Sci. Technol.* 28, 025801. doi: 10.1088/1361-6501/aa53a5

Zhao, Y., Lu, W., Zheng, Y., and Wang, J. (2012). An early smoke detection system based on increment of optical flow residual., in *2012 International Conference on Machine Learning and Cybernetics*, 1474–1479. doi: 10.1109/ICMLC.2012.6359582

Zhou, Z., Shi, Y., Gao, Z., and Li, S. (2016). Wildfire smoke detection based on local extremal region segmentation and surveillance. *Fire Saf. J.* 85, 50–58. doi: 10.1016/j.firesaf.2016.08.004

Zohdi, E., and Abbaspour, M. (2019). Harmful algal blooms (red tide): a review of causes, impacts and approaches to monitoring and prediction. *Int. J. Environ. Sci. Technol.* 16, 1789–1806. doi: 10.1007/s13762-018-2108-x